NAVAL POSTGRADUATE SCHOOL
Monterey, California

DTIC
ELECTE
MAR 12 1991
S
B
D

DISSERTATION

PARAMETRIC MODELING AND ESTIMATION
OF PULSE PROPAGATION ON MICROWAVE
INTEGRATED CIRCUIT INTERCONNECTIONS

by

Edward M. Siomacco

June 1990

Thesis Advisor: Murali Tummala

Approved for public release; distribution is unlimited

REPORT DOCUMENTATION PAGE		Form Approved OMB No 0704-0188

1a REPORT SECURITY CLASSIFICATION UNCLASSIFIED	1b RESTRICTIVE MARKINGS

2a SECURITY CLASSIFICATION AUTHORITY	3 DISTRIBUTION/AVAILABILITY OF REPORT Approved for public release; distribution is unlimited
2b DECLASSIFICATION/DOWNGRADING SCHEDULE	

4 PERFORMING ORGANIZATION REPORT NUMBER(S)	5 MONITORING ORGANIZATION REPORT NUMBER(S)

6a NAME OF PERFORMING ORGANIZATION Naval Postgraduate School	6b OFFICE SYMBOL (If applicable) EC	7a. NAME OF MONITORING ORGANIZATION Naval Postgraduate School

6c. ADDRESS (City, State, and ZIP Code) Monterey, California 93943-5000	7b ADDRESS (City, State, and ZIP Code) Monterey, California 93943-5000

8a NAME OF FUNDING/SPONSORING ORGANIZATION	8b OFFICE SYMBOL (If applicable)	9 PROCUREMENT INSTRUMENT IDENTIFICATION NUMBER

8c. ADDRESS (City, State, and ZIP Code)	10 SOURCE OF FUNDING NUMBERS			
	PROGRAM ELEMENT NO	PROJECT NO	TASK NO	WORK UNIT ACCESSION NO

11 TITLE (Include Security Classification) PARAMETRIC MODELING AND ESTIMATION OF PULSE PROPAGATION ON MICROWAVE INTEGRATED CIRCUIT INTERCONNECTIONS

12 PERSONAL AUTHOR(S) SIOMACCO, Edward M.

13a TYPE OF REPORT PhD Dissertation	13b TIME COVERED FROM _____ TO _____	14 DATE OF REPORT (Year, Month, Day) 1990 June	15 PAGE COUNT 157

16 SUPPLEMENTARY NOTATION The views expressed in this thesis are those of the author and do not reflect the official policy or position of the Department of Defense or the U.S. Government.

17 COSATI CODES			18 SUBJECT TERMS (Continue on reverse if necessary and identify by block number)
FIELD	GROUP	SUB-GROUP	Microstrip; ARMA; Parametric Modeling, Parameter Estimation

19 ABSTRACT (Continue on reverse if necessary and identify by block number) The modeling of picosecond pulse propagation on microwave integrated circuit interconnections is considered. Autoregressive moving-average (ARMA) and autoregressive (AR) parametric models are derived for lossy dispersive microstrip transmission lines and cascaded microstrip step discontinuities. We formulated mathematical expressions to relate the model parameters to the physical microstrip properties.

New lumped-distributed equivalent circuit models are presented. Dispersive pulse propagation on high-frequency integrated circuit interconnections is modeled using frequency-dependent lumped parameters and lossy distributed transmission-line sections. We verified the equivalent circuit models through computer simulations and experimental measurements. Modern parameter estimation techniques are applied to system identification modeling. We develop several algorithms to estimate the model parameters from input and/or output measurements. The performance of the algorithms are evaluated using computer simulations and experimental results.

20 DISTRIBUTION/AVAILABILITY OF ABSTRACT ☒ UNCLASSIFIED/UNLIMITED ☐ SAME AS RPT ☐ DTIC USERS	21 ABSTRACT SECURITY CLASSIFICATION UNCLASSIFIED	
22a NAME OF RESPONSIBLE INDIVIDUAL TUMMALA, Murali	22b TELEPHONE (Include Area Code) 408-646-2645	22c OFFICE SYMBOL EC/Tu

DD Form 1473, JUN 86   Previous editions are obsolete   SECURITY CLASSIFICATION OF THIS PAGE

S/N 0102-LF-014-6603

1

Parametric Modeling and Estimation of Pulse Propagation
on Microwave Integrated Circuit Interconnections

by

Edward Michael Siomacco
Major, United States Army
B.S., North Carolina State University, 1975
M.S., Naval Postgraduate School, 1985

Submitted in partial fulfillment of the
requirements for the degree of

DOCTOR OF PHILOSOPHY IN ELECTRICAL ENGINEERING

from the

NAVAL POSTGRADUATE SCHOOL

June 1990

Author: _____
Edward Michael Siomacco

Approved by:

_____   _____
Glen A. Myers   Jeffrey B. Knorr
Associate Professor of Electrical   Professor of Electrical and
and Computer Engineering   Computer Engineering

_____   _____
Harold M. Fredricksen   Michael J. Zyda
Professor of Mathematics   Associate Professor of Computer Science

_____   _____
Charles W. Therrien   Murali Tummala
Professor of Electrical and   Assistant Professor of Electrical
Computer Engineering   and Computer Engineering
                                     Dissertation Supervisor

Approved by: _____
John P. Powers, Chairman,
Department of Electrical and Computer Engineering

Approved by: _____
Provost/Academic Dean

ii

ABSTRACT

The modeling of picosecond pulse propagation on microwave integrated circuit interconnections is considered. Autoregressive moving-average (ARMA) and autoregressive (AR) parametric models are derived for lossy dispersive microstrip transmission lines and cascaded microstrip step discontinuities. We formulated mathematical expressions to relate the model parameters to the physical microstrip properties.

New lumped-distributed equivalent circuit models are presented. Dispersive pulse propagation on high-frequency integrated circuit interconnections is modeled using frequency-dependent lumped parameters and lossy distributed transmission-line sections. We verified the equivalent circuit models through computer simulations and experimental measurements. Modern parameter estimation techniques are applied to system identification modeling. We develop several algorithms to estimate the model parameters from input and/or output measurements. The performance of the algorithms are evaluated using computer simulations and experimental results.

iii

TABLE OF CONTENTS

vi

LIST OF TABLES

LIST OF FIGURES

ACKNOWLEDGEMENT

My sincere thanks to Him, for everlasting guidance. I would like to express my appreciation for the dedication and research support to me by Professor Murali Tummala. This work would have been impossible without him.

I would also like to thank the members of the Doctoral Committee. In particular, I wish to express my gratitude to Professor Glen A. Myers for his support and for his *voltage* approach to communications, to Professor Charles W. Therrien for his friendship and challenging multi-dimensional signal processing concepts, and to Professor Jeff B. Knorr for his interest in this research. In addition, many thanks to Professor H. M. Fredricksen for his dedication to electrical engineering, mathematically speaking, and to Professor M. J. Zyda for his graphical outlook on life.

Several faculty members at the Naval Postgraduate School have significantly contributed to the thesis. In particular, I wish to thank Professor R.D. Strum who provided to me friendship and an opportunity to learn.

Additional thanks go to Colonel Stanley E. Reinhart, Jr. and Major Glen C. Long of the Department of Electrical Engineering at USMA. I also wish to thank my wife, Linda, for all she has done during these many years. Her patience, understanding, and support greatly contributed to my efforts to complete this work.

I. INTRODUCTION

Microwave and high-speed very large scale integrated (VLSI) circuits are limited by the propagation characteristics of the on-chip interconnections [Ref. 1]. The effects of signal dispersion and loss become even more predominant as devices and circuits are scaled to smaller dimensions. At microwave frequencies, the interconnections between elements on a dielectric substrate, such as silicon (Si) or gallium arsenide (GaAs) where considerable wavelength reductions occur, must be treated as planar waveguide structures. The analysis and design of circuits consisting of these guided wave structures are facilitated by the use of equivalent circuits. Accurate high frequency characterization of picosecond pulse propagation on these structures including dispersion and losses requires extensive numerical techniques. The empirical equations that have been derived for the propagation parameters from these numerical results do not lead to an equivalent circuit model with realizable series and shunt branches. Furthermore, reliable and accurate empirical models for many useful structures such as microstrips on dielectric substrate used in monolithic microwave integrated circuits (MMIC's) are not available [Ref. 2: pp. 256-262].

Knowledge of the transient signal behavior on microstrip transmission lines is essential for the design of MMIC's at high switching speeds or high frequencies. High-speed time-domain measurements must be used to properly understand and model the transient response. The microwave techniques available for picosecond pulse propagation characterization are scattering parameter measurements, high-speed sampling oscilloscope measurements, and picosecond photoconductor measurements. The scattering or s-parameter measurement method is a small-signal frequency-domain technique which is widely used by microwave network analyzers. High-speed sampling oscilloscope measurements can characterize low-level signals and have a higher signal-to-noise (S/N) ratio than the s-parameter method. Picosecond photoconductor measurements are a new high-frequency measurement technique made possible by advances in laser technology. The generation of optical pulses with sub-picosecond duration are shorter than those that can be generated solely by electronic means [Ref.

1

3: pp. 117-124]. An opto-electronic transducer such as a photoconductor permits the conversion of these sub-picosecond optical pulses to picosecond electrical signals. The significant advantage of this technique is the photoconductors can be integrated on the substrate material to facilitate very high-speed measurements with extremely high S/N and sensitivity to microvolt signal levels. The disadvantage of the s-parameter and sampling oscilloscope measurement methods is they suffer from poor connections in terms of high-frequency signal transmission on the substrate.

There is an urgent need for the development of computer-aided design (CAD) models tailored specifically to the special demands of MMIC technology. MMIC's are not readily tunable after manufacture, and the time and costs involved in a design are high. In addition to the development of new models for CAD design, a diagnostic testing procedure that permits on-wafer characterization of MMIC's before dicing the wafer into individual chips is highly desirable [Ref. 4: p.14].

It will be useful to formulate a digital signal processing framework to solve this modeling problem. The motivation for this approach is simple. The availability of input and output time-domain measurements invites the transition from an equivalent circuit model to a parametric model. For our purposes, we will define a parametric model as a discrete mathematical description of the actual propagation mechanism of the system in terms of specific model parameters or coefficients. Three particularly important discrete-time parametric models are the moving-average (MA), the autoregressive (AR), and their combination, the autoregressive moving-average (ARMA) model. These models are described as linear transformations of respective input-output time series.

The model-building process is determined from *a priori* (structural) knowledge and *a posteriori* (measurement) knowledge of the system. The basic approach taken in this dissertation, with respect to the modeling of microwave integrated circuit (MIC) interconnections, is to represent them as linear time-invariant systems. This allows linear algorithms to be applied to the solution of the modeling and parameter estimation problem. The structural knowledge of the microstrip line permits the use of empirical and analytical expressions to formulate lumped-distributed equivalent

circuit models which can characterize the system. Rational network functions are evaluated from the circuit models and discrete linear transformations are employed to produce the parametric models.

Another main emphasis of this research is on the system identification aspect. Identification is defined by Zadeh [Ref. 5: pp. 856-865] as: *"the determination on the basis of input and output, of a system within a specified class of systems, to which the system under test is equivalent."* Consequently, the identification problem is reduced to that of model parameter estimation based upon measurement knowledge.

A. HISTORICAL BACKGROUND

Numerous authors have focused their research on various computational approaches to analyze and model microstrip on different substrates [Refs. 6,7]. Accurate and complete analysis, however, requires elaborate mathematical models and time intensive numerical techniques. Quasi-TEM mode calculations combined with frequency-dependent expressions can achieve accuracies within one percent of the full-wave analysis [Ref. 8]. Computer-aided design (CAD) programs are available with the capability of both synthesis and analysis of microstrip lines. The extensive development of closed-form expressions for the frequency-dependent effective microstrip permittivity $\epsilon_{eff}(f)$, has produced rapid computation of the microstrip parameters. However, the empirical equations that have been derived for the frequency-dependent propagation terms do not lead to an equivalent circuit model with realizable series and shunt circuit impedances. It is these equivalent impedances that relate to the physical microstrip properties. Therefore, the effective microstrip permittivity of different dielectric substrates is critical for the synthesis and validation of IC interconnections models.

Recently, optical techniques have been successfully used in the characterization of microwave devices and integrated circuits. Frequency-domain measurements have been performed using electro-optic probing of a microstrip line. In this work, the microwave signal is launched onto the circuit using coplanar waveguide (CPW) contacting probes. Hung et al. [Ref. 9] have developed an on-wafer GaAs MMIC

measurement system using a picosecond pulse sampling technique proposed by Auston [Ref. 10]. This optoelectronic characterization has been demonstrated to achieve a broad-band frequency response for both the magnitude and the phase of a K_a-band (27-40 GHz) MMIC.

The problem of system identification is the determination of a mathematical model that provides an optimum characterization for a system or process. Usually our knowledge of the system is limited by observable input-output measurements. The inverse scattering problem as applied to electromagnetic systems has close connections to several signal processing concepts such as the design of digital filters, the development of linear prediction algorithms and their lattice filter implementations. In particular, transmission-line systems on planar dielectric materials can be interpreted as layered, wave scattering structures. Two successful analogous applications have been in speech and seismic signal processing. In speech, the vocal tract has been modeled as an acoustic tube of varying cross-sectional area [Ref. 11]. The inverse, or model identification, problem is to determine the medium properties from its reflection response measured at an observable boundary, to some incident input signal. This also relates to the seismic problem. Here, an impulsive input to the earth, such as an explosion, will generate seismic waves propagating downwards. Reflections are produced as the wave encounters respective earth layers. From the resulting reflected waves, the layered structure beneath the surface can be identified.

Bruckstein and Kailath [Ref. 12] have specified conditions on the layered structure that permits the use of recursive parameter estimation algorithms. Their first algorithm takes scattering data and processes it to identify a unique layer and then, at each iteration, replaces the data by a set of "synthetic" scattering data. This procedure is called the *layer-peeling* method. The second approach, called the *layer-adjoining* method, propagates the original scattered data through the previously identified layer to determine information about future layers. The *layer-adjoining* method is the Levinson-Durbin alogrithm for solving the Toeplitz normal equations. For lossless structures, the *layer-peeling* method is the Schur algorithm. The primary difference between the *layer-adjoining* and the *layer-peeling* process is that the latter method

4

has avoided the requirement to compute inner products. These algorithms will provide background for the derivation of model parameter estimation algorithms that will be presented in Chapter V.

Bruckstein, Levy and Kailath [Ref. 13] have discussed several classes of physical models that are equivalent descriptions of a lossless scattering media. They presented how a lumped circuit model for a uniform lossless transmission line, described by partial differential equations, can be formulated into a discretized wave scattering layered model. This model illustrates how propagating waves through a lossless transmission line can be described as a multi-layered medium. Each layer is characterized by its impedance function which directly relates to a layer reflection coefficient. In Chapter IV, multiple microstrip discontinuities are compared to the multi-layered model; however, loss and dispersion are considered.

B. OBJECTIVES OF THE RESEARCH

The first objective of this research is to develop an equivalent circuit model for a dispersive lossy microstrip transmission line which is compatible with the standard circuit analysis and design techniques, including computer-aided design (CAD) tools. The proposed circuit model will then be extended to describe abrupt width dimension changes, called impedance discontinuities, of the microstrip line. The transient analysis of these equivalent circuits will simulate the picosecond pulse propagation on dispersive lossy microstrip lines and the effects of impedance discontinuities can be modeled. The circuit models will be verified using photoconductor measurements from IC interconnections and experimental results from fabricated microstrip test structures.

The second objective of the thesis is to derive ARMA and AR parametric models for three microstrip test structures. These include 1) an impedance matched microstrip transmission line, 2) a cascaded microstrip step discontinuity, and 3) a multi-section microstrip step discontinuity. The impedance matched microstrip line describes the typical MIC interconnection [Ref. 3: pp. 18-19]. As discussed eariler, the formulation of these parametric models provides an opportunity to exploit existing

parameter estimation algorithms, as well as develop new algorithms to characterize transient signal propagation on MIC's.

The last objective is the development of parameter estimation algorithms. This research work will focus on the estimation of both ARMA and AR model parameters from the impulse response of an electrically short microstrip line section. Additionally, the system identification of the multi-section microstrip structure will also be investigated. The detection of each section impulse response will be complicated by pulse dispersion, propagation loss, and multiple reflections due to the impedance discontinuities. A new *layer-probing* algorithm will be presented to overcome these difficulties. Computer simulations of the algorithms are performed to validate their performance.

C. ORGANIZATION OF THE REPORT

Chapter II derives a lumped-distributed equivalent circuit that includes the effects of microstrip loss and dispersion. The bandwidth of the propagating pulse will establish a maximum wavelength of interest. The physical length of the IC interconnection being considered will be very much less than a quarter-wavelength. Under this condition the lumped-element circuit approximation is used to characterize the microstrip line section.

Chapter III presents the parametric models for the impedance matched quarter-wavelength microstrip transmission line. An ARMA parametric model is derived from the network function of the equivalent circuit model. The ARMA model coefficients are shown to be directly related to the equivalent lumped capacitance and inductance of the circuit model. An AR parametric model will also be presented. Relationships are given to evaluate the effective microstrip permittivity directly from the ARMA/AR model parameters.

In Chapter IV, microstrip discontinuities will be considered. Equivalent circuit models are derived for a cascaded microstrip step discontinuity. Similarly, ARMA and AR parametric models are developed using discrete transformations of the equivalent circuit network functions.

Parameter estimation algorithms are the emphasis in Chapter V. Several estimation algorithms are developed for both deterministic and stochastic data. Three deterministic based algorithms are presented. A weighted least squares (WLS) algorithm is derived to solve the ARMA model parameters from a finite-length impulse response. An alternative technique will analytically approximate a transfer function of the microstrip section using measured input-output rise and delay times of a transient pulse. Finally, AR model parameters are estimated from the impulse response using the Schur algorithm [Ref. 14]. The stochastic algorithms will assume that a white noise source is applied to the input of the microstrip structure. The Schur algorithm will estimate the AR model parameters from the output data. When input and output random data are available, an ARMA parameter estimation algorithm based on a generalized Mullis-Roberts (M-R) criterion [Ref. 15] is employed. However, if only the output data can be measured, a modified two-stage least squares algorithm is presented to estimate a second-order ARMA model. Finally, new system identification algorithms for the multi-section microstrip step discontinuity are presented.

Chapter VI presents simulation and experimental results. Waveform comparisons are made between measured data, equivalent circuit simulations, and parametric model simulations for each microstrip test structure. The performance of the parameter estimation algorithms will be investigated.

Chapter VII is a summary of the significant contributions presented in this dissertation. It draws conclusions from the results and proposes some important future directions for this research.

Three appendices are included. Appendix A contains an alternate proof of the Schur algorithm. Appendix B contains the equivalent circuit model listings that are used by the transient analysis program. Appendix C contains listings of the FORTRAN programs used in the simulations presented in this report.

II. MICROSTRIP CHARACTERIZATION

In this chapter equivalent circuit models are derived for a lossy dispersive microstrip transmission line. The propagation characteristics of the transmission line are modeled by lumped-distributed equivalent circuit models. In order to derive the expressions for the equivalent lumped circuit elements, the models are defined for a maximum frequency of interest which is restricted by the physical length of the microstrip line and the dielectric constant of the substrate. The empirical equations described in the literature for the propagation parameters do not usually lead to an equivalent circuit model [Ref. 16].

The equivalent circuit models presented are compatible with standard circuit analysis and design techniques including the use of computer-aided design tools such as PSPICE [Ref. 17]. The proposed models will include the effects of dispersion and loss at microwave frequencies.

A. IC MICROSTRIP INTERCONNECTIONS

Integrated circuit interconnections can be described by microstrip transmission lines because their geometries are similar. The abrupt dielectric interface shown by the open microstrip geometry in Figure 2.1 makes it incapable of supporting a single model of propagation. However, microstrip propagates the bulk of its energy in a field distribution which approximates the transverse electromagnetic (TEM) mode and is usually referred to as the quasi-TEM or quasi-static mode [Ref. 18]. Several computational approaches are available utilizing quasi-TEM mode calculations combined with closed-form frequency-dependent expressions [Ref. 6]. It is this latter approach which is considered in this work.

8

The characteristic impedance of a TEM transmission line is described by

$$Z_0 = \sqrt{\frac{L}{C}} \tag{2.1}$$

where L and C are the equivalent lumped inductance and capacitance of the microstrip section, respectively. With microstrip geometries, the same type of dielectric substrate is used below the conductor. However, there is air above the conductor.
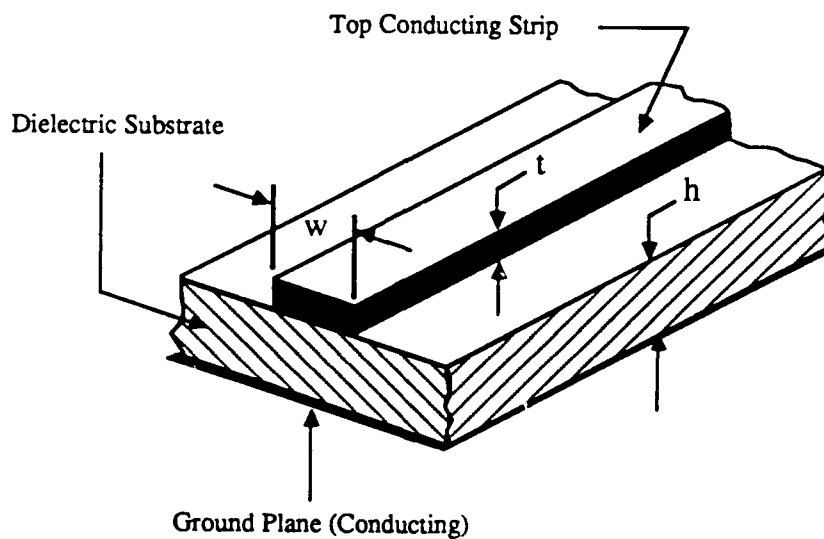
Figure 2.1 Generalized open microstrip geometry

The dielectric constant used in the design must take into consideration the dielectric constant of air ($\epsilon_r = 1$) and that of the substrate material. The effective microstrip permittivity ϵ_{eff} will be introduced. This quantity is unique to mixed-dielectric transmission line systems and it provides a useful link between different wavelengths, impedances, and propagating velocities.

An expression for the static-TEM effective microstrip permittivity has been calculated by Owens [Ref. 19]:

$$\epsilon_{eff} = \frac{\epsilon_r + 1}{2} + \frac{\epsilon_r - 1}{2}\left(1 + 10\frac{h}{w}\right)^{-0.555} \tag{2.2}$$

where ϵ_r is the relative dielectric constant of the substrate. Using the effective microstrip permittivity, the characteristic impedance at TEM frequencies is calculated by

$$Z_0 = \frac{60}{\sqrt{\epsilon_{eff}}} \ln\left(\frac{8h}{w} + \frac{w}{4h}\right) \qquad\qquad w < h \tag{2.3a}$$

$$= \frac{120\pi}{\sqrt{\epsilon_{eff}}}\left(\frac{w}{h} + 1.393 + 0.667\ln\left(\frac{w}{h} + 1.444\right)\right)^{-1} \qquad w > h \tag{2.3b}$$

where w and h are microstrip conductor width and substrate thickness, respectively [Ref. 20]. A correction factor is applied to account for the fringing fields associated with a finite conductor thickness. Bahl et al. [Ref. 21] have introduced an effective width parameter into (2.3) in order to improve the Z_0 calculation. The effective width w_e, replaces the w in equation (2.3)

$$w_e = w + \frac{1.25t}{\pi}\left(1 + \ln\left(\frac{4\pi\,w}{t}\right)\right), \qquad \frac{w}{h} \le \frac{1}{2\pi} \tag{2.4a}$$

$$w_e = w + \frac{1.25t}{\pi}\left(1 + \ln\left(\frac{2h}{t}\right)\right), \qquad \frac{w}{h} \ge \frac{1}{2\pi}. \tag{2.4b}$$

where t is the conductor thickness.

B. FREQUENCY-DEPENDENT MICROSTRIP MODELS

The quasi-TEM analysis of microstrip transmission lines mentioned above begins to lose accuracy at high microwave frequencies. The characteristic impedance and the effective microstrip permittivity are dependent upon the dielectric thickness-to-guide wavelength ratio, $2\pi h/\lambda_g$ [Ref. 22]. In addition, different loss mechanisms become important and the attenuation function is also frequency dependent. This frequency-dependency of the microstrip is caused by a hybrid mode of propagation

10

that describes a coupled version of both transverse electric (TE) and transverse magnetic (TM) modes.

The propagation group velocity of a signal also depends on the frequency-dependent effective microstrip permittivity as

$$v_g(f) = \frac{c}{\sqrt{\epsilon_{eff}(f)}} \tag{2.5}$$

where c is the velocity of light in a vacuum. Pulses which have a spectral component above the TEM mode frequency regime will be dispersed because the higher harmonics of the pulse will travel at a slower phase velocity than the lower harmonics [Ref. 18]. Therefore, the phase constant (β) is a non-linear function of frequency, which leads to the phenomena of dispersion.

Several methods for evaluating the frequency-dependent effective microstrip permittivity are available [Refs. 23, 24]. However, Yamashita et $al.$ [Ref. 7] have derived an expression by curve fitting the data obtained from a full-wave analysis as

$$\sqrt{\epsilon_{eff}(f)} = \sqrt{\epsilon_{eff}} + \left(\sqrt{\epsilon_r} - \sqrt{\epsilon_{eff}}\right) \Big/ \left(1 + 4F^{-\frac{3}{2}}\right) \tag{2.6}$$

where

$$F = \left(\frac{f}{c}\right)(4h\sqrt{\epsilon_r - 1})\left[\frac{1}{2} + \left(1 + 2\,\log\left(1 + \frac{w}{h}\right)\right)^2\right].$$

If the substrate material is lossless, the phase constant becomes

$$\beta_0 = \frac{2\pi\,f\,\sqrt{\epsilon_{eff}}}{c}. \tag{2.7}$$

However, finite resistivity of the conductor and finite conductivity of the substrate introduce attenuation. At low microwave frequencies the conductor loss factor α_c is given by [Ref.18: p. 90]

$$\alpha_c = \frac{0.072\sqrt{f}\,\lambda_g}{w\,Z_0} \qquad \mathrm{dB}/\lambda_g \tag{2.8}$$

11

where f is in gigahertz. For higher frequencies, Pucei *et al.* [Ref. 25] have calculated the conductor loss as

$$\alpha_c = \frac{8.68 \, R_s}{2\pi \, Z_0 \, h}\left[1 - \left(\frac{w'}{4h}\right)^2\right]\left[1 + \frac{h}{w'} + \frac{h}{\pi \, w'}\left(\ln\frac{4\pi \, w}{t} + \frac{t}{w}\right)\right],$$ (2.9a)

$$\text{for } \frac{w}{h} \le \frac{1}{2\pi}$$

$$\alpha_c = \frac{8.68 \, R_s}{2\pi \, Z_0 \, h}\left[1 - \left(\frac{w'}{4h}\right)^2\right]\left[1 + \frac{h}{w'} + \frac{h}{w'}\left(\ln\frac{2h}{t} - \frac{t}{h}\right)\right],$$ (2.9b)

$$\text{for } \frac{1}{2\pi} < \frac{w}{h} \le 2$$

$$\alpha_c = \frac{8.68 \, R_s}{Z_0 \, h\left\{\frac{w'}{2h} + \frac{2}{\pi}\ln\left[2\pi e \left(\frac{w'}{2h} + 0.94\right)\right]\right\}^2}\left[\frac{w'}{h} + \frac{w'/(\pi \, h)}{w'/(2h) + 0.94}\right] \times$$

$$\left[1 + \frac{h}{w'} + \frac{h}{w'}\left(\ln\frac{2h}{t} - \frac{t}{h}\right)\right],$$ (2.9c)

$$\text{for } 2 \le \frac{w}{h}$$

where α_c is in dB/cm and

$$w' = w + \Delta w$$

$$\Delta w = \frac{t}{\pi}\left(\ln\frac{4\pi w}{t} + 1\right), \quad \text{for} \quad \frac{2t}{h} < \frac{w}{h} \le \frac{1}{2\pi}$$

$$\Delta w = \frac{t}{\pi}\left(\ln\frac{2h}{t} + 1\right), \quad \text{for} \quad \frac{w}{h} \ge \frac{1}{2\pi}$$

and R_s is the surface skin resistance in ohms given by

$$R_s = \sqrt{\frac{\pi f \mu}{\sigma_c}}$$ (2.9d)

where μ is the conductor permeability and σ_c is the conductor conductivity. An expression for dielectric loss α_d has been derived by Hammerstad and Bekkadal [Ref. 26] as

$$\alpha_d = 27.3 \, \frac{\epsilon_r(\epsilon_{eff} - 1)\tan\delta}{\epsilon_{eff}(\epsilon_r - 1)} \quad \text{dB}/\lambda_g$$ (2.10)

12

where $\tan\delta$ is the loss tangent of the substrate. For lossy semiconductor substrates, the general attenuation and phase constants for the microstrip are derived from an analysis of a transmission line section modeled by series and shunt resistances to represent the conductor and dielectric loss mechanisms [Ref. 27] as

$$\alpha^2 = \frac{\sqrt{\left(\beta_0^2 + 4\alpha_c^2\right)\left(\beta_0^2 + 4\alpha_d^2\right)} - \beta_0^2 + 4\alpha_c\alpha_d}{2}, \qquad (2.11a)$$

$$\beta^2 = \frac{\sqrt{\left(\beta_0^2 + 4\alpha_c^2\right)\left(\beta_0^2 + 4\alpha_d^2\right)} + \beta_0^2 - 4\alpha_c\alpha_d}{2}. \qquad (2.11b)$$

C. PICOSECOND PULSE PROPAGATION

One of the research objectives is to accurately characterize picosecond pulses propagating on microwave IC interconnections. Researchers have studied the effects of dispersion on picosecond pulses by performing computer simulations in the frequency domain [Refs. 28,29]. An input time-domain signal $v(t,0)$ is transformed using Fast Fourier transform (FFT) techniques to produce the input frequency spectrum, $F\left\{v(t,0)\right\}$. A frequency-dependent propagation function $\gamma(f)$ acts upon each spectral component as

$$F\left\{v(t,0)\right\}\epsilon^{-\gamma(f)\,l}$$

where the propagation function is $\gamma(f) = \alpha(f) + j\beta(f)$ and l is the propagation distance along the microstrip. The distorted temporal pulse is determined using an inverse Fourier transform as

$$v(t,l) = F^{-1}\left\{F\left\{v(t,0)\right\}\epsilon^{-[\alpha(f) + j\beta(f)]\,l}\right\}.$$

The approach taken in this work is similar, but the exponential propagation term is replaced by a discrete parametric model of the microstrip section. Specifically, the phase term $\beta(f)$ is modeled by a digital transfer function $H(z)$, while a discrete loss multiplier describes the attenuation constant $\alpha(f)$ of the microstrip line section at a maximum frequency of interest. Chapter III will introduce the parametric models for several microstrip transmission line structures.

13

D. DERIVATION OF EQUIVALENT CIRCUIT MODELS

A microstrip transmission line is approximated by cascading several electrically short sections [Ref. 30]. A single section of microstrip line having a characteristic impedance Z_0 and terminated in a matched load impedance is shown in Figure 2.2a. The load impedance $Z_{(n+1)}$, is the equivalent input impedance of the $(n + 1)$-th section. The normalized input impedance to the n-th section is derived [Ref. 30] as

$$\frac{Z_n}{Z_0} = \frac{Z_{n+1}\cosh(\gamma l) + Z_0\sinh(\gamma l)}{Z_{n+1}\sinh(\gamma l) + Z_0\cosh(\gamma l)} \tag{2.12}$$

where the propagation function, $\gamma = \alpha + j\beta$, describes the attenuation α, and phase shift β of the n-th section. Equation (2.12) is rewritten as

$$\frac{Z_n}{Z_0} = \frac{\dfrac{Z_{n+1}}{Z_0} + \tanh(\gamma l)}{1 + \dfrac{Z_{n+1}}{Z_0}\tanh(\gamma l)}. \tag{2.13}$$

The hyperbolic function, $\tanh(\gamma l)$, is expanded to

$$\tanh(\gamma l) = \frac{\tanh(\alpha l) + j\tan(\beta l)}{1 + j\tanh(\alpha l)\tan(\beta l)}. \tag{2.14}$$

Substituting (2.14) into (2.13) yields

$$\frac{Z_n}{Z_0} = \frac{\left(\dfrac{Z_{n+1}}{Z_0}\right)' + \tanh(\alpha l)}{1 + \left(\dfrac{Z_{n+1}}{Z_0}\right)'\tanh(\alpha l)} \tag{2.15a}$$

where

$$\left(\frac{Z_{n+1}}{Z_0}\right)' = \frac{\dfrac{Z_{n+1}}{Z_0} + j\tan(\beta l)}{1 + j\left(\dfrac{Z_{n+1}}{Z_0}\right)\tan(\beta l)}. \tag{2.15b}$$

A physical interpretation of (2.15) is illustrated in Figure 2.2b. The original n-th section is equivalent to three sub-sections of the same characteristic impedance cascaded together. The first and third sub-sections provides attenuation but no

14

phase shift, and are modeled by purely resistive attenuator pads. The total loss of the microstrip line is divided equally between each π-attenuator. The center subsection has a pure imaginary propagation function and no attenuation. This type of reactive network corresponds to a lossless transmission line having a phase shift equal to the original section.

In classical filter theory the reactive lossless, two-port network has been described as a constant-k lowpass filter. Two variations of this filter network will now be presented. A reactive π-network is used to derive the lumped-parameter
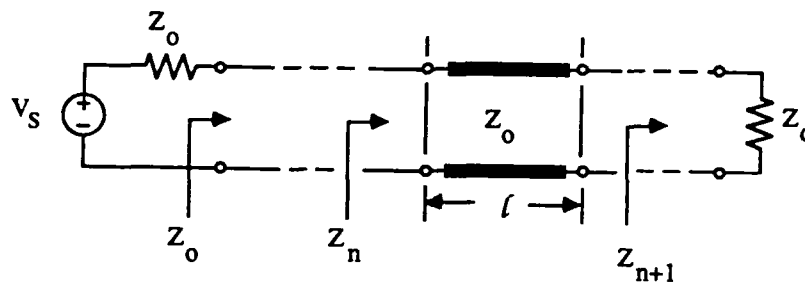
(a)
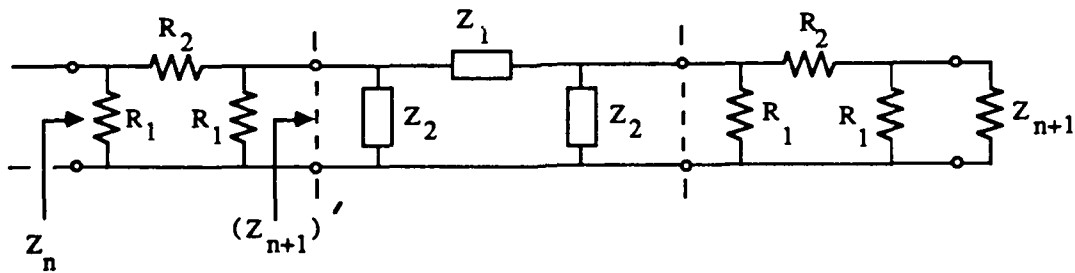
(b)

Figure 2.2 Microstrip line section equivalent circuit

equivalent circuit model and a reactive T-network is used to derive a lumped-distributed equivalent circuit model.

15

1. Lumped-Parameter Equivalent Reactive Π-Network

The lossless reactive network of Figure 2.2b is modeled by an equivalent π-network. The complex impedances are

$$Z_1 = \frac{Z_0}{j \tan\left(\dfrac{\beta l}{2}\right)} \tag{2.16a}$$

$$Z_2 = j Z_0 \sin(\beta l). \tag{2.16b}$$

Equations (2.16a) and (2.16b) represent a capacitive and an inductive lumped reactive impedance, respectively. Solving for the susceptive (B_C) and reactive (X_L) lumped elements yields

$$B_C = \frac{1}{Z_0} \tan\left(\frac{\beta l}{2}\right) \tag{2.17a}$$

$$X_L = Z_0 \sin(\beta l). \tag{2.17b}$$

Assuming a very short section length ($l << \lambda_g/4$), the equivalent shunt capacitance and series inductance can be approximated as follows [Ref. 18]

$$C_\pi \approx \frac{l}{2 Z_0 \, f \, \lambda_g} \tag{2.18a}$$

$$L_\pi \approx \frac{Z_0 \, l}{\lambda_g \, f} \ . \tag{2.18b}$$

The guide wavelength λ_g is expressed in terms of the frequency-dependent microstrip permittivity $\epsilon_{eff}(f)$ as

$$\lambda_g = \frac{c}{f \, \sqrt{\epsilon_{eff}(f)}} \tag{2.19}$$

where f is the highest frequency of interest of the propagating signal [Ref. 18: p. 70]. The resultant lumped-parameter equivalent circuit for the microstrip line section is shown in Figure 2.3.

2. Lumped-Distributed Equivalent Reactive T-Network

The reactive π-network of Figure 2.3 can be replaced by an equivalent T-network as shown in Figure 2.4a. The series inductive and the shunt capacitive impedances are then given by

$$Z_1 = jZ_0 \tan\left(\frac{\beta l}{2}\right) \qquad (2.20a)$$

$$Z_2 = \frac{Z_0}{j\sin(\beta l)}. \qquad (2.20b)$$

Solving for the reactive and susceptive lumped elements of Figure 2.4 yields

$$X_L = 2Z_0 \tan\left(\frac{\pi l}{\lambda_g}\right) \qquad (2.21a)$$

$$B_C = \frac{1}{Z_0}\sin\left(\frac{2\pi\, l}{\lambda_g}\right). \qquad (2.21b)$$
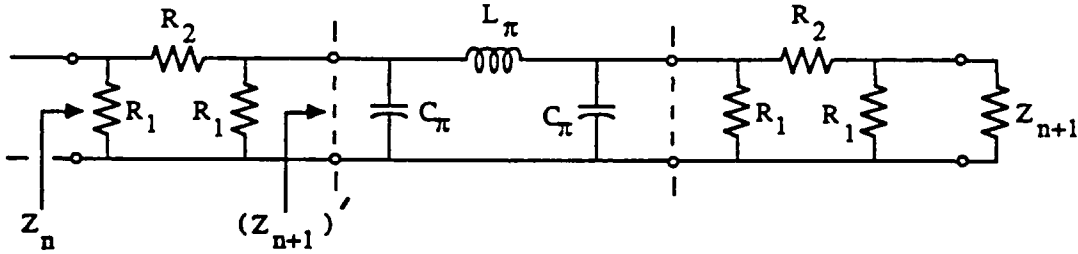
Figure 2.3 Lumped-parameter equivalent circuit model

Assuming a section length that is less than a quarter wavelength, the lumped elements can be approximated as follows [Ref. 18]:

$$L_T \approx \frac{Z_0 l}{f\,\lambda_g} \qquad (2.22a)$$

$$C_T \approx \frac{l}{Z_0 f \lambda_g}. \qquad (2.22b)$$

Next an equivalency between the series lumped inductance (L_T) and a lossless transmissiom line section is derived. Referring to Figure 2.4b, we define equivalent

impedances, Z_{eq}, with respect to the shunt capacitance C_T. The load impedance Z_L is equivalent to the characteristic impedance Z_0. Therefore, the equivalent impedance yields

$$Z_{eq} = Z_L + j\omega L_T. \qquad (2.23a)$$

Using (2.15), the n-th section input impedance for a lossless ($\alpha = 0$), high impedance transmission-line section is

$$Z_n = \frac{Z_{n+1} + j Z_0 \tan(\beta l)}{1 + j\dfrac{Z_{n+1}}{Z_0} \tan(\beta l)}. \qquad (2.23b)$$

Assuming $|\beta l| \ll 1$, the input impedance can be approximated by

$$Z_n \approx Z_{n+1} + j Z_0 (\beta l). \qquad (2.23c)$$

Equation (2.23c) is now equated to the equivalent input impedance Z_{eq}.
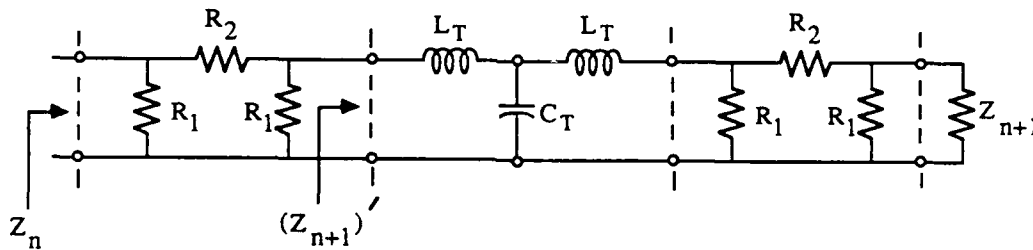
Figure 2.4(a) Equivalent T-network equivalent circuit

Assuming a small section length and taking the imaginary terms in (2.23a) and (2.23c) into account yields

$$L_T \approx Z_0 \left(\frac{\beta l}{\omega} \right) = Z_0 \, t_d \qquad (2.24)$$

where t_d is the propagation delay through the lossless transmission-line section.

18

Each lumped inductance L_T can now be replaced by an equivalent distributed transmission line as shown in Figure 2.5.
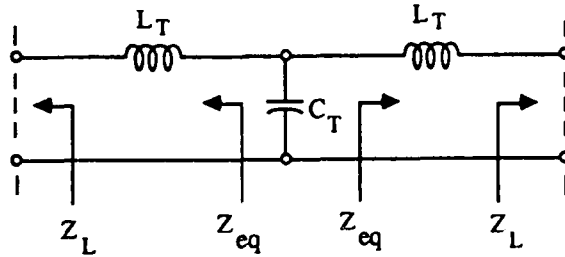
Figure 2.4(b) Equivalent T-network equivalent circuit (continued)
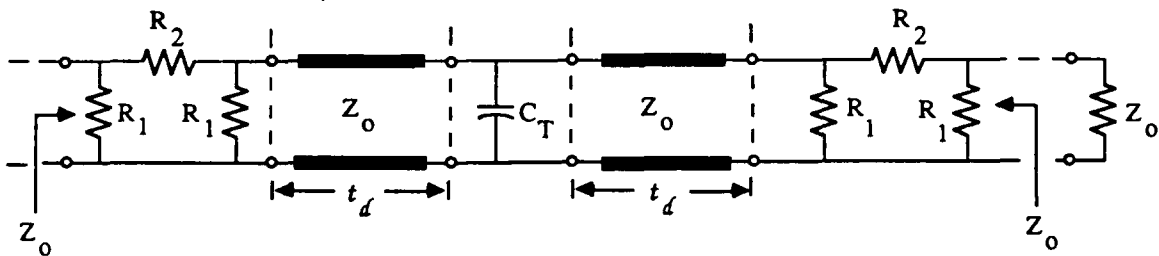
Figure 2.5 Lumped-distributed equivalent circuit model

The accuracy of the circuit model is dependent on the microstrip line length l, and the maximum frequency bandwidth ω_{max} of the propagating transient signal. The equivalent lumped-distributed circuit presented in this section is valid for electrically short, high impedance transmission lines which satisfy the conditions $t_d \ll 1/\omega_{max}$ and $|\beta l| \ll 1$.

E. ESTIMATION OF CHARACTERISTIC IMPEDANCE

Picosecond pulses propagating on the IC interconnections are described as finite energy signals and their maximum cumulative energy is defined by [Ref. 31: p. 35]

$$E_{max_l} = \sum_{n=-\infty}^{+\infty} |v^+[l,n]|^2 \tag{2.25}$$

where $v^+[l,n]$ is the sampled right-propagating voltage measured at the l-th length along the microstrip. To discuss pulse propagation on a lossy microstrip line, we first obtain the transmission-line equations by applying Kirchoff's voltage and current laws to the alternative distributed equivalent circuit as shown in Figure 2.6. When low-loss, high frequency conditions are assumed, the general solution for the voltage and current at the l-th length is solved as [Ref. 32: pp. 437-445]

$$v(l,t) = v^+\left(t - \frac{l}{v_g}\right) + v^-\left(t + \frac{l}{v_g}\right) \tag{2.26a}$$

$$i(l,t) = \frac{1}{Z_0}\left[v^+\left(t - \frac{l}{v_g}\right) + v^-\left(t + \frac{l}{v_g}\right)\right] \tag{2.26b}$$

where the superscripts (+) and (-) denote the right- and left-propagating voltage waves, respectively. When we compare these equations, the right-propagating current and voltage are given by

$$i^+(l,t) = \frac{1}{Z_0}v^+\left(t - \frac{l}{v_g}\right) \tag{2.27a}$$

$$v^+(l,t) = v^+\left(t - \frac{l}{v_g}\right) \tag{2.27b}$$

where v_g is the group velocity. The instantaneous power associated with the right-propagating wave is

$$p^+(l,t) = v^+(l,t)\, i^+(l,t) \tag{2.28a}$$

$$= \frac{\left[v^+\left(t - \frac{l}{v_g}\right)\right]^2}{Z_0} \tag{2.28b}$$

Since the pulse rise time is very fast (< 10 ps), the derivative of the cumulative energy curve (i.e. the instantaneous power) is approximately constant. Therefore, the maximum power of a causal, transient pulse is given by

$$P_{max} \approx \frac{1}{N} \sum_{n=0}^{N} |v^+[l,n]|^2 \qquad (2.29)$$

where N is the number of voltage sample values. By equating (2.28b) and (2.29), we have the characteristic impedance given by

$$Z_0 = \frac{|v^+[l,n]_{peak}|^2}{P_{max}} \qquad (2.30)$$

where $v^+[l,n]_{peak}$ is the peak amplitude voltage sample of the propagating pulse.

(Lumped-elements expressed as per unit length)
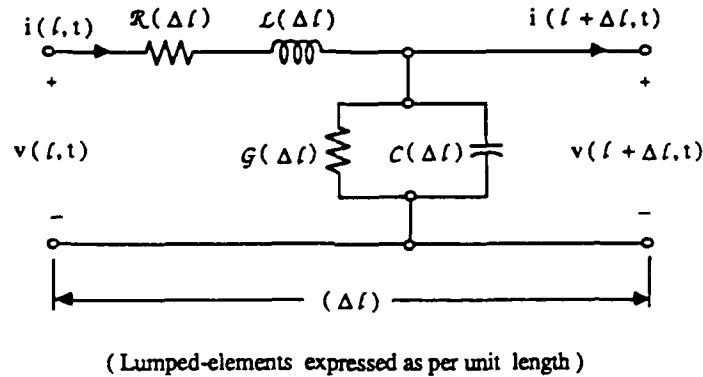
Figure 2.6 Lossy transmission line equivalent circuit (After Ref. 32)

In summary, distributed-lumped equivalent circuit models were derived for an electrically short length of lossy microstrip transmission line. The lumped circuit elements are evaluated at the maximum frequency of a bandlimited input signal. The validity of the equivalent circuit models are controlled by the physical length of the microstrip line. Therefore, we are interested in picosecond pulse widths and specific IC interconnections lengths which satisfy the lumped-element modeling criterion. Chapter III will use the proposed circuit models as a foundation to derive the parametric models for an IC interconnection.

21

III. PARAMETRIC MODELING

The rationale for using a parametric modeling approach to approximate a microstrip transmission line is intimately related to the identification of the physical microstrip properties. This chapter will present both autoregressive moving-average (ARMA) and autoregressive (AR) models of the equivalent reactive networks previously derived for the IC interconnection. A second objective is to show how the model parameters are related to the effective microstrip permittivity ϵ_{eff}, the characteristic impedance Z_0, and the propagation group delay τ_g of the microstrip structure.

A. RATIONAL TRANSFER FUNCTION MODELS

1. ARMA Parametric Model

In this model, the discrete-time input sequence $x[n]$, and the microstrip section output sequence $y[n]$, are related by the linear difference equation [Ref. 31]

$$y[n] = \sum_{k=0}^{q} b_k x[n-k] - \sum_{k=1}^{p} a_k y[n-k]. \tag{3.1}$$

where b_k are the moving-average (MA) model parameters and a_k are the autoregressive (AR) model parameters. The flowgraph representation of (3.1) is shown in Figure 3.1. This difference equation describes an ARMA model of order (p, q) and the corresponding system transfer function is

$$H_{ARMA}(z) = \frac{\sum_{k=0}^{q} b_k z^{-k}}{1 - \sum_{k=1}^{p} a_k z^{-k}} = \frac{B(z)}{A(z)} \tag{3.2}$$

2. AR Parametric Model

When all the b_k coefficients, except $b_0 = 1$, are zero in the ARMA model, equation (3.1) reduces to

$$y[n] = x[n] - \sum_{k=1}^{p} a_k y[n-k] \tag{3.3}$$

and the corresponding AR or all-pole transfer function is given by [Ref. 33: p.111]

$$H_{AR}(z) = \frac{1}{1 - \sum_{k=1}^{p} a_k z^{-k}} = \frac{1}{A(z)}. \tag{3.4}$$
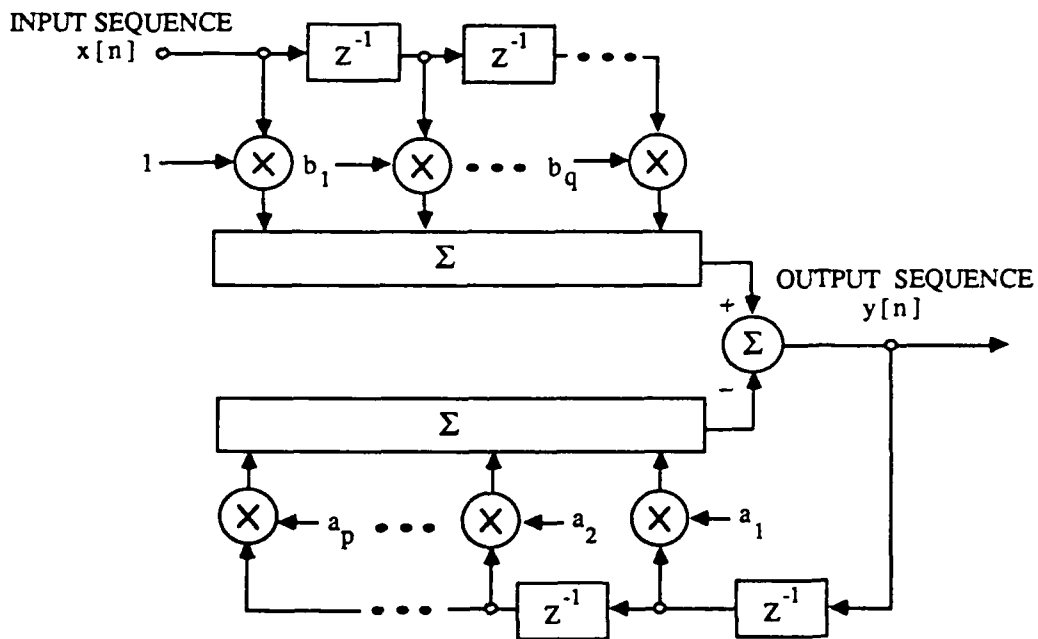
Figure 3.1 Realization of the ARMA/AR parametric models

In Figure 3.1, a flowgraph realization of this model is shown by the weighted feedback signal path.

B. IC INTERCONNECTION PARAMETRIC MODELS

1. Derivation of the ARMA Model

The network transmission function for the reactive π-network of Figure 2.3 yields

$$H(s) = \frac{\omega_0^2}{s^2 + 2\zeta\omega_0 s + \omega_0^2} \tag{3.5}$$

where $\omega_0 = (L_\pi C_\pi)^{-0.5}$ and $\zeta = (2Z_0 C_\pi \omega_0)^{-1}$. This network function describes a bandlimited frequency response for a second-order lowpass filter. Here we use the impulse invariant design method to transform (3.5) into a digital transfer function [Ref. 34]. Equation (3.5) can be expressed in the partial-fraction expansion form as

$$H(s) = \sum_{k=1}^{2} \frac{C_k}{s - d_k} \tag{3.6}$$

where

$$C_{1,2} = \frac{\omega_0}{2\sqrt{1 - \zeta^2}} \; e^{\pm\pi/2}$$

and the complex poles are

$$d_{1,2} = -\zeta\omega_0 \pm j\omega_0 \sqrt{1 - \zeta^2}.$$

Taking the inverse Laplace transform, the corresponding unit impulse response becomes

$$h(t) = \sum_{k=1}^{2} C_k e^{d_k t} \quad \text{for} \quad t \geq 0 \tag{3.7a}$$

and its discrete representation is

$$h[n] = \sum_{k=1}^{2} C_k e^{d_k n T} \tag{3.7b}$$

where T is the sampling interval.

It should be observed that for high sampling rates (say, T = 1.25 ps) the digital filter has an extremely high gain. For this reason (3.7b) is expressed as

$$h[n] = T \sum_{k=1}^{2} C_k e^{d_k nT}. \tag{3.8}$$

The digital transfer function is then obtained by taking the z-transform of (3.8) as:

$$H_{ARMA}(z) = \sum_{k=1}^{2} \frac{T C_k}{1 - e^{d_k T} z^{-1}}. \tag{3.9}$$

After rearranging the terms and simplifying, we have

$$H_{ARMA}(z) = \frac{b_1 z^{-1}}{1 - a_1 z^{-1} - a_2 z^{-2}} \tag{3.10}$$

where the filter coefficients, also called the ARMA model parameters, are:

$$b_1 = \frac{\omega_0 T}{\sqrt{1 - \zeta^2}} e^{-\zeta \omega_0 T} \cos\left(\frac{\pi}{2} - \omega_0 \sqrt{1 - \zeta^2}\, T\right) \tag{3.11a}$$

$$a_1 = 2\, e^{-\zeta \omega_0 T} \cos\left(\omega_0 \sqrt{1 - \zeta^2}\, T\right) \tag{3.11b}$$

$$a_2 = -e^{-2\zeta \omega_0 T}. \tag{3.11c}$$

The filter coefficient b_1 is directly linked to the AR filter coefficients a_1 and a_2. Given a_2 and the sampling period T, (3.11c) yields $\zeta \omega_0$. Substituting this result into (3.11b), a value for $\omega_0 \sqrt{1 - \zeta^2}$ can be found. Finally, specific values for ω_0 and ζ are easily determined and the numerator filter coefficient b_1 can be calculated. Therefore, the MA model parameter in (3.10) can be obtained from the AR model parameter estimates. In Chapter IV we will take advantage of this computational result in our discussion of parameter estimation algorithms.

2. Derivation of the AR Model

The AR parametric model is derived from the lumped-distributed equivalent circuit model of Figure 2.5. A network reflection function $\Gamma(s)$ is solved as [Ref. 35]

$$\Gamma(s) = \frac{Y_0(s) - Y_L(s)}{Y_0(s) + Y_L(s)} \tag{3.12}$$

where the equivalent admittances are given by

$$Y_0(s) = \frac{1}{Z_0}$$
$$Y_L(s) = Y_C(s) + Y_0(s)$$
$$= sC_T + \frac{1}{Z_0}.$$

After simpilfying and rearranging (3.12), we have

$$\Gamma(s) = -\frac{s\left(\dfrac{C_T}{2}\right) Z_0}{1 + s\left(\dfrac{C_T}{2}\right) Z_0}. \tag{3.13}$$

The network transmission function is then defined as

$$T(s) = 1 + \Gamma(s). \tag{3.14}$$

By substituting (3.13) into (3.14), a first-order, single time constant transfer function is achieved:

$$T(s) = \frac{\delta}{s + \delta} \tag{3.15}$$

where $\delta = \left(\dfrac{2}{Z_0 C^-}\right)$. Taking the inverse Laplace transform yields the unit impulse response

$$h_{AR}(t) = \delta e^{-\delta t} \quad \text{for} \quad t \geq 0. \tag{3.16}$$

The z-transform of the corresponding normalized sampled transmission impulse response is given by

$$H_{AR}(z) = \frac{1}{1 - e^{-T_n} z^{-1}} \quad \text{for} \quad |z| > |e^{-T_n}|. \tag{3.17}$$

26

where T_n is the normalized sampling interval. In order to satisfy the Nyquist sampling criterion, the sampling intervals of the normalized and denormalized transmission responses must be related by [Ref. 36: pp. 341-342]

$$T_n = \delta\, T\,.$$

(3.18)

To adjust the dc gain of (3.17) we can multiply the digital transfer function $H_{AR}(z)$ by the ratio of (3.15) evaluated at $s = 0$ to (3.17) evaluated at $z = 1$ (which is the dc value). Thus, the AR transfer function, after being adjusted for the dc gain, becomes

$$H_{AR}(z) = \frac{1 - e^{-T_n}}{1 - e^{-T_n}\, z^{-1}} \quad \text{for} \quad |z| > |e^{-T_n}|.$$

(3.19)

3. Effective Microstrip Permittivity

The effective microstrip permittivity is directly related to the ARMA model parameter a_2, the sampling interval T, and the physical microstrip length l. Using (3.11c), the propagation group delay is solved as [Ref. 18: p. 3]

$$\zeta\omega_0 = -\frac{2\,T}{\ln a_2}$$

(3.20a)

$$\tau_g = -\frac{2\,T}{(\ln a_2)\,(l)}$$

(3.20b)

where the group delay of the reactive network is $\tau_g = (2L_\pi C_\pi)^{-0.5}$. The propagation group delay can also be related to the effective microstrip permittivity by [Ref. 18: p. 62]

$$\tau_g = \frac{\sqrt{\epsilon_{eff}}}{c}.$$

(3.21)

Substituting (3.21) into (3.20b) yields the effective microstrip permittivity

$$\epsilon_{eff} = \left[\frac{2\,T\,c}{(\ln a_2)\,(l)}\right]^2.$$

(3.22)

27

We now derive an expression for the effective microstrip permittivity from the AR model parameter. From (3.19), we recognize the first-order AR filter coefficient is

$$a = e^{-T_n}.$$ (3.23)

The effective microstrip permittivity is now solved in terms of this AR model parameter and the propagation group delay:

$$\zeta = -\frac{T}{\ln a}$$ (3.24a)

$$\tau_g = -\frac{2\,T}{(\ln a)\,(l)}.$$ (3.24b)

Substituting (3.21) into (3.24b) yields the effective microstrip permittivity

$$\epsilon_{eff} = \left[\frac{2\,T\,c}{(\ln a)\,(l)}\right]^2.$$ (3.25)

4. Modeling Propagation Loss

Both the ARMA and AR digital transfer functions were derived from a lossless equivalent circuit. In order to properly characterize a picosecond pulse propagating on the IC interconnection, we must include a loss mechanism in the parametric models. The total propagation loss (in dB) experienced by a high-speed transient pulse will be defined by [Ref. 37: p. 7]

$$L_{dB} = 10\log_{10}\left[e^{-2\alpha_t\,l}\right]$$ (3.26)

where α_t is the total attenuation factor (in nepers/m) and l is the propagation distance (in meters) along the microstrip. The attenuation factor can be solved by combining the theoretical conductor and dielectric attenuation factors from (2.8b) and (2.10), respectively.

In summary, this chapter has presented ARMA and AR parametric models for a lossy dispersive microstrip transmission line. Analytical expressions were derived to relate the effective microstrip permittivity to the model parameters at a maximum frequency of interest. We have assumed no discontinuities on the IC interconnection because of impedance matching. In Chapter IV, we will extend the equivalent circuit and parametric models for a cascaded microstrip step discontinuity. Chapter V will present several parameter estimation algorithms which will be used to approximate the effective microstrip permittivity of the IC interconnection.

IV. MICROSTRIP DISCONTINUITY MODELING

Numerous approaches have been made to use equivalent circuits to model the microstrip discontinuities. Whinnery and Jamieson [Ref. 38] used Hahn's method to match electromagnetic-wave solutions across discontinuities, Oliner [Ref. 39] used Babinet's principle to describe stripline discontinuities, and Menzel and Wolff [Ref. 40] calculated the frequency-dependent properties of various microstrip discontinuities.

A discrete parametric method is presented in this chapter to model the reflection and transmission characteristics of a cascaded microstrip step discontinuity, assuming the quasi-TEM mode of propagation. Equivalent circuits are developed using the shunt capacitance circuit model presented by Gupta and Gopinath [Ref. 41]. Both reflection and transmission network functions are derived from the circuit models. ARMA and AR digital filters are described using discrete transformations of the respective network functions. This method has the advantage that complex microstrip circuits containing discontinuities can now be modeled by linear difference equations.

A. MICROSTRIP DISCONTINUITY EQUIVALENT CIRCUITS

1. Single Step Discontinuity

A single microstrip step discontinuity exists at the junction of two microstrip lines having different widths and characteristic impedances. This type of discontinuity is seen in the design of microwave matching transformers, couplers, filters and transitions [Ref. 41].

30

The geometric configuration of the step discontinuity and its equivalent circuit are shown in Figure 4.1.
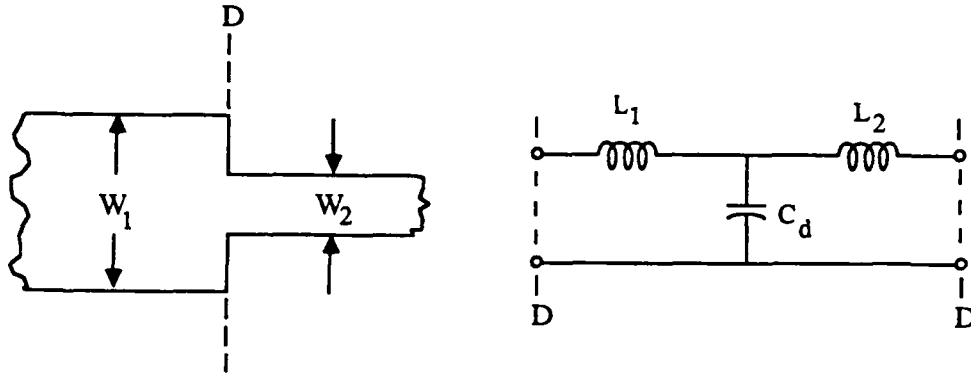
Figure 4.1 Microstrip step discontinuity and the equivalent circuit

The effect of the total discontinuity inductance (L_d) may be separated into L_1 and L_2 as

$$L_1 = \frac{L_{w1}}{L_{w1} + L_{w2}} L_d \qquad \text{(H)} \qquad (4.1a)$$

$$L_2 = \frac{L_{w2}}{L_{w1} + L_{w2}} L_d \qquad \text{(H)} \qquad (4.1b)$$

where L_{w1} and L_{w2} are the inductances per unit length for the microstrip of width W_1 and W_2 given by

$$L_{wm} = \frac{Z_{0m}\sqrt{\epsilon_{effm}}}{c}, \qquad m = 1,2 \quad \text{(H/m)} \qquad (4.2)$$

where Z_{0m} is the characteristic impedance and ϵ_{effm} is effective permittivity of the width W_m, and $c = 3 \times 10^8$ m/s. The closed-form expressions for C_d and L_d have been derived from curve fitting numerical results. These expressions are [Ref. 41]

$$\frac{C_d}{\sqrt{W_1 W_2}} = (10.1 \ \log \epsilon_r + 2.33)\frac{W_1}{W_2} - 12.6 \ \log \epsilon_r - 3.17 \quad \text{(pF/m)}$$

$$\text{(for } \epsilon_r \leq 10; \ 1.5 \leq W_1/W_2 \leq 3.5) \qquad (4.3a)$$

31

and

$$\frac{L_d}{h} = 40.5\left(\frac{W_1}{W_2} - 1.0\right) - 75\log\frac{W_1}{W_2} + 0.2\left(\frac{W_1}{W_2} - 1.0\right)^2 \quad \text{(nH/m)} \qquad (4.3b)$$

where ϵ_r is the relative dielectric constant and h is the substrate thickness. Equation (4.3a) yields a percentage of error less than 10 percent and equation (4.3b) has an error less than 5 percent for $W_1/W_2 \leq 5$ and $W_2/h = 1.0$.

2. Cascaded Step Discontinuity

The cascaded microstrip step discontinuity is formed by combining two single step discontinuities as shown in Figure 4.2(a). Short ($< \lambda_g/4$) lengths of high impedance (narrow width) microstrip line will behave predominantly as a series inductance (L_s). Whereas, a very short $\ll \lambda_g/4$ length of low impedance (wide width) line will act predominantly as a shunt capacitance (C_s) [Ref. 18: pp. 212-216]. End-inductances (L_e) are also introduced in the low impedance line as its length approaches a quarter-wavelength. The predominant series inductive reactance of the line of length l_2 is

$$\omega L_s = Z_{02}\sinh\left(\frac{2\pi l_2}{\lambda_{g2}}\right). \qquad (4.4)$$

Assuming the small-angle approximation such that $(2\pi l_2/\lambda_{g2} \ll \pi/4)$, equation (4.4) is approximated as

$$L_s \approx \frac{Z_{02}\, l_2}{f\lambda_{g2}} \qquad (4.5)$$

where the frequency-dependent microstrip wavelength is

$$\lambda_{g2} = \frac{c}{f\sqrt{\epsilon_{eff}(f)}}.$$

When high impedance widths (W_2) are equal, the equivalent circuit can be described by Figure 4.2(b).

The predominant shunt capacitive suspectance of the line of length l_1 is

$$\omega C_s = \frac{1}{Z_{01}} \sinh\left(\frac{2\pi\, l_1}{\lambda_{g1}}\right) \qquad (4.6)$$
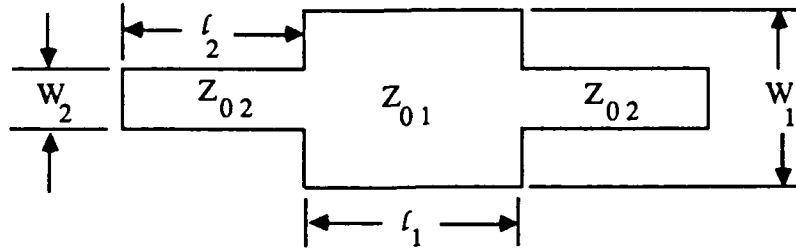
(a)
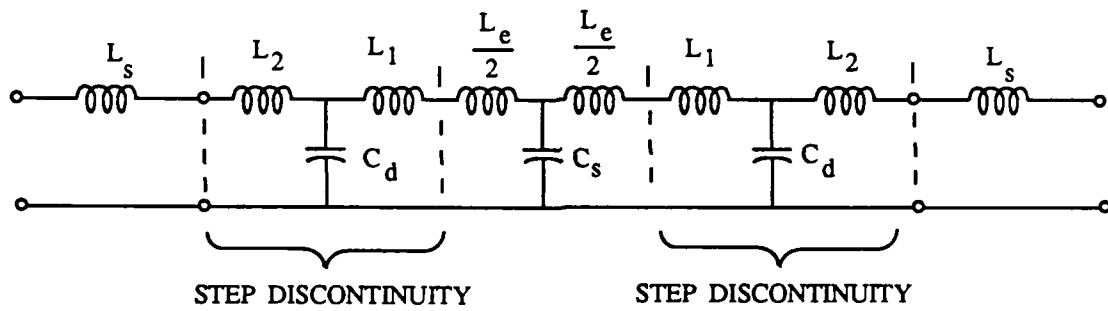
(b)

Figure 4.2 Cascaded Step Discontinuity and the Equivalent Circuit

and for $2\pi l_1/\lambda_{g1} \ll \pi/4$, the shunt capacitance is approximated by

$$C_s \approx \frac{l_1}{f\, Z_{01}\, \lambda_{g1}}. \qquad (4.7)$$

Similarly, the end-inductances are obtained as

$$L_e \approx \frac{Z_{01}\, l_1}{f\, \lambda_{g1}}. \qquad (4.8)$$

33

The relatively low characteristic impedance Z_{01} will cause a very small inductive effect (L_{w1}) at each step discontinuity. Therefore, at frequencies up to a few gigahertz, the inductance L_1 in the equivalent circuit can be neglected [Ref.18: p. 217]. A modified equivalent circuit is formed by converting the low impedance equivalent T-network into a π-network as shown in Figure 4.3(a). The shunt capacitances $C_s/2$ and the discontinuity capacitances C_d are added to form C_π. Also, each step discontinuity inductance L_2 is combined with their adjacent series inductance L_s to form a new inductance L_h. Assuming very short microstrip lengths and from (2.24), the new inductance can be approximated as a lossless, distributed transmission line section having a characteristic impedance of Z_{02} and a time delay approximated by

$$t_d \approx \frac{L_h}{Z_{02}}. \tag{4.9}$$

Figures 4.3(b) and 4.3(c) show the complete lumped-distributed equivalent circuits for the cascaded microstrip step discontinuity.
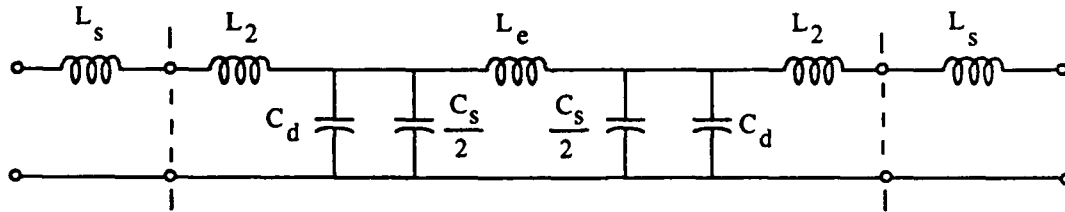
(a)
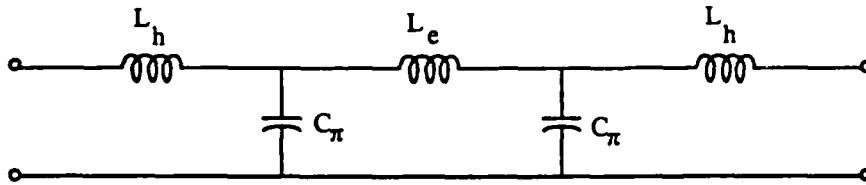
(b)

Figure 4.3 Modified cascaded step discontinuity equivalent circuit
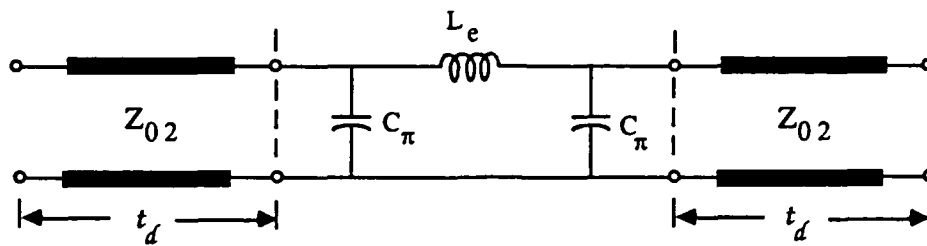
(c)

Figure 4.3 Modified cascaded step discontinuity equivalent circuit (continued)

3. Capacitive Shunt Equivalent Circuit Model

An alternative equivalent circuit is presented that is designed to yield an "all-pole" transmission network function. The equivalent π-network of Figure 4.3(b) is converted into a T-network and the series inductances are combined as shown in Figure 4.4(a). The combined inductances are approximated as lossless, distributed transmission line sections having time delays of

$$t_d' = \frac{(2L_h + L_e)}{2Z_{02}}. \tag{4.10}$$

The shunt capacitance equivalent circuit model is shown in Figure 4.4(b) where t_d' represents the propagation delay time.
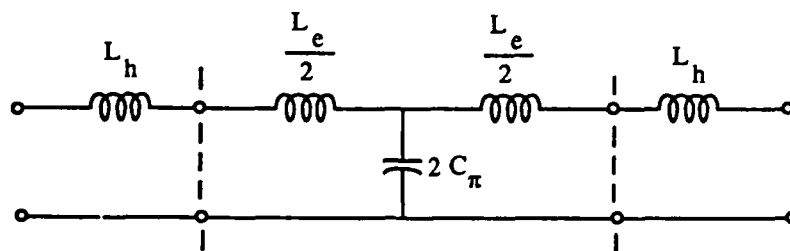
(a)

Figure 4.4 Capacitive shunt equivalent circuit

35
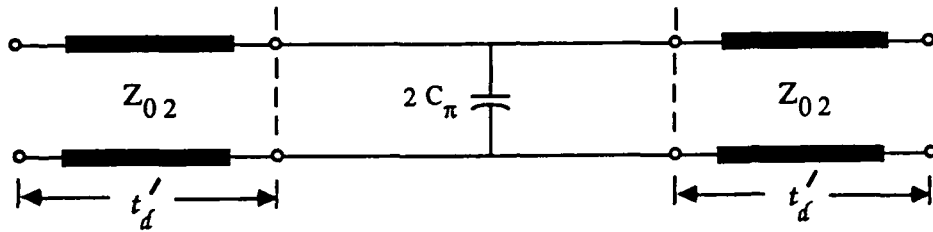
(b)

Figure 4.4 Capacitive shunt equivalent circuit (continued)

4. Modeling Propagation Loss

Chapter II presented a resistive π-network attenuator to model the total propagation loss in a single microstrip line section. This scheme will again be used for the equivalent circuits of Figures 4.3(c) and 4.4(b). Figure 4.5 illustrates how the half-symmetrical losses of the cascaded microstrip step discontinuity are modeled. Using (2.8b) and (2.10), a total propagation loss can be obtained for the microstrip.
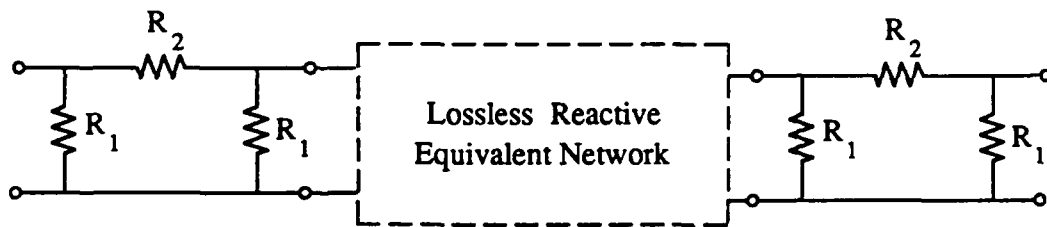
Figure 4.5 Lossy cascaded microstrip step equivalent circuit

Next, we equally represent the total loss by two identical resistive π-networks as shown in Figure 4.5.

B. PARAMETRIC MODELS FOR MICROSTRIP DISCONTINUITIES

1. Reflection and Transmission Network Functions

The characteristic impedance mismatch caused by the abrupt change in the width dimension will produce both reflected and transmitted traveling voltage waveforms. The objective of this section is to derive reflection and transmission network functions which accurately characterize the cascaded microstrip step discontinuity propagation effects. Initially, a third-order transmission network function is derived from the equivalent circuit shown in Figure 4.3(c). This network function is transformed into an ARMA model. Next, a first-order approximation is solved from the single capacitive shunt equivalent circuit of Figure 4.4(b). This single-impedance, single-capacitor network function is then transformed into an AR model.

a. Third-Order Transmission Function

The reflection network function for the π-network of Figure 4.3(c), expressed in the complex s-domain, is defined as [Ref. 38: p.217]

$$\Gamma(s) = \frac{Y_{02}(s) - Y_L(s)}{Y_{02}(s) + Y_L(s)} \tag{4.11}$$

where the admittances $Y_{02}(s)$ and $Y_L(s)$ are obtained as indicated in Figure 4.6.
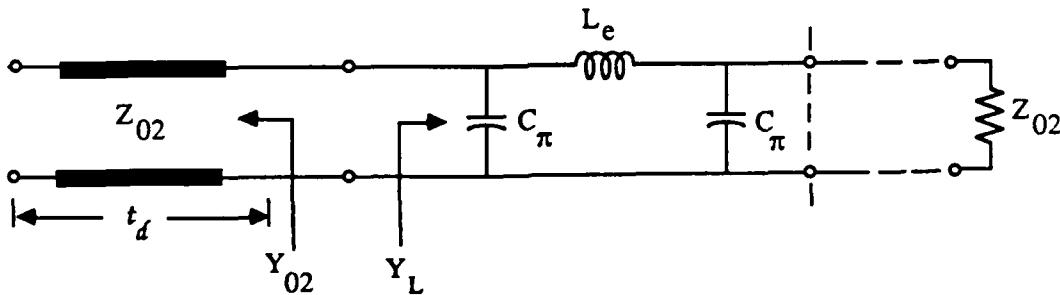
Figure 4.6 Characteristic and load admittances

Substituting for $Y_{02}(s)$ and $Y_L(s)$ in (4.11) and manipulating the resultant expression yields

$$\Gamma_3(s) = -\frac{(C_\pi^2 L_e Z_{02}^2)s^3 + (2C_\pi Z_{02}^2 + L_e)s}{(C_\pi^2 L_e Z_{02}^2)s^3 + (2C_\pi L_e Z_{02})s^2 + (2C_\pi Z_{02}^2 + L_e)s + 2Z_{02}} \qquad (4.12)$$

where the subscript (3) denotes a third-order network function. The transmission function is defined as [Ref. 38: p. 217]

$$T_3(s) = 1 + \Gamma_3(s). \qquad (4.13)$$

Substituting (4.12) into (4.13) yields

$$T_3(s) = \frac{\left(\dfrac{2}{C_\pi Z_{02}}\right)s^2 + \left(\dfrac{2}{C_\pi^2 Z_{02}^2}\right)s + \left(\dfrac{2}{C_\pi^2 L_e Z_{02}}\right)}{s^3 + \left(\dfrac{2}{C_\pi Z_{02}}\right)s^2 + \left(\dfrac{2C_\pi Z_{02}^2 + L_e}{C_\pi^2 L_e Z_{02}^2}\right)s + \left(\dfrac{2}{C_\pi^2 L_e Z_{02}}\right)}. \qquad (4.14)$$

b. First-Order Reflection and Transmission Functions

A first-order approximation of the reflection network function is determined by solving (4.11) for the equivalent circuit of Figure 4.4(b). Evaluating (4.11) yields

$$\Gamma_1(s) = -\frac{s(C_\pi Z_{02})}{1 + s(C_\pi Z_{02})} \qquad (4.15a)$$

and the transmission network function becomes

$$T_1(s) = \frac{1}{1 + s(C_\pi Z_{02})}. \qquad (4.15b)$$

2. ARMA/AR Models for the Cascaded Step Discontinuity

a. Autoregressive Moving-Average Parametric Model

The first step is to perform a partial fraction expansion of equation (4.14). The s-domain expansion is generalized as

$$T_3(s) = \frac{K_1}{(s - d_1)} + \frac{K_2 e^{j\theta}}{(s - d_2)} + \frac{K_2 e^{-j\theta}}{(s - d_2^*)} \qquad (4.16)$$

38

where the three poles are:

$$d_1 = -\frac{1}{C_\pi Z_{02}}$$

$$d_2 = -\sigma + j\omega$$

$$d_2^* = -\sigma - j\omega.$$

Using the impulse-invariant design method, a digital filter transfer function is obtained from (4.16) as

$$T_3(z) = \frac{K_1}{1 - e^{-d_1 T} z^{-1}} +$$

$$\frac{2K_2 \cos(\theta) - 2K_2 e^{-\sigma T} z^{-1} \cos(\theta - \omega T)}{1 - 2e^{-\sigma T} \cos(\omega T) z^{-1} + e^{-d_1 T} z^{-2}.} \tag{4.17}$$

After considerable complex algebra the generalized ARMA transfer function becomes

$$T_3(z) = \frac{b_0 + b_1 z^{-1} + b_2 z^{-2}}{1 - a_1 z^{-1} - a_2 z^{-2} - a_3 z^{-3}} \tag{4.18}$$

where

$$b_0 = K_1 + 2K_2 \cos(\theta)$$

$$b_1 = -2 \left[K_2 e^{-d_1 T} \cos(\theta) + e^{-\sigma T} \left(K_1 \cos(\omega T) + K_2 \cos(\theta - \omega T) \right) \right]$$

$$b_2 = e^{-d_1 T} \left[K_1 + 2K_2 e^{-\sigma T} \cos(\theta - \omega T) \right]$$

$$a_1 = 2e^{-\sigma T} \cos(\omega T) + e^{-d_1 T}$$

$$a_2 = - \left[2e^{-(\sigma + d_1)T} \cos(\omega T) + e^{-d_1 T} \right]$$

$$a_3 = e^{-2d_1 T}.$$

The most significant filter coefficient a_3 identifies the time constant $(Z_{02} C_\pi)$ of the network. In terms of the sampling interval T, this filter coefficient is

$$a_3 = \exp \left(-\frac{2T}{C_\pi Z_{02}} \right). \tag{4.19}$$

A reflection digital transfer function is obtained from the bilinear transformation of equation (4.15a) as [Ref. 34: pp.206-211]

$$\Gamma_1(z) = \Gamma_1(s)\Big|_{s = \frac{2}{T}\left(\frac{1 - z^{-1}}{1 + z^{-1}}\right)}$$

$$\Gamma_1(z) = -\frac{2C_\pi Z_{02}(1 - z^{-1})}{(T + 2C_\pi Z_{02}) + (T - 2C_\pi Z_{02})z^{-1}}$$

$$\Gamma_1(z) = \frac{b_0'(z^{-1} - 1)}{1 + a_1 z^{-1}}. \tag{4.20a}$$

and the transmission transfer function is evaluated as

$$T_1(z) = \frac{T(1 + z^{-1})}{(T + 2C_\pi Z_{02}) + (T - 2C_\pi Z_{02})z^{-1}}$$

$$T_1(z) = \frac{b_0(1 + z^{-1})}{1 + a_1 z^{-1}} \tag{4.20b}$$

which is a 1st-order ARMA model. The parameters are defined as follows:

$$b_0 = \left(\frac{T}{T + 2C_\pi Z_{02}}\right),$$

$$b_0' = \left(\frac{2C_\pi Z_{02}}{T + 2C_\pi Z_{02}}\right),$$

and

$$a_1 = \left(\frac{T - 2C_\pi Z_{02}}{T + 2C_\pi Z_{02}}\right)$$

b. Autoregressive Parametric Model

A first-order AR digital filter of the transmission network function is obtained using the matched z-transform design method. The single pole of equation (4.15b) is directly related to the pole of the AR transfer function [Ref. 42: pp. 666-667] as

$$T_{AR}(z) = \frac{\left(\dfrac{T}{C_\pi Z_{02}}\right)}{1 - e^{-\left(\frac{T}{C_\pi Z_{02}}\right)}z^{-1}}. \tag{4.21}$$

40

c. Realization of the Lossy Parametric Model

The proposed ARMA/AR reflection and transmission transfer functions were derived from *lossless* reactive networks. The propagation losses which are associated with both the low and high impedance microstrip lines must be included in the parametric models. These losses are represented as constant "loss" multipliers. The value of the multiplier is defined by

$$L = \exp\left[-(\alpha_t \, l)\right] \qquad (4.22)$$

where l represents the microstrip line length and α_t is the total attenuation factor in nepers per unit length. Figure 4.7 describes the lossy parametric model for the cascaded microstrip step discontinuity.

3. Parametric Models for Multiple Discontinuities

In this section a parametric model is developed for a multi-section microstrip structure described by a combination of cascaded step discontinuities. Wave propagation in the multi-section microstrip structure exhibits several of the physical characteristics of the multi-layered earth model developed in geophysical signal processing [Ref. 35: pp. 306-315]. Similarly, two different propagating waves exist within each microstrip section, an incident (right-propagating) wave and a reflected (left-propagating) wave. Unlike the lossless multi-layered earth model, propagating signals in microstrip are influenced by frequency-dependent losses and dispersion. Energy conservation is established across each discontinuity boundary. However, energy loss will occur between adjacent discontinuities. A linear time-invariant system is used to describe each discontinuity boundary. At each discontinuity an incident signal is partially reflected and partially transmitted into the next section. A proportional response of each component is given by the concurrent convolution of the incident signal with both a reflected and a transmitted impulse response of the linear system. A lattice-like system flowgraph relating right-propagating $v_m^{\pm}(z)$,

41

and left-propagating $v_m^-(z)$ signals at the m-th discontinuity boundary is shown in Figure 4.8. The reflection transfer function $\Gamma_m(z)$
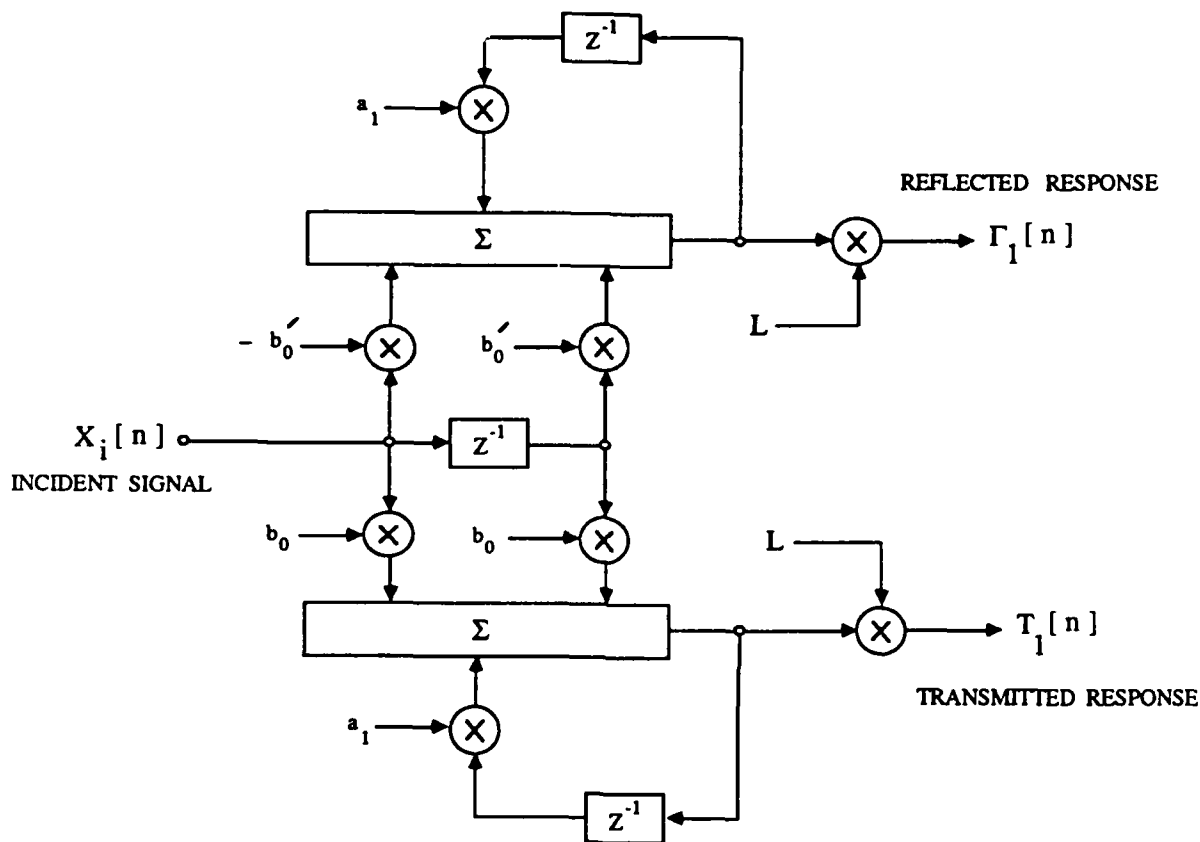
Figure 4.7 1st-order ARMA model realization of the cascaded step discontinuity

and the transmission transfer function $T_m(z)$ are the 1st-order ARMA models of (4.20a) and (4.20b), respectively. The overall parametric model for multiple discontinuities may then be constructed by using the lattice as building blocks, and interconnecting the lattice sections with lossy delay lines. Figure 4.9 describes two adjacent discontinuity sections of a multi-section structure. Here an incident voltage

sequence $v_m^{(+)'}[n]$ initially enters a lossy delay line $D_m(z)$, and a reflected voltage sequence $v_m^{(-)'}[n]$ is the resultant outcome after multiple reflections from the other discontinuities.
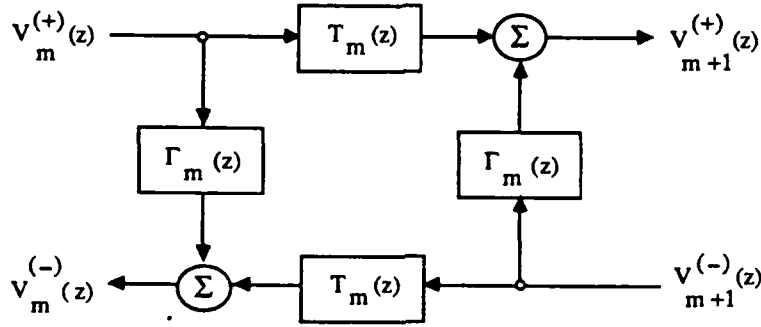
Figure 4.8 Discontinuity lattice configuration

The flowgraph of the model shows an interaction of right- and left-propagating waves through the multi-section structure. We will characterize the lossy delay line for an m-th section by the transfer function

$$D_m(z) = e^{-[\alpha_t^{(m)} l_m]} z^{-T_m} \tag{4.23}$$

where $\alpha_t^{(m)}$ is the m-th section attenuation factor, l_m the section length, and T_m is the discrete-time propagation delay per section.

In summary, both equivalent circuit and ARMA/AR parametric models were presented for a cascaded microstrip step discontinuity. Losses were included in the circuit model by resistive π-networks. Corresponding lossless reflection and transmission network functions were derived from the reactive networks. Next,

discrete transformations were performed on the network functions to derive the ARMA/AR digital transfer functions. Multiple microstrip step discontinuities were modeled by cascading the lossy equivalent circuit of a single step discontinuity. A lattice-like 1st-order ARMA model was introduced to describe a multi-section microstrip structure. In Chapter VI, transient analysis simulations of the equivalent circuit models will be compared with experimental measurements to validate
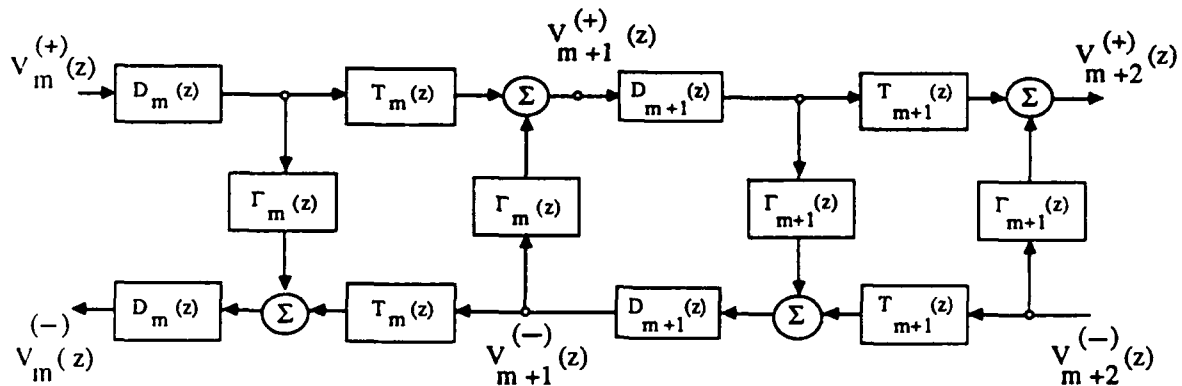
Figure 4.9 Multi-section lattice model

the accuracy of the circuit models. In the next chapter, we will develop several parameter estimation algorithms, and introduce new system identification techniques for multi-section microstrip structures.

V. PARAMETER ESTIMATION ALGORITHMS

The parameter estimation algorithms presented are based upon deterministic and stochastic methods. Figure 5.1 describes an unknown system to be identified. The observable input and output signals can be either deterministic or stochastic. The ARMA and/or AR model parameters of the unknown system are determined by the parameter estimation algorithms. Additionally, simulation results are presented to study the performance of the algorithms.
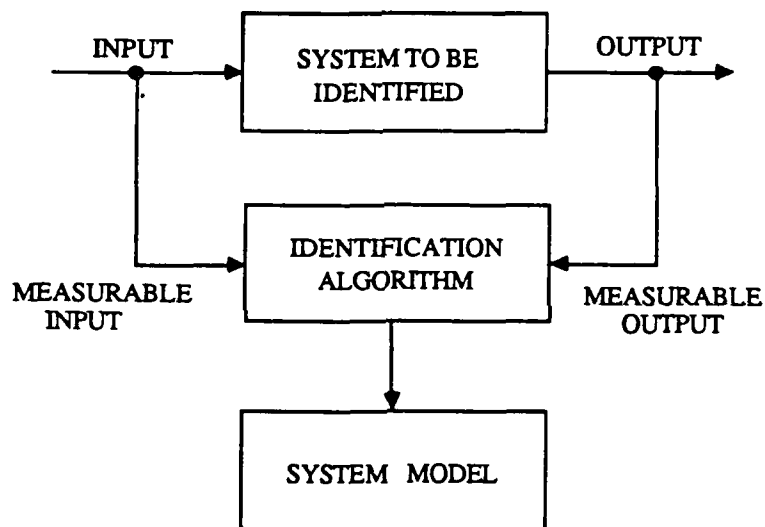
Figure 5.1 Block diagram representation of the p′ ımeter estimation problem

The deterministic methods to be presented are the weighted least squares (WLS) algorithm, the network function approximation method, and the Schur algorithm. The WLS algorithm is a method for finding the filter coefficients of a p-th order recursive digital filter, ·vhich gives an optimum least squares approximation to a known sample impulse response. The network function method approximates an s-domain network function from the unit step response characteristics, such as rise and delay times, of a propagating pulse. Finally, the Schur algorithm estimates

the AR model parameters from a given sample impulse response. Our emphasis will focus on the deterministic methods because avaliable microwave measurement techniques have deterministic excitation sources.

In the discussion of the stochastic methods we assume that a nearly white wideband microwave noise source excites the microstrip structure. When the noise source and the output random data are both available for signal processing, an ARMA parameter estimation algorithm based on a generalized Mullis-Roberts (M-R) criterion is used [Ref. 15]. However, if the input noise source cannot be measured, an estimate of the driving source can be obtained from the output process. This restriction in observable data precludes the direct application of the general estimators. Therefore, a suboptimal *two-stage* least squares ARMA estimation algorithm will be presented to solve this problem.

In Chapter IV, we presented a lattice parametric model for the multi-section microstrip discontinuity. New algorithms will now be introduced that will estimate the ARMA/AR parameters for this model using reflected and transmitted time-domain measurements.

A. DETERMINISTIC PARAMETER ESTIMATION

1. Weigthed Least Squares (WLS) Algorithm

a. WLS Algorithm Derivation

Evans and Fischl [Ref. 43] presented a computational algorithm for estimating the coefficients of a pth-order ARMA digital filter whose unit impulse response best approximates, in a minimum mean-square error sense, a prescribed impulse response of finite length. Here we derive a slightly modified version of their original least squares solution to estimate the ARMA parameters.

The transfer function $H_{ARMA}(z)$ of (3.2) can be expressed in terms of samples of the impulse response

$$H_{ARMA}(z) = h_0 + h_1 z^{-1} + h_2 z^{-2} + \dots . \qquad (5.1)$$

The first m samples of the estimated impulse response forms the m-vector

$$\hat{\underline{h}} = \begin{bmatrix} \hat{h}_0 \\ \hat{h}_1 \\ \vdots \\ \hat{h}_{m-1} \end{bmatrix} \tag{5.2}$$

and the m samples of the prescribed impulse response is

$$\underline{h} = \begin{bmatrix} h_0 \\ h_1 \\ \vdots \\ h_{m-1} \end{bmatrix} . \tag{5.3}$$

The error vector is defined by

$$\underline{e} = \underline{h} - \hat{\underline{h}} . \tag{5.4}$$

By long division of (3.2), we can relate the AR and MA parameters (a, b) to the estimated impulse response $\hat{\underline{h}}(a, b)$ as

$$\begin{bmatrix} -\dfrac{b}{0} - \end{bmatrix} = \begin{bmatrix} -\dfrac{\hat{H}_1}{\hat{H}_2} -- \end{bmatrix} \begin{bmatrix} \underline{a} \end{bmatrix} \tag{5.5a}$$

where

$$\underline{b} = \begin{bmatrix} b_0 \\ b_1 \\ \vdots \\ b_{p-1} \end{bmatrix} \quad \text{and} \quad \underline{a} = \begin{bmatrix} a_0 \\ a_1 \\ \vdots \\ b_p \end{bmatrix} \tag{5.5b}$$

$$[\widehat{H_1}] = \begin{bmatrix} \hat{h}_0 & 0 & \dots & 0 & 0 \\ \hat{h}_1 & \hat{h}_0 & \dots & 0 & 0 \\ \vdots & \vdots & \ddots & \vdots & \vdots \\ \hat{h}_{p-1} & \hat{h}_{p-2} & \dots & \hat{h}_0 & 0 \end{bmatrix} \tag{5.5c}$$

$$[\widehat{H_2}] = \begin{bmatrix} \hat{h}_p & \hat{h}_{p-1} & \dots & \hat{h}_0 \\ \hat{h}_{p+1} & \hat{h}_p & \dots & \hat{h}_1 \\ \vdots & \vdots & \ddots & \vdots \\ \hat{h}_{m-1} & \hat{h}_{m-2} & \dots & \hat{h}_{m-p-1} \end{bmatrix} . \tag{5.5d}$$

A least squares solution can be determined by minimizing

$$\| \underline{e}\,(a, b) \| = \left[\sum_{i=0}^{m-1} e_i(a, b)^2 \right]^{1/2} \tag{5.6}$$

47

with respect to the coefficients (a, b).

Burrus and Parks [Ref. 44] have proposed a linear-equation error vector in the matrix formulation, given by

$$\underline{d}(a) = [H_2]\, \underline{a} \tag{5.7a}$$

where

$$\underline{d}(a) = \begin{bmatrix} d_1(a) \\ d_2(a) \\ \vdots \\ d_{m-p}(a) \end{bmatrix}. \tag{5.7b}$$

The error vector $\underline{e}(a, b)$ of (5.4) is related to $\underline{d}(a)$ by rearranging (5.7a) as

$$\underline{d}(a) = [B(a)]^T\, \underline{h} \tag{5.8}$$

where the $m \times (m - p)$ matrix

$$B(a) = \begin{bmatrix} a_p & 0 & \ldots & 0 \\ a_{p-1} & a_p & \ldots & 0 \\ \vdots & \vdots & \ddots & \vdots \\ a_0 & a_1 & \ldots & a_p \\ 0 & a_0 & \ldots & a_1 \\ \vdots & \vdots & \ddots & \vdots \\ 0 & 0 & \ldots & a_0 \end{bmatrix}. \tag{5.9}$$

We can substitute $\underline{h}$ of (5.4) into (5.8), and recognizing from the lower partition of (5.5a) that

$$[B(a)]^T\, \underline{h} = 0, \tag{5.10}$$

we have

$$\underline{d}(a) = [B(a)]^T\, \underline{e}(a, b). \tag{5.11}$$

An inverse relationship between the errors is formed using a transformation weighting matrix $[W(a)]$. Hence, the minimization problem of (5.6) can now be expressed as [Ref. 44]

$$\min_{a,b} \| \underline{e}(a, b) \| = \min_a \| [W(a)]\underline{d}(a) \| \tag{5.12}$$

where

$$[W(a)] = [B(a)][B(a)^T B(a)]^{-1}. \tag{5.13}$$

48

The computational algorithm begins with an initial estimate of $\underline{\hat{a}}^{(0)}$. Equation (5.7a) can be partitioned as

$$\underline{d}(\hat{a}) = \left[-\underline{f} \mid [X]\right] \underline{\hat{a}} \tag{5.14}$$

where

$$[X] = \begin{bmatrix} h_{p-1} & \cdots & h_0 \\ h_p & \cdots & h_1 \\ \vdots & \ddots & \vdots \\ h_{m-2} & \cdots & h_{m-p-1} \end{bmatrix} \tag{5.15}$$

$$\underline{f} = \begin{bmatrix} -h_p \\ -h_{p+1} \\ \vdots \\ -h_{m-1} \end{bmatrix} \tag{5.16}$$

and the AR parameter vector

$$\underline{\hat{a}} = \begin{bmatrix} a_1 \\ a_2 \\ \vdots \\ a_p \end{bmatrix} . \tag{5.17}$$

The least squares solution of $\underline{\hat{a}}$ yields

$$\underline{\hat{a}}^{(0)} = [X^T X]^{-1} X^T \underline{f} \tag{5.18}$$

The initial estimate equally weights the error vector $\underline{d}(\hat{a})$. However, the error formulation can be weighted differently depending upon the initial estimate. Then, the weighted least squares solution at the i-th iteration is given by

$$\underline{\hat{a}}^{(i)} = \left[X^T W\left(\underline{\hat{a}}^{(i-1)}\right)^T W\left(\underline{\hat{a}}^{(i-1)}\right) X\right]^{-1} \times$$

$$\left[X^T W\left(\underline{\hat{a}}^{(i-1)}\right)^T W\left(\underline{\hat{a}}^{(i-1)}\right) \underline{f}\right] \tag{5.19}$$

49

where the weighting matrix $\left[W\left(\hat{\underline{a}}^{(i-1)} \right) \right]$ is in terms of the previous estimate $\hat{\underline{a}}^{(i-1)}$. The iteration is continued until $\hat{\underline{a}}^{(i)} \approx \hat{\underline{a}}^{(i-1)}$. Using the optimal estimate for $\hat{\underline{a}}$, the weighted error $\underline{e}_w(a,b)$ is calculated by

$$\underline{e}_w(a,b) = \left[W\left(\hat{\underline{a}}^{(i)} \right) \right] \underline{d}\left(\hat{\underline{a}}^{(i)} \right).\tag{5.20}$$

From (5.4), the estimate $\hat{\underline{h}}(a,b)$ is given by

$$\hat{\underline{h}}(a,b) = \underline{h} - \underline{e}_w(a,b).\tag{5.21}$$

Finally, the numerator coefficient estimate vector $\hat{\underline{b}}$ is calculated directly by

$$\hat{\underline{b}} = [\widehat{H_1}]\,\hat{\underline{a}}.\tag{5.22}$$

b. Simulation Results

The weighted least squares algorithm was implemented using a Fortran program. Several reference models were estimated beginning with an ARMA order (3,2), denoting AR order $p = 3$, and MA order $q = 2$. The transfer function is

$$H(z) = \frac{0.5 - 0.4z^{-1} + 0.89z^{-2}}{1 - 0.20z^{-1} - 0.25z^{-2} + 0.05z^{-3}}.\tag{5.23}$$

The actual reference model parameters and the WLS algorithm parameter estimates are shown in Table 1. All results are obtained after one iteration of the algorithm using 20 samples of the impulse response.

Table 1. WLS SIMULATION (3,2) MODEL RESULTS

Parameter	Actual	Estimated
AR:	0.2000	0.2000
	0.2500	0.2500
	-0.0500	-0.0500
MA:	0.5000	0.5000
	-0.4000	-0.4000
	0.8900	0.8899

50

We next consider a second reference model with order (4,2) having transfer function

$$H(z) = \frac{1 + 0.2z^{-1} - 0.99z^{-2}}{1 - 0.20z^{-1} + 0.62z^{-2} - 0.152z^{-3} + 0.3016z^{-4}} \qquad (5.24)$$

and the obtained results are given in Table 2.

Table 2. WLS SIMULATION (4,2) MODEL RESULTS

Parameter	Actual	Estimated
AR:	0.2000	0.2002
	-0.6200	-0.6197
	0.1520	0.1529
	-0.3016	-0.3014
MA:	1.0000	1.0000
	0.2000	0.1998
	-0.9900	-0.9902

The final example is a strictly AR model of order (4,0) having a transfer function

$$H(z) = \frac{1}{1 - 0.20z^{-1} + 0.622z^{-2} - 0.151z^{-3} + 0.355z^{-4}} \, . \qquad (5.25)$$

The actual and estimated AR parameters are listed in Table 3.

Table 3. WLS SIMULATION (4,0) MODEL RESULTS

Parameter	Actual	Estimated
AR:	0.2000	0.2004
	-0.6220	-0.6221
	0.1510	0.1513
	-0.3550	-0.3551

The above examples demonstrate the estimation accuracy of the WLS algorithm for $(q < p)$ order models.

2. Network Function Approximation Method

The following method, introduced by Elmore [Ref. 45], can approximate the normalized network function from the unit step response delay and rise times. Assume that the microstrip section is excited by a unit step and that its step

response $v_2(t)$, has been normalized as $v_{2n}(t)$. The microstrip group delay time is then defined as

$$\tau_g = \frac{\displaystyle\int_0^\infty t\, v'_{2n}(t)dt}{\displaystyle\int_0^\infty v'_{2n}(t)dt} = \int_0^\infty t\, h_n(t)dt \qquad (5.26)$$

where $v'_{2n}(t) = h_n(t)$ is the normalized impulse response. The rise time is defined as

$$T_r = \sqrt{2\pi}\left[\int_0^\infty (t-\tau_g)^2\, h_n(t)dt\right]^{1/2},$$

$$= \sqrt{2\pi}\left[\int_0^\infty t^2\, h_n(t)dt - 2\,\tau_g\int_0^\infty t\, h_n(t)dt + \tau_g^2\int_0^\infty h_n(t)dt\right]^{1/2},$$

$$T_r = \sqrt{2\pi}\left[\int_0^\infty t^2\, h_n(t)dt - \tau_g^2\right]^{1/2}. \qquad (5.27)$$

Figure 5.2 describes a network voltage output response resulting from a unit step input. The normalized network function is expressed as

$$H_n(s) = \int_0^\infty h_n(t)e^{-st}dt \qquad (5.28)$$

Expanding e^{-st} in a power series in (5.28) yields

$$H_n(s) = \int_0^\infty h_n(t)(1 - st + \frac{s^2\, t^2}{2!} - \ldots)dt,$$

$$= \int_0^\infty h_n(t)dt - s\int_0^\infty t\, h_n(t)dt + \frac{s^2}{2!}\int_0^\infty t^2\, h_n(t)dt - \ldots,$$

$$= 1 - s\tau_g + \frac{s^2}{2!}\left(\frac{T_r^2}{2\pi} + \tau_g^2\right) - \ldots \qquad (5.29)$$

52

As shown in Figure 5.3, the microstrip transmission line is described by M identical network sections in cascade each with independent propagation delay
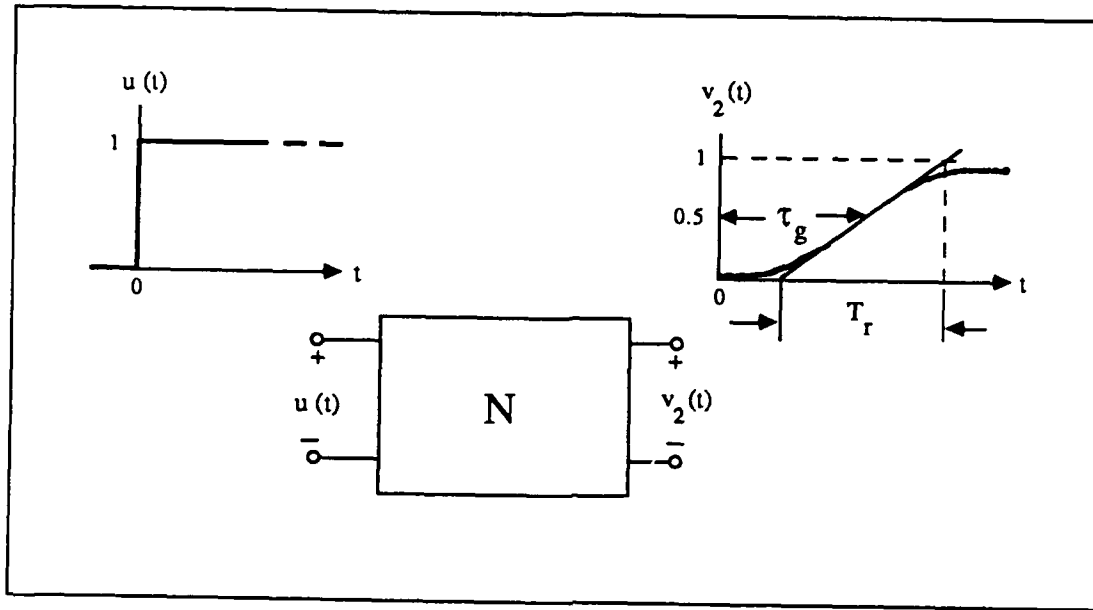
Figure 5.2 A network N with its unit step response

times $\tau_{g_1}, \tau_{g_2}, \ldots, \tau_{g_M}$, and rise times $T_{r_1}, T_{r_2}, \ldots, T_{r_M}$. Then the overall normalized network function is

$$H_n(s) = \prod_{k=1}^{M} H_{nk}(s),$$

$$= \prod_{k=1}^{M} \left[1 - s\tau_g + \frac{s^2}{2!} \left(\frac{T_{rk}^2}{2\pi} + \tau_{gk}^2 \right) - \ldots \right],$$

$$= 1 - s \sum_{k=1}^{M} \tau_{gk} + \frac{s^2}{2!} \left[\left(\frac{T_{rk}^2}{2\pi} + \tau_{gk}^2 \right) + 2 \sum_{k=1}^{M} \sum_{l=k+1}^{M} \tau_{gk}\tau_{gl} \right] \ldots \quad (5.30)$$

Finally,

$$H_n(s) = 1 - s \sum_{k=1}^{M} \tau_{gk} + \frac{s^2}{2!} \left[\sum_{k=1}^{M} \frac{T_{rk}^2}{2\pi} + \left(\sum_{k=1}^{M} \tau_{gk}^2 \right) \right] \cdots \tag{5.31}$$

where the total propagation group delay is

$$\tau_g = \sum_{k=1}^{M} \tau_{gk} \tag{5.32}$$

and the overall rise time for M sections is

$$T_r{}^2 = \sum_{k=1}^{M} T_{rk}^2. \tag{5.33}$$
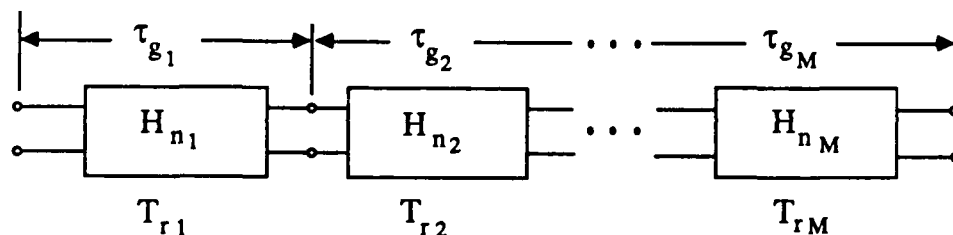
Figure 5.3 Microstrip transmission line as M cascaded networks

Assume that the propagating pulse is the response of some networ⊦ to an unit step. Evidently, the rise time of the previous network(s) is T_{r1}. Now the pulse continues through an unknown network which has a rise time T_r. The resulting pulse then has a total rise time T_{r2}. From (5.33), the expected rise time of the unknown network is given by

$$T_r = \sqrt{T_{r2}^2 - T_{r1}^2}. \tag{5.34}$$

After estimating the network delay and rise times, the ARMA filter coefficients of equation (3.11) are solved from the polynomial coefficients of (5.29), while the first-order AR filter coefficient is also related to τ_g and T_r as follows:

$$a = \exp\left[-\frac{2\,T\,\tau_g}{\left(\dfrac{T_r^2}{2\pi} + \tau_g^2\right)}\right] \tag{5.35}$$

where T denotes the sampling interval.

3. Deterministic Schur Algorithm

The autocorrelation function (ACF) of the normalized impulse response of equation (3.16) is computed as

$$R(\tau) = \int_0^\infty h(t)h(t+\tau)dt, \quad \text{for} \quad \tau = 0,1,2,...,N \tag{5.36}$$

where τ is the correlation lag. However, the sampled autocorrelation function will give a discrete correlation vector as:

$$[R(0), R(1), R(2), \ldots, R(N)] \tag{5.37}$$

Next, the ACF data is applied to the Schur algorithm. The Schur algorithm is a recursive algorithm that solves the AR model parameters (also called the partial reflection coefficients) [Ref. 14]. The algorithm begins by forming a generator matrix (G_0^T) using the sampled autocorrelation vector as

$$G_0^T = \begin{bmatrix} R(0) & R(1) & R(2) & \cdots & R(N) \\ 0 & R(1) & R(2) & \cdots & R(N) \end{bmatrix}. \tag{5.38}$$

Shifting the first column down yields

$$\tilde{G}_1^T = \begin{bmatrix} 0 & R(0) & R(1) & \cdots & R(N-1) \\ 0 & R(1) & R(2) & \cdots & R(N) \end{bmatrix}. \tag{5.39}$$

The 1st-order model reflection coefficient is computed as the ratio of the (2,2) and (2,1) terms of (5.39) as

$$k_1 = \frac{R(1)}{R(0)}. \tag{5.40}$$

A new generator matrix is then formed, given by

$$G_1^T = \Theta(k_1)\tilde{G}_1^T \tag{5.41}$$

where

$$\Theta(k_1) = \frac{1}{\sqrt{1 - k_1^2}} \begin{bmatrix} 1 & -k_1 \\ -k_1 & 1 \end{bmatrix}. \tag{5.42}$$

Similarly, the 2nd-order model reflection coefficient is

$$k_2 = \frac{R(2) - k_1 R(1)}{R(0) - k_1 R(1)}. \tag{5.43}$$

The algorithm repeats until the desired order reflection coefficient is obtained. When the impulse response, h(t), describes a 1st-order AR transfer function, a single reflection coefficient will result. From this reflection coefficient the time constant of the impulse response is easily found. The computational efficiency is achieved by iterating the autocorrelation vector through an Nth-order AR lattice structure. In the next section, the Schur algorithm will be applied to an AR stochastic process.

B. STOCHASTIC PARAMETER ESTIMATION

The following algorithms are presented to estimate the ARMA/AR model parameters when the observable input/output signals are stochastic processes. Assuming a white noise process as the driving input, the system to be identified produces an output process as shown in Figure 5.4. The efficiency of a particular estimation algorithm is governed by the choice of model selected and its order. In practice, we do not usually know *a priori* which model to choose. Once a model, either ARMA or AR, has been chosen, we must specify the model order. In choosing a model for the microstrip transmission line, we will select the ARMA/AR models proposed in Chapter III.

Autoregressive models are the most widely used models because the analysis algorithms for extracting the model parameters are found by solving a set of linear
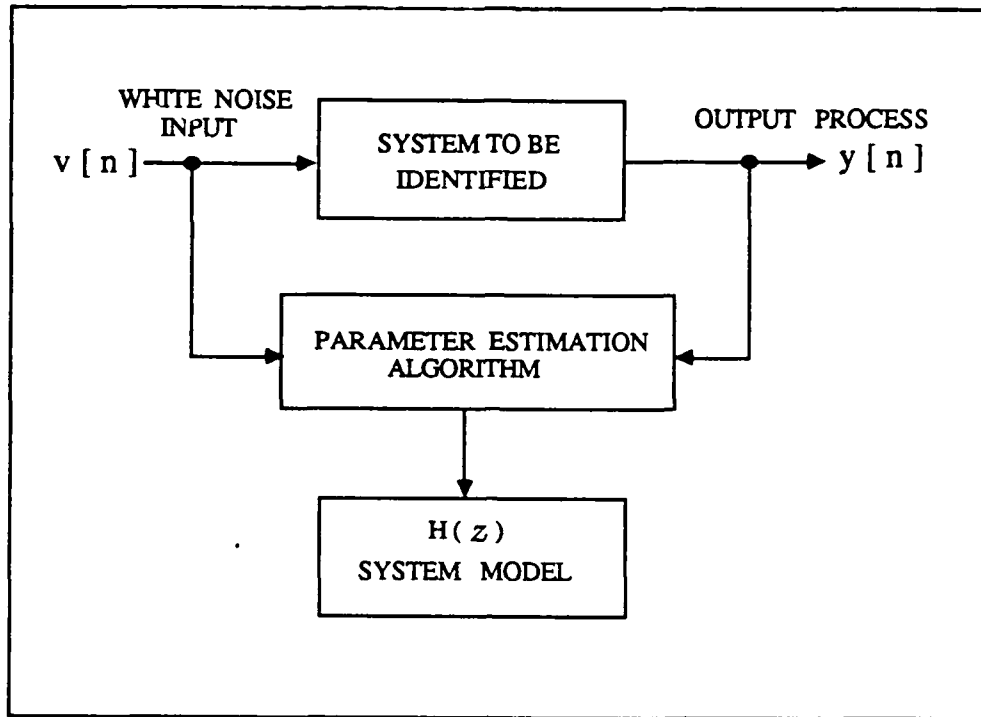
Figure 5.4 Stochastic system identification problem

equations. When the AR modeling assumption is valid, these algorithms provide very good estimates of the model parameters [Ref. 33: p. 131]. Unfortunately, application of these algorithms to non-AR time series data usually results in poor quality estimates. Furthermore, if an AR estimator is applied to a process that is not AR, then the true AR model would be one of infinite order. Any finite order AR model will introduce bias errors from modeling inaccuracies. A trade-off must take place to choose order-p large enough to reduce the bias or to choose order-p small enough to reduce the estimation errors.

In ARMA modeling, the best least squares estimate of the model parameters is, generally, a nonlinear function of the past observations. Nonlinear optimization techniques are usually computationally intensive and may not converge to the

global minimum. Two ARMA parameter estimation algorithms will be presented for stochastic data.

1. Schur Algorithm - Revisited

The AR filter coefficients $(a_1, a_2, a_3, \ldots, a_p)$ are related to the autocorrelation matrix of the data to be modeled and the noise variance (σ^2) by the normal equations:

$$
\begin{bmatrix}
R_{yy}(0) & R_{yy}(-1) & \ldots\ldots & R_{yy}(-n+1) \\
R_{yy}(1) & R_{yy}(0) & \ldots\ldots & R_{yy}(n) \\
\vdots & \vdots & \ddots & \vdots \\
R_{yy}(n-1) & \ldots & R_{yy}(1) & R_{yy}(0)
\end{bmatrix}
\begin{bmatrix}
1 \\
a_1 \\
\vdots \\
a_p
\end{bmatrix}
=
\begin{bmatrix}
\sigma^2 \\
0 \\
\vdots \\
0
\end{bmatrix}. \tag{5.44}
$$

Several algorithms have provided efficient methods for solving the normal equations [Ref. 33: pp. 116-118]. The Levinson algorithm for solving Toeplitz systems of linear equations is well-known in digital signal processing. However, the Levinson algorithm has been discovered to be computationally less efficient than an alternative, the so-called Schur algorithm, because of a requirement to evaluate vector inner products [Ref. 12: pp. 6-22].

We have previously introduced the Schur algorithm for estimating AR model parameters using deterministic signals. Assuming that the unknown system is driven by a white noise process, the AR model parameters can be computed from the output process using the Schur algorithm. The time average approximation of an autocorrelation function (called the sample autocorrelation) is defined as [Ref. 46: p. 27]

$$
\hat{R}_{yy}[n] = \frac{1}{N} \sum_{k=0}^{N-1-k} y[k+n]y[k] \quad \text{for} \quad 0 \le n \le (N-1) \tag{5.45}
$$

where $y[n]$ are the measured output signal samples of length N. A derivation of the Schur algorithm for stochastic signals is presented in Appendix A.

2. Generalized Mullis-Roberts (M-R) Algorithm

An ARMA parameter estimation algorithm based on a generalized Mullis-Roberts criterion has been proposed by Miyanaga et al. [Ref. 47: pp. 619-621].

This algorithm is derived by forming forward and backward prediction models using available input noise and output data. Prediction errors are formed to satisfy specific orthogonality conditions which are similar to those found in AR modeling problems [Ref. 47: pp. 116-121]. Finally, autocorrelation and crosscorrelation functions are calculated and then the forward and backward ARMA filter coefficients are predicted from the correlation lags. A previous reference model is estimated using the M-R algorithm in order to compare parameter estimates obtained by the WLS algorithm. The transfer function of order (4,2), given by (5.24), was driven by a white noise sequence. Table 4 shows the ARMA parameter estimates obtained

Table 4. M-R SIMULATION (4,2) MODEL RESULTS

Parameter	Actual	(WLS) Estimate	(M-R) Estimate
AR:	0.2000	0.2002	0.1933
	-0.6200	-0.6197	-0.6165
	0.1520	0.1529	0.1462
	-0.3016	-0.3014	-0.3010
MA:	1.0000	1.0000	1.0011
	0.2000	0.1998	0.2057
	-0.9900	-0.9902	-0.9893

from the M-R algorithm.

3. A Two-Stage Least Squares Algorithm

When the input noise is unobservable, the M-R algorithm cannot be applied directly. A modified *two-stage* least squares approach is now presented. The name *two-stage* least squares is due to the use of a large order AR least squares estimator followed by another ARMA parameter estimation algorithm. This approach is known to be suboptimal because the noise input is unobservable and must be estimated [Ref. 33: p. 320]. Nevertheless, we modify the *two-stage* least squares algorithm to estimate the specific ARMA model parameters of equation (3.11). The modification uses the M-R algorithm instead of the Levenison algorithm as summarized in Table 6. A reference model was estimated having a transfer function

of

$$H_{ARMA} = \frac{0.1172z^{-1}}{1 - 1.4513z^{-1} + 0.570z^{-2}} \tag{5.46}$$

at a sample period of 1.25 ps. Table 5 lists the results of this algorithm. The M-R algorithm (Step 3) produced very poor MA order coefficient results from the noise estimate. However, the AR order coefficients a_1 and a_2 were used to calculate the

Table 5. TWO-STAGE ALGORITHM RESULTS

Parameter	Actual	Estimated
b_1	0.1172	0.1097
a_1	1.4513	1.4591
a_2	-0.5700	-0.5701

single MA order coefficient with favorable results.

C. MULTI-SECTION MODEL PARAMETER ESTIMATION

In this section new algorithms are presented for the identification of the multi-section microstrip structure. The layer reflection coefficient estimation algorithm will approximate the number and location of cascaded microstrip step discontinuties from the measured reflection data. The *layer-probing* algorithm is an iterative impulse response estimation technique. The algorithm assumes that the multi-section microstrip structure can be described by the lattice AR parametric model of Chapter IV.

1. Layer Reflection Coefficient Estimation Algorithm

A single discontinuity between two lossy transmission lines having different values for the characteristic impedance Z_m, and propagation function γ_m is shown in Figure 5.5. The m-th subscript denotes a single layer defined by equal propagation time delay. Assuming that a current wave $i_m^{(+)'}$ is incident at the discontinuity from the m-th layer, we find that the incident current wave alone cannot satisfy the boundary conditions at the junction [Ref. 35].

60

Table 6. SUMMARY OF TWO-STAGE LEAST SQUARES ALGORITHM

Given the output process, $y[n]$, of length N, the sample interval, T, and $L \gg N$

Step 1: Predict the Lth-order AR parameters $(\hat{a}_k)$

Using the Levinson algorithm [Ref. 33: pp. 213-214] with output, $(y[n])$

Step 2: Estimate the noise input $(\hat{v}[n])$

$$\hat{v}[n] = \sum_{k=0}^{L} \hat{a}_k y[n-k]$$

Step 3: Estimate AR filter coefficients (a_1) and (a_2)

Use the Mullis-Roberts criterion algorithm [Ref. 15]

where $(\hat{v}[n]) \Rightarrow$ input and $(y[n]) \Rightarrow$ output

Step 4: Solve $(\zeta \omega_0 T)$

Substitute (a_2) of Step 3 $\Rightarrow$ (3.11c)

Step 5: Solve $(\omega_0 \sqrt{1 - \zeta^2}\, T)$

Substitute (a_1) from Step 3 $\Rightarrow$ (3.11b)

Substitute $(\zeta \omega_0 T)$ from Step 4 $\Rightarrow$ (3.11b)

Step 6: Solve MA filter coefficient (b_1)

Use $(\zeta \omega_0 T)$ from Step 4, and

$(\omega_0 \sqrt{1 - \zeta^2}\, T)$ from Step 5 to solve ζ

61

Hence, a reflected current wave $i_m^{(-)\prime}$ is generated. Using the boundary conditions at the impedance mismatch, we then write

$$i_m^{(+)\prime} + i_m^{(-)\prime} = i_{m+1}^{(+)} + i_{m+1}^{(-)} \qquad (5.47a)$$

where

$$i_m^{(+)\prime} = i_m^{(+)} \, e^{\gamma_m \, l_m} \qquad (5.47b)$$

$$i_m^{(-)\prime} = i_m^{(-)} \, e^{\gamma_m \, l_m}. \qquad (5.47c)$$
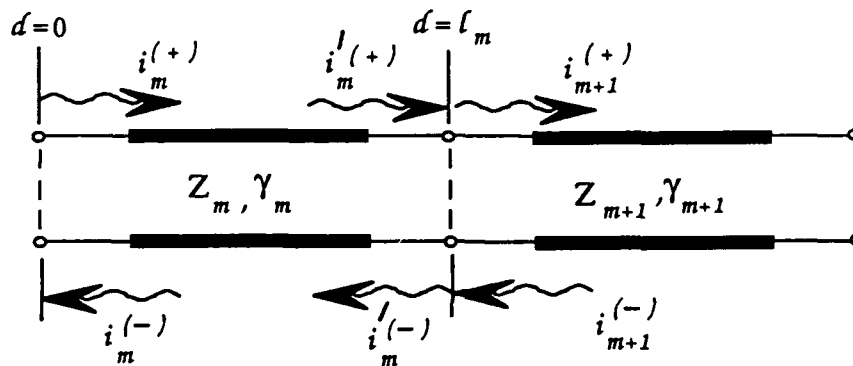
Figure 5.5   Impedance discontinuity equivalent circuit

The voltage and current wave relationships are defined as follows:

$$i_m^{(+)\prime} = \frac{v_m^{(+)\prime}}{Z_m} \qquad (5.48a)$$

$$i_m^{(-)\prime} = -\frac{v_m^{(-)\prime}}{Z_m} \qquad (5.48b)$$

$$i_{m+1}^{(+)} = \frac{v_{m+1}^{(+)}}{Z_{m+1}} \qquad (5.48c)$$

$$i_{m+1}^{(-)} = -\frac{v_{m+1}^{(-)}}{Z_{m+1}}. \qquad (5.48d)$$

62

By substituting (5.48) into (5.47) we have

$$v_m^{(+)\prime} - v_m^{(-)\prime} = \frac{Z_m}{Z_{m+1}} \left(v_{m+1}^{(+)} - v_{m+1}^{(-)} \right). \tag{5.49}$$

The instantaneous voltage at the mismatch is defined as

$$
\begin{aligned}
v(t, l_m) &= v_m^{(+)\prime} - v_m^{(-)\prime} \\
&= v_{m+1}^{(+)} - v_{m+1}^{(-)}.
\end{aligned} \tag{5.50}
$$

Taking (5.49) and (5.50), we solve for the incident voltage wave as

$$v_m^{(+)\prime} = v_{m+1}^{(+)} \left(\frac{1}{\tau_m} \right) + v_{m+1}^{(-)} \left(\frac{\rho_m}{\tau_m} \right) \tag{5.51a}$$

where the reflection coefficient ρ_m, and transmission coefficient τ_m at the mismatch are

$$\rho_m = \frac{Z_{m+1} - Z_m}{Z_{m+1} + Z_m} \tag{5.51b}$$

and

$$
\begin{aligned}
\tau_m &= \frac{2Z_m}{Z_{m+1} + Z_m} \\
\tau_m &= 1 + \rho_m.
\end{aligned} \tag{5.51c}
$$

While the reflected voltage wave at the m-th layer is

$$
\begin{aligned}
v_m^{(-)\prime} &= v_{m+1}^{(+)} \left(\frac{\rho_m}{\tau_m} \right) + v_{m+1}^{(-)} \left(\frac{1}{\tau_m} \right) \\
&= v_m^{(+)\prime} (\rho_m) - v_{m+1}^{(-)} (1 - \rho_m).
\end{aligned} \tag{5.52}
$$

Using (5.51a), the voltage wave incident at the $(m + 1)$-th layer is

$$v_{m+1}^{(+)} = v_m^{(+)\prime} (1 + \rho_m) - v_{m+1}^{(-)} (\rho_m). \tag{5.53}$$

Combining (5.52) and (5.53) into a scattering matrix yields

$$
\begin{bmatrix} v_{m+1}^{(+)} \\ v_m^{(-)\prime} \end{bmatrix} = \begin{bmatrix} 1 + \rho_m & -\rho_m \\ \rho_m & 1 - \rho_m \end{bmatrix} \begin{bmatrix} v_m^{(+)\prime} \\ v_{m+1}^{(-)} \end{bmatrix}. \tag{5.54}
$$

63

Next, we normalize the voltage waves with respect to their characteristic impedance as

$$
\begin{bmatrix} v_m^{(+)\prime} \\ v_m^{(-)\prime} \end{bmatrix} = \frac{1}{\sqrt{Z_m}} \begin{bmatrix} v_m^{(+)\prime} \\ v_m^{(-)\prime} \end{bmatrix}
\tag{5.55a}
$$

and

$$
\begin{bmatrix} v_{m+1}^{(+)} \\ v_{m+1}^{(-)} \end{bmatrix} = \frac{1}{\sqrt{Z_{m+1}}} \begin{bmatrix} v_{m+1}^{(+)} \\ v_{m+1}^{(-)} \end{bmatrix}.
\tag{5.55b}
$$

Using (5.54) and (5.55), the normalized forward recursion matrix yields

$$
\begin{bmatrix} v_{m+1}^{(+)} \\ v_{m+1}^{(-)} \end{bmatrix} = \frac{1}{\sqrt{1-\rho_m^2}} \begin{bmatrix} 1 & -\rho_m \\ -\rho_m & 1 \end{bmatrix} \begin{bmatrix} v_m^{(+)\prime} \\ v_m^{(-)\prime} \end{bmatrix}.
\tag{5.56}
$$

The normalized incident and reflected voltages in (5.56) can be related to the propagation function (γ_m) as

$$
\begin{aligned}
\begin{bmatrix} v_m^{(+)\prime} \\ v_m^{(-)\prime} \end{bmatrix} &= \begin{bmatrix} e^{-\gamma_m\, l_m} & 0 \\ 0 & e^{\gamma_m\, l_m} \end{bmatrix} \begin{bmatrix} v_m^{(+)} \\ v_m^{(-)} \end{bmatrix} \\
&= \begin{bmatrix} e^{-(\alpha_m+j\beta_m)l_m} & 0 \\ 0 & e^{(\alpha_m+j\beta_m)l_m} \end{bmatrix} \begin{bmatrix} v_m^{(+)} \\ v_m^{(-)} \end{bmatrix}.
\end{aligned}
\tag{5.57}
$$

Therefore, (5.56) can be expanded as

$$
\begin{aligned}
\begin{bmatrix} v_{m+1}^{(+)} \\ v_{m+1}^{(-)} \end{bmatrix} &= \frac{1}{\sqrt{1-\rho_m^2}} \begin{bmatrix} 1 & -\rho_m \\ -\rho_m & 1 \end{bmatrix} \begin{bmatrix} e^{-\alpha_m\, l_m} & 0 \\ 0 & e^{\alpha_m\, l_m} \end{bmatrix} \\
&\quad \times \begin{bmatrix} e^{-\beta_m\, l_m} & 0 \\ 0 & e^{\beta_m\, l_m} \end{bmatrix} \begin{bmatrix} v_m^{(+)} \\ v_m^{(-)} \end{bmatrix}.
\end{aligned}
\tag{5.58}
$$

For a lossy dispersive microstrip transmission line the attenuation α_m, and phase β_m terms are functions of frequency.

64

Hence, the total attenuation per m-th layer is described by

$$\alpha_m(f) = \alpha_c(f) + \alpha_d(f) \tag{5.59}$$

where the conductor loss α_c, and the dielectric loss α_d were given by (2.8b) and (2.10), respectively. Whereas, the phase term is related to the frequency-dependent effective microstrip permittivity $\epsilon_{eff}(f)$ as

$$\beta_m(f) = \frac{2\pi f \sqrt{\epsilon_{eff}(f)}}{c}. \tag{5.60}$$

Both the attenuation and phase terms are approximated as constants at the m-th layer. Furthermore, the phase term β_m is proportional to the m-th layer propagation delay time [Ref. 35] as

$$t_m = \frac{l_m}{v_{g_m}}$$
$$= l_m \left(\frac{d\beta_m}{d\omega} \right) \tag{5.61}$$

where v_{g_m} is the group velocity in the m-th layer.

Next we develop the discrete-time recursion equations that solve the inverse scattering problem. Taking the z-transform of the recursion matrix (5.58) and using (5.61) yields

$$\begin{bmatrix} V_{m+1}^{(+)}(z) \\ V_{m+1}^{(-)}(z) \end{bmatrix} = \begin{bmatrix} \Omega(z) \end{bmatrix} \begin{bmatrix} V_m^{(+)}(z) \\ V_m^{(-)}(z) \end{bmatrix} \tag{5.62}$$

where

$$\begin{bmatrix} \Omega(z) \end{bmatrix} = \frac{z^{-1}}{\sqrt{1 - \rho_m^2}} \begin{bmatrix} z^{-1} & -\rho_m \\ -\rho_m z^{-1} & 1 \end{bmatrix} \begin{bmatrix} e^{-\alpha_m l_m} & 0 \\ 0 & e^{\alpha_m l_m} \end{bmatrix}.$$

The variable z^{-1} represents the two-way propagation time delay of the m-th section, while $z^{-\frac{1}{2}}$ represents the one-way time delay. Using (5.58), the $(m+1)$-th layer reflection coefficient is computed by

$$\rho_{m+1} = \frac{v_{m+1}^{(-)}}{v_{m+1}^{(+)}}. \tag{5.63}$$

A layer characteristic impedance profile (in ohms) is determined from the layer reflection coefficient sequence as

$$Z_{m+1} = Z_m \left[\frac{1 + \rho_{m+1}}{1 - \rho_{m+1}} \right] \tag{5.64}$$

where the initial impedance Z_0 is the measured input characteristic impedance. In order to compensate for losses, the algorithm must have prior knowledge of the total attenuation per layer α_m. Unfortunately, this loss information is not available for the inverse scattering problem, but the overall attenuation per structure can be estimated from the measured incident, reflected, and transmitted signals. Under this assumption, we can obtain an average attenuation factor for each layer. A method to estimate the attenuation factor from measured results will be introduced in the last section.

2. Layer-Probing Algorithm

The multi-section microstrip structure is modeled as cascaded linear time-invariant systems. Figure 5.6 describes the first iteration of the *layer-probing* algorithm. The algorithm begins by exciting the structure with an impulsive signal $v_s[n]$. A minimum-phase transfer function $T_1(z)$ is estimated for the first discontinuity using the WLS algorithm. Next, an inverse filter $A_1(z)$ of the transfer function $T_1(z)$ is implemented and excited by the original impulsive signal. The inverse filter output now becomes a new excitation signal. This new input is convolved with the first discontinuity transmission impulse response, resulting in an impulsive signal $v_p[n]$ which probes the second discontinuity. The subsequent reflected wave $v_r[n]$ now contains the reflected impulse response of the second discontinuity. We can ignore that portion of the reflection response caused by the first discontinuity, and record the subsequent data. The recording window is defined by a time greater than the two-way propagation delay time to the first discontinuity. Next, the windowed reflection response is deconvolved across the first discontinuity transmission impulse response in order to observe the second discontinuity reflected impulse response. Similarly, another AR model is estimated from this reflected impulse response, and

then we repeat the procedure. Practically, the excitation signal is bandlimited by the instrumentation, and this prevents the input from being an ideal impulse.
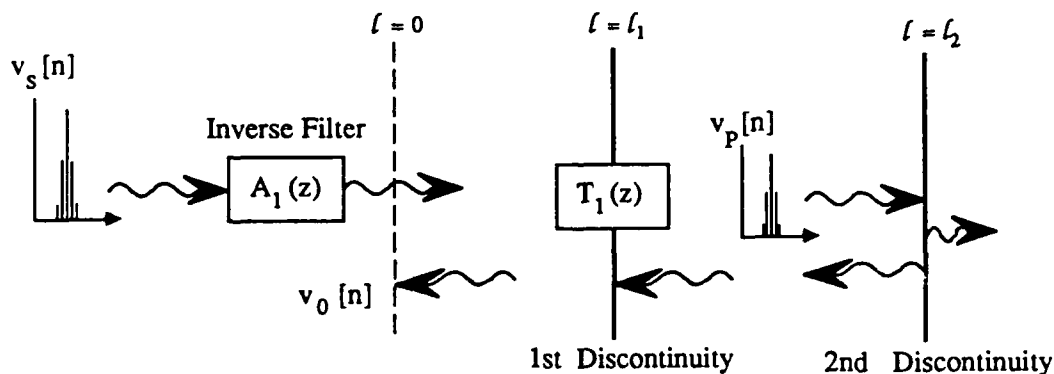
Figure 5.6 Layer-probing of a unknown discontinuity

Also, the microstrip dispersion causes pulse spreading. As a consequence, when two discontinuities are separated by less than the time-dispersive spread for the propagating pulse, multiple reflections may introduce destructive interference. Therefore, when the reflected impulse response is significantly distorted by destructive interference, the inverse scattering problem cannot be solved.

We will attempt to overcome this problem by measuring the output transmission response resulting from the last impulsive probing signal. The remaining unknown discontinuities will be described by an M-th order AR model. A technique is required for estimating an appropriate model order. It is generally observed that $M \ll N$ where N is the data segment length. The best order is typically within the range from N/20 to N/5, but for particularly short data segments the best order can be as large as N/3 or even N/2 [Ref. 48]. Consequently, we do have a priori

knowledge about the order by assuming the model order and the *detected* number of discontinuities are equal. As discussed earlier, the layer reflection coefficient algorithm can estimate the number of discontinuities within the unknown structure.

The transmission response now reveals sufficient transient information to model the remaining unknown sections. Using the WLS algorithm, the transmission impulse response is modeled by an ARMA transfer function $T(z)$. Suppose for simplicity, and not too much loss of generality, that we let the MA model (numerator term) become a gain constant, so that

$$T(z) = \frac{b_0}{A(z)} \tag{5.65}$$

and the transfer function can be rewritten as

$$T(z) = \prod_{r=1}^{M} T_r(z) \tag{5.66}$$

where

$$T_r(z) = \frac{b_0^{1/M}}{1 - a_r \, z^{-1}}$$

and a_r is the AR model parameter. As can be seen, the individual $T_r(z)$ functions are 1st-order AR transfer functions which model each discontinuity. Simulation results are performed in Chapter VI to demonstrate the performance of the *layer-probing* algorithm.

3. Model Attenuation Factor Estimation

The total attenuation factor can be estimated by considering the energy loss of the microstrip structure. An incident transient pulse delivers a finite amount of energy to the microstrip transmission line. Discontinuities in multi-section microstrip structure will introduce multiple energy reflections. We can only measure the reflect 1 and transmitted voltage waveforms with respect to the input/output

measurement ports. Thus, we will treat the lossy multi-section structure as a single cascaded microstrip step discontinuity. Referring to Figure 5.7, the cumulative energy loss is given by

$$E_{LOSS} = E_1^{(i)} - E_2^{(t)} - E_1^{(r)} \qquad (5.67)$$

where

$E_1^{(r)}$ is the cumulative reflected energy measured at the input port (1),

$E_2^{(t)}$ is the cumulative transmitted energy measured at the output port (2), and

$E_1^{(i)}$ is the cumulative incident energy measured at the input port (1).

The cumulative energy values are calculated by [Ref. 31: p. 34]

$$E = \sum_{n=0}^{N} |v[n]|^2 \qquad (5.68)$$

where $v[n]$ is the sampled voltage measured at the respective input/output ports. Next, the energy loss is described in terms of an imaginary discontinuity boundary (D) as

$$E_{LOSS} = \left(E_1^{(i)} - E_D^{(i)}\right) + \left(E_D^{(r)} - E_1^{(r)}\right) + \left(E_D^{(t)} - E_2^{(t)}\right) \qquad (5.69)$$

where

$$E_D^{(i)} = E_1^{(i)} \epsilon^{-2\alpha_1 l_1}$$

$$E_D^{(r)} = E_1^{(r)} \epsilon^{2\alpha_1 l_1}$$

$$E_D^{(t)} = E_1^{(t)} \epsilon^{2\alpha_2 l_2}.$$

Assuming a symmetrical microstrip geometry with respect to the boundary, we will assume $\alpha_1 = \alpha_2$ and $l_1 = l_2$. Equating (5.67) and (5.69) yields the half-symmetrical loss (in nepers) as

$$\alpha_1 l_1 = \frac{1}{4} \left| \ln \left(\frac{E_1^{(r)} + E_2^{(t)}}{E_1^{(i)}} \right) \right|. \qquad (Np) \qquad (5.70)$$

69

The half-symmetrical attenuation factor will be used to design the resistive π-networks in Figure 4.5.
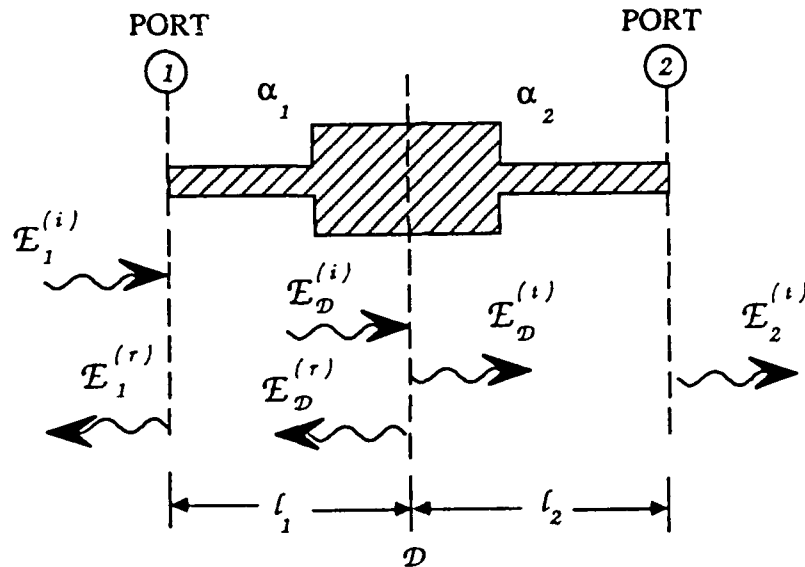
Figure 5.7 Cascaded step energy flow model

This chapter presented the use of several ARMA/AR model parameter estimation algorithms for the characterization and transient response modeling of microstrip transmission lines. Both deterministic and stochastic approaches were discussed. Newly developed algorithms to improve the identification of lossy microstrip lines consisting of multiple discontinuities were also derived. These algorithms were the layer reflection coefficient estimation algorithm, and the *layer-probing* algorithm. The purpose of these algorithms is to estimate the appropriate ARMA/AR model parameters from available time-domain measurements. In Chapter VI, the algorithms' performance will be studied using simulated and experimentally measured data.

VI. EXPERIMENTAL AND SIMULATION RESULTS

The purpose of this chapter is to verify the proposed microstrip models using both experimental and simulation results. The lumped-distributed equivalent circuit and parametric models presented are now simulated for an integrated circuit (IC) interconnection, a cascaded microstrip step discontinuity, and a multi-section microstrip step discontinuity. The microstrip models are verified by comparing picosecond time-domain measurements with transient analysis and parametric model simulation results. Finally, the performance of the ARMA/AR parameter estimation algorithms is studied using simulated and measured data.

A. INTEGRATED CIRCUIT INTERCONNECTION RESULTS

1. Optoelectronic Measurement Techniques

D.H Auston and A.M. Johnson of Bell Laboratories first demonstrated the generation of picosecond pulses on silicon substrates in 1975 by using optically triggered gating [Ref. 49,50]. They used quasimetallic photoconductivity produced by the absorption of short optical pulses in silicon to both turn on and off a switching gap. Figure 6.1 shows an optoelectronic switch using this technique. The microstrip transmission line is fabricated on high resistivity ($\rho = 10^4 \Omega - cm$) silicon and contains a gap which forms the switch. Optical pulses generating mobile carriers within the silicon produce the switching action. The work on silicon has been extended by W.R. Eisenstadt and R.B. Hammond to produce picosecond optoelectronic switches on bulk silicon [Ref. 51]. Their effort was focused towards the production of high speed photoconductors which can be integrated along side other devices on an integrated circuit using standard VLSI fabrication techniques.

The Photoconductor Circuit Element (PCE) is the best laser driven optoelectronic transducer for high-speed sampling applications to integrate on a silicon substrate [Ref. 52]. The primary goal of the PCE is to achieve an ideal impulsive sampling gate.
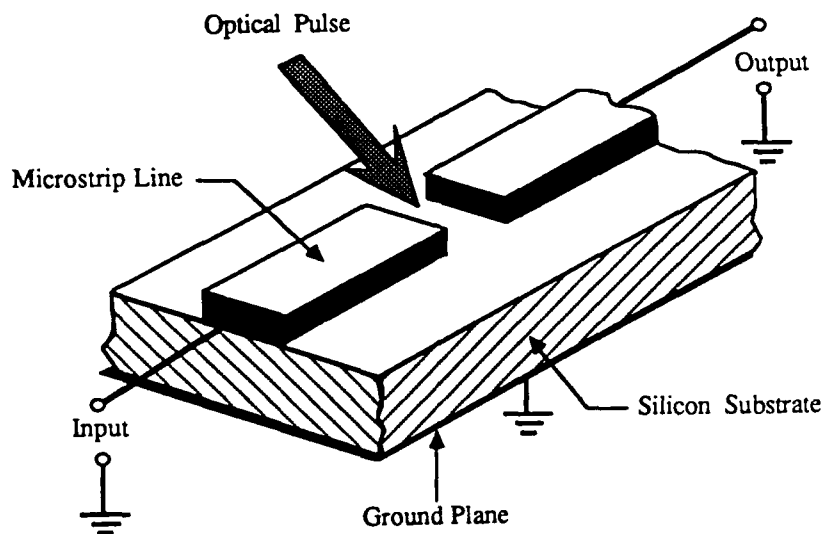
Figure 6.1 Diagram of D.H. Auston's picosecond photoconductor

2. Picosecond Pulse Propagation Measurements

D. Bowman [Ref. 53: pp. 82-94] performed a series of picosecond time-domain measurements using a polysilicon PCE test structure. The structure shown in Figure 6.2 illustrates the IC fabrication of the PCE sampler on the microstrip transmission line. The length of microstrip beyond the last PCE sampler prevents any reflections from the open stub end from returning in time to interfere with the measurement. The experimental sampling system uses a colliding pulse mode-locked (CPM) ring dye laser with a nominal 200 femtosecond optical pulse to excite a 3.5 GHz bandwidth electrical pulse. The half power bandwidth of the electrical

electrical pulse is determined from the magnitude spectrum using the Fast Fourier transform. Table 7 lists the physical properties of the microstrip test structure.
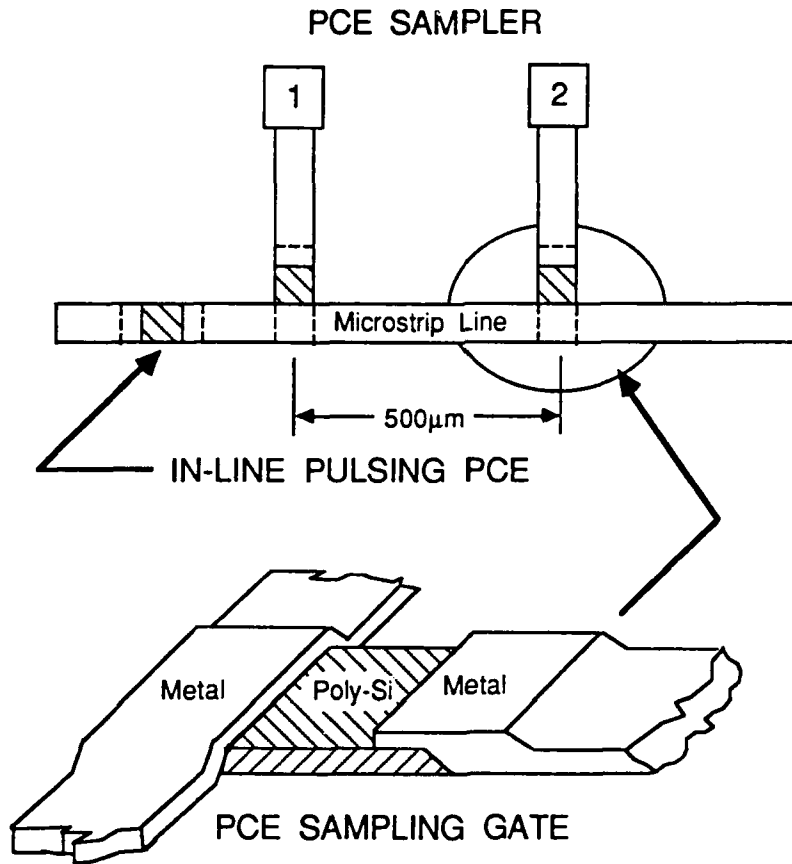
Figure 6.2 Polysilicon PCE microstrip test structure

a. Sampled Waveform Measurements

A transient pulse was measured at different distances along a 100 μm wide microstrip at a sampling interval of 1.25 ps. Figure 6.3 shows the measured waveforms with magnitudes normalized to the peak of the first sampler. Successive curves are the sampled measurements at the second (500 μm), third (1000 μm), and fourth (2000 μm) PCE sampler.

Table 7. IC MICROSTRIP PROPERTIES

Material Properties		Value
Characteristic Impedance	(Z_0)	73.24 Ω
Dielectric Constant	(ϵ_r)	11.7
Substrate Thickness	(h)	350.5 μm
Conductor Thickness	(t)	1.0 μm
Conductor Width	(w)	100.0 μm
Substrate Resistivity (Si)	(ρ_s)	14.5 Ω-cm
Conductor Resistivity (Al)	(ρ_c)	0.262e-05 Ω-cm
Conductor Length	(l)	500 μm
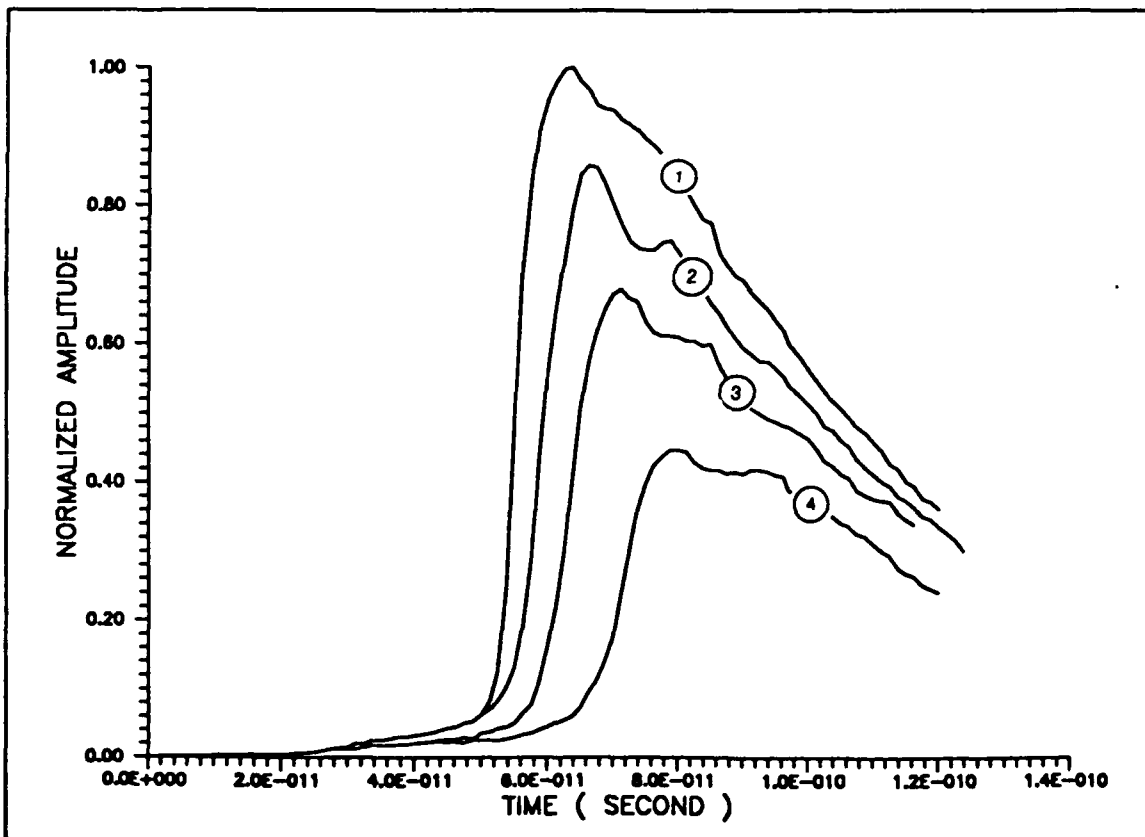
Figure 6.3 High frequency waveform propagation measurements

74

The measured responses show the expected dispersive propagation with high losses. This is evident from the increasing rise times of the pulses (pulse spreading) and smaller peak magnitudes with increasing propagation distance [Ref. 53: pp: 84-85].

b. Propagation Velocity

The rate at which a pulse propagates down an IC interconnection is a very important parameter, particularly for circuits involving critical timing applications or pulse synchronization. At the high frequencies present with picosecond pulses, propagation velocity varies with frequency and affects the shape of the pulse.

The relative time at which the peak magnitude of the pulse occurs can be used to determine the velocity. The group velocity and not the phase velocity of the pulse is actually measured by observing the relative delays of the peak magnitude. Figure 6.4 reports the results of the measured propagation delays at the various time differences between the peak magnitudes for each of the three samplers. The theoretical propagation delay is calculated by [Ref 18: p. 62]

$$t_d = \frac{\sqrt{\epsilon_{eff}}\, l}{c} \tag{6.1}$$

for the different lengths of the microstrip. What is interesting about the results is the almost identical slope for both the measured and theoretical delay. This indicates a relatively constant velocity of $\approx$ 112-114 μm/ps.

c. Propagation Loss

The decrease in the peak magnitude of the propagating pulse with distance seen in Figure 6.3 is evidence of the significant losses present on silicon substrates. Figure 6.5 shows the loss in decibels as a function of propagation distance. The theoretical loss combines the numerical results for conductor loss (2.8b) and dielectric loss (2.10) at three microstrip distances. The measured propagation losses were obtained from relative cumulative energy results. The theoretical values reveal a loss of 2.4 dB/mm while the measurements indicate a 3.6 dB/mm loss is actually occurring. A possible explanation for the discrepancy between the theoretical loss

and the measured loss is that (2.8b) yields a somewhat low result because surface roughness is not considered, and the effective microstrip permittivity value used in (2.10) actually varies with frequency [Ref. 18: p.90].
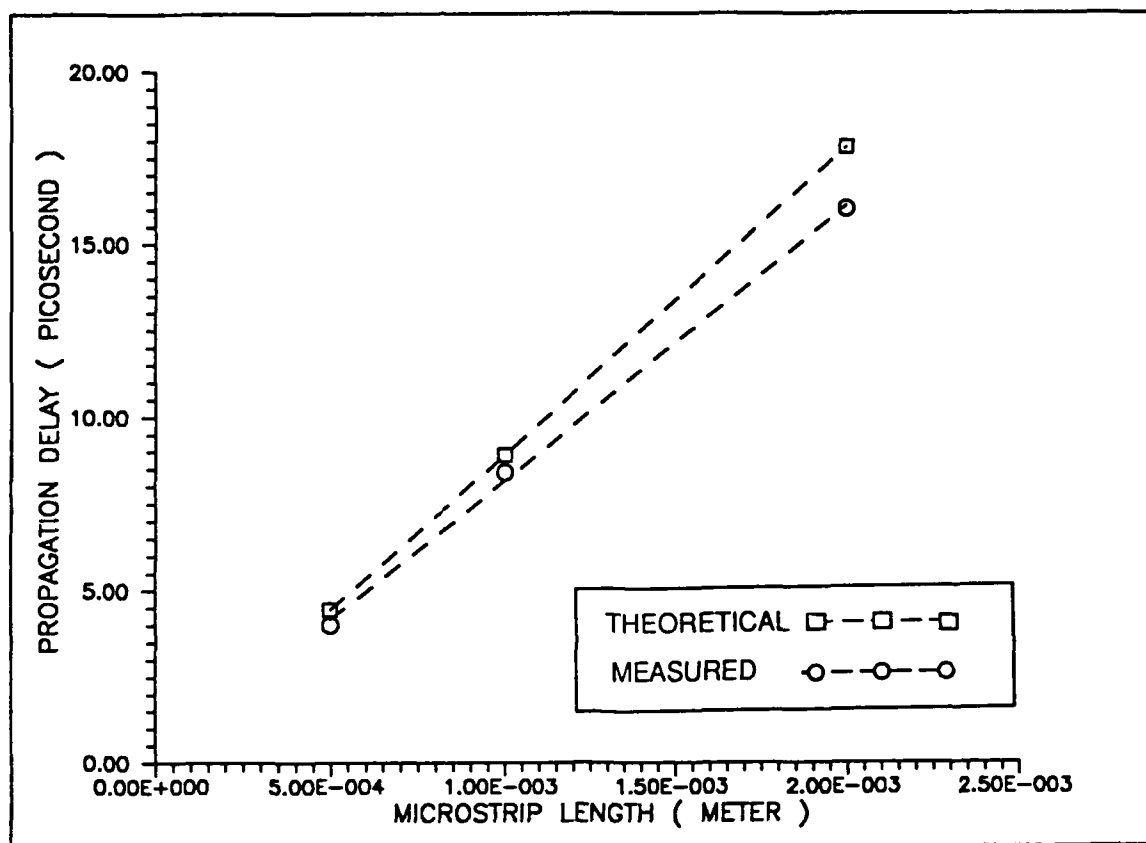
Figure 6.4   Pulse propagation delay on IC interconnection

3. Equivalent Circuit Simulations

The lumped-parameter and lumped-distributed equivalent circuits, derived in Chapter II, are developed for a 500 μm length of microstrip in the PCE test structure. Numerical results for the circuit model are presented in Table 8. Several comments can be made about these theoretical calculations. The static effective microstrip permittivity significantly influences all subsequent calculations. It assumes a TEM mode of propagation on the microstrip which is frequency independent.

76

In the equivalent circuit model the lumped-elements are evaluated at a maximum frequency of 3.5 GHz which corresponds to the bandwidth of the propagating signal.
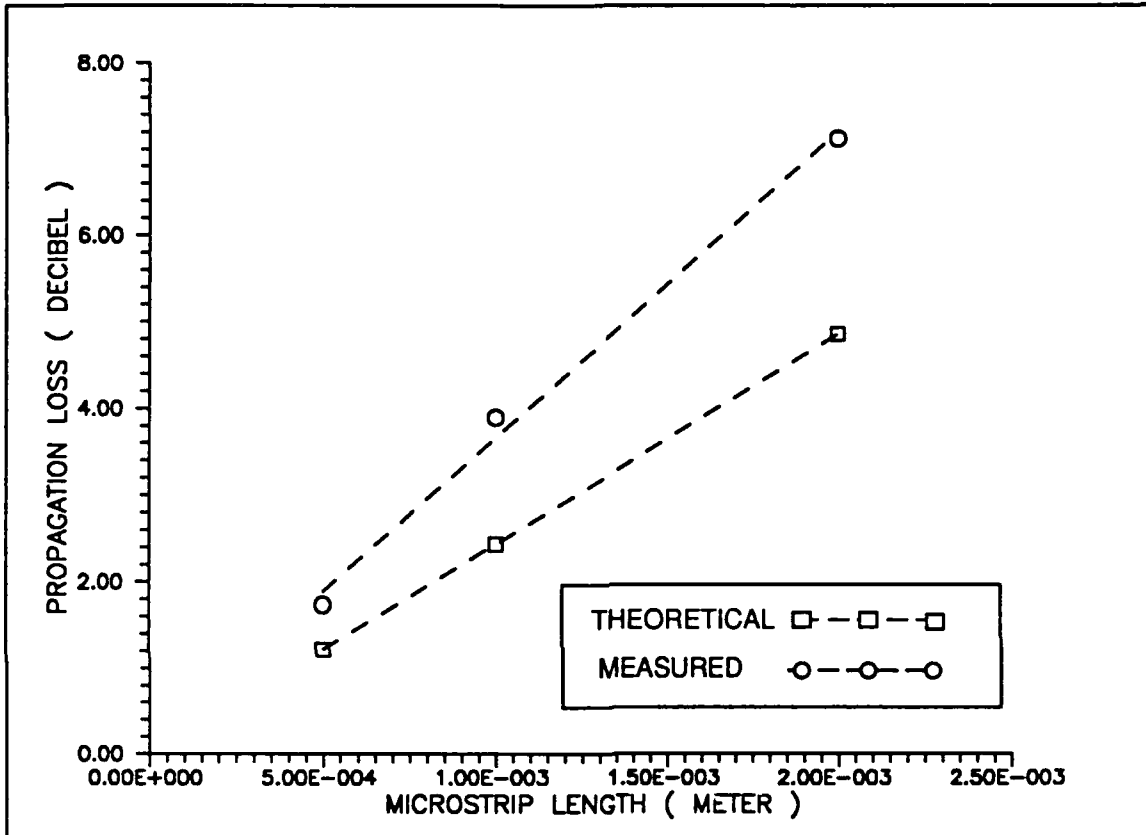
Figure 6.5 Pulse propagation loss on IC interconnection

At this frequency the physical microstrip length should be less than 4 mm ($\approx \lambda_g/8$). Consequently, the equivalent circuit models may lose their accuracy if significant higher order modes are excited by microstrip discontinuities. Figure 6.6 shows

Table 8. EQUIVALENT CIRCUIT THEORETICAL RESULTS

Circuit Parameters		Equation	Value
Maximum Frequency	(f)		3.5 GHz
Static Effective Permittivity	(ϵ_{eff})	(2.2)	7.082
Effective Permittivity	$(\epsilon_{eff}(f))$	(2.6)	7.120
Characteristic Impedance	(Z_0)	(2.3a)	75.22 Ω
Guide Wavelength	(λ_g)	(2.19)	32.12 mm
Shunt Capacitance	(C_π)	(2.18a)	0.03 pF
Series Inductance	(L_π)	(2.18b)	0.33 nH
Propagation Loss			
Conductor Loss	(α_c)	(2.8b)	0.009 dB
Dielectric Loss	(α_d)	(2.10)	1.204 dB
Total Loss	(α_t)		1.213 dB

the schematic diagrams of the equivalent circuit models.
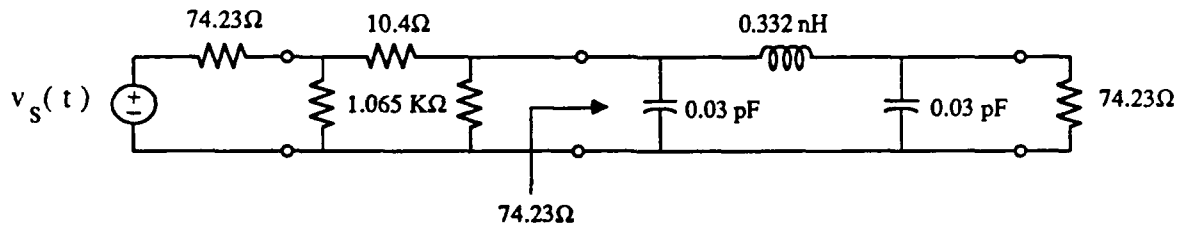
(a)

Figure 6.6 (a) Lumped-element equivalent circuit

In modeling the IC interconnection using equivalent circuits, it is assumed that impedance matching networks are used to prevent reflections. In Figure 6.6(a) a

78

propagation loss of 1.213 dB is modeled by a resistive π-network and a propagation delay of 4.46 ps is described by the reactive LC network. Transient analysis simu-
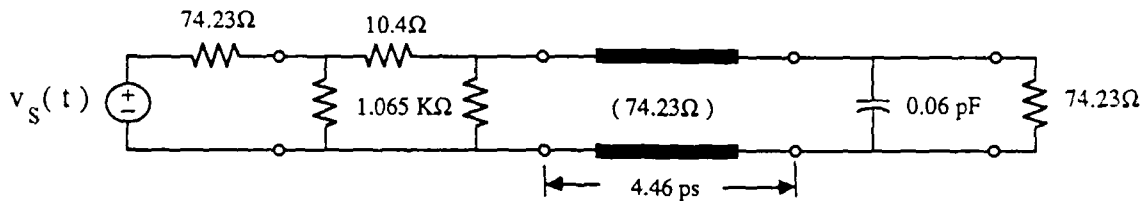
(b)

Figure 6.6(b) Lumped-distributed equivalent circuit

lations of the circuit models are performed using the PSPICE electrical circuit simulation program [Ref. 17]. The PSPICE network listings for both equivalent circuits are given in Appendix B. A piecewise-linear approximation of the normalized reference pulse, measured at the first PCE sampler, acts as the PSPICE voltage source. Waveform comparisons between the second PCE sampler measurement and the circuit model simulations are shown in Figure 6.7. The general shape of the simulations are representative of the measured data; however, there are some significant discrepancies. Two possible causes are suggested. First, on the decaying transient the measurement contains a second peak caused by a reflected signal from the backplane of the substrate. This phenomena is not modeled by the circuit model because of its complex wave nature [Ref. 53: p.90]. Second, the equivalent T-network circuit model simulation indicates a decreased peak magnitude. This observation can be explained as energy lost by a reflected voltage caused by the shunt capacitance.

Next, we derive an equivalent circuit model for the 1000μm length of microstrip. Using the same reactive π-network of Figure 6.6(a), we calculate the new shunt capacitances and series inductance as 0.06 pF and 0.663 nH, respectively. The
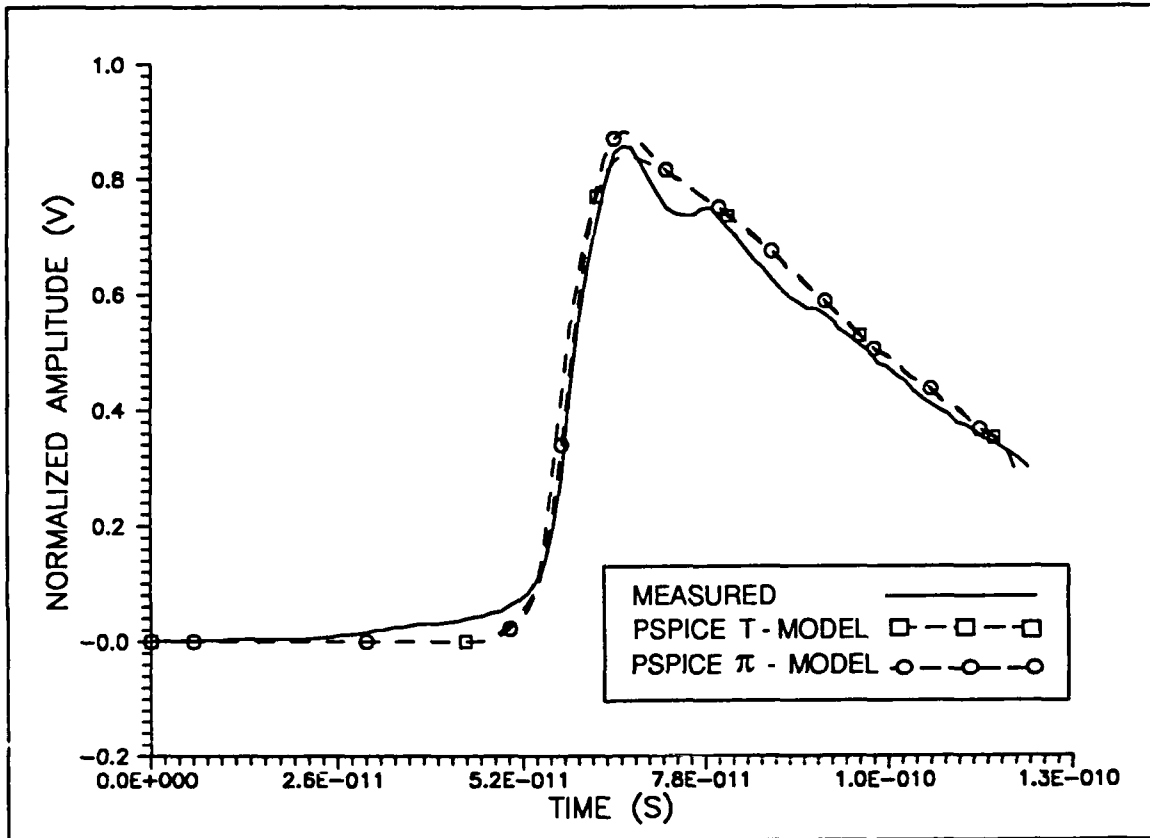
Figure 6.7 Waveform simulations of the equivalent circuit models

measured propagation loss of 3.891 dB is used to evaluate the resistive π-network. Figure 6.8(a) compares the PSPICE transient analysis simulation with the measured response. The simulated results tend to underestimate the rise time of the measured pulse.

This error may be attributed to the breakdown in the lumped-element equivalent circuit assumption as the physical length of the microstrip increases. Therefore, we can improve the model by cascading two reactive π-network sections. A PSPICE simulation was performed using the higher order circuit model.
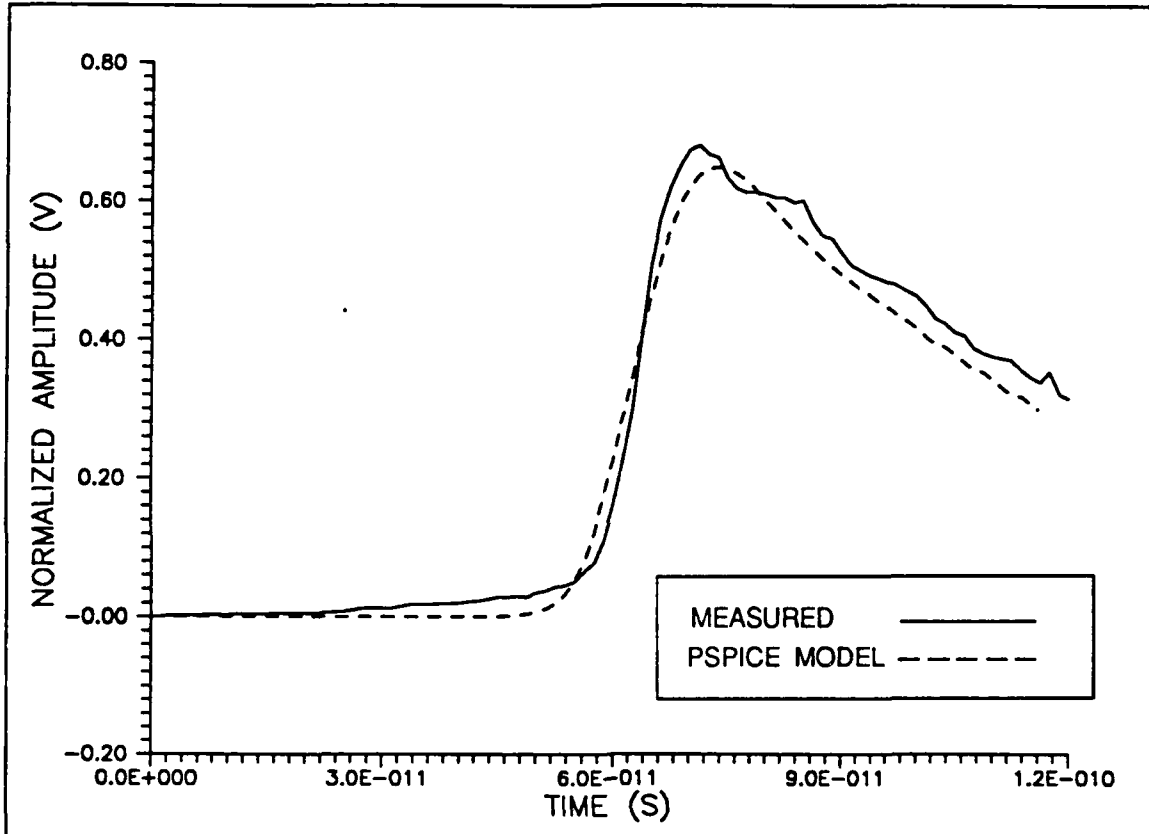
Figure 6.8(a) Single LC network simulation at the 1000μm PCE sampler

Figure 6.8(b) shows a significant improvement in the waveform agreement, especially in the rise times. However, as the number of reactive lumped-elements increase, the model order also increases.

Then the mathematical relationships among the model parameters and the microstrip physical properties will become more complex.
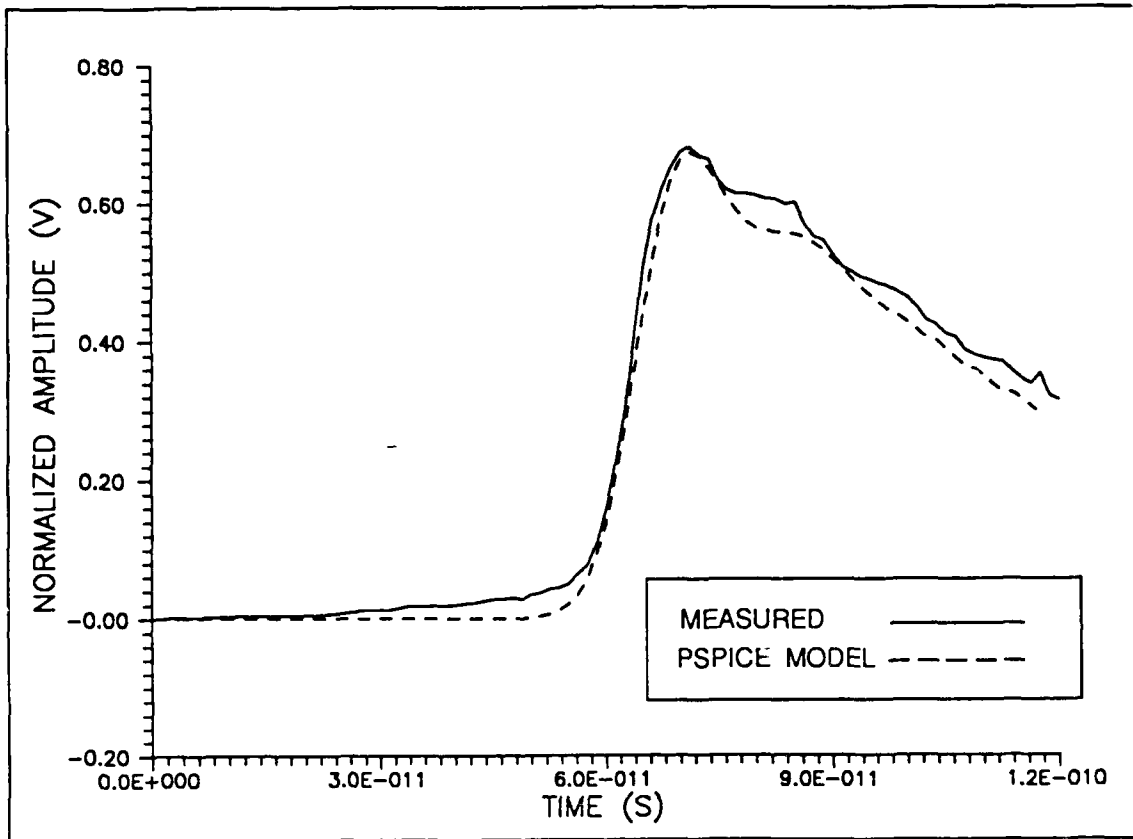
Figure 6.8(b) Cascaded LC network simulation at the 1000μm PCE sampler

4. Parametric Model Simulations

The following ARMA digital transfer function is computed for the 500 μm microstrip test section using (3.10) and (3.11) at a sampling interval of 1.25 ps:

$$H_{ARMA}(z) = \frac{0.1172 \, z^{-1}}{1 - 1.4513 \, z^{-1} + 0.57 \, z^{-2}}. \tag{6.2}$$

The normalized reference pulse, measured at the first PCE sampler, is attenuated by 1.213 dB and then iterated through a difference equation of (6.2). Similarly, an AR digital transfer function is evaluated using (3.19) as

$$H_{AR}(z) = \frac{0.4295}{1 - 0.5705 \, z^{-1}}. \tag{6.3}$$

The normalized reference pulse is again attenuated by 1.213 dB and iterated through a difference equation of (6.3). Figure 6.9 shows the ARMA and AR model simulation results as compared with the measured pulse.
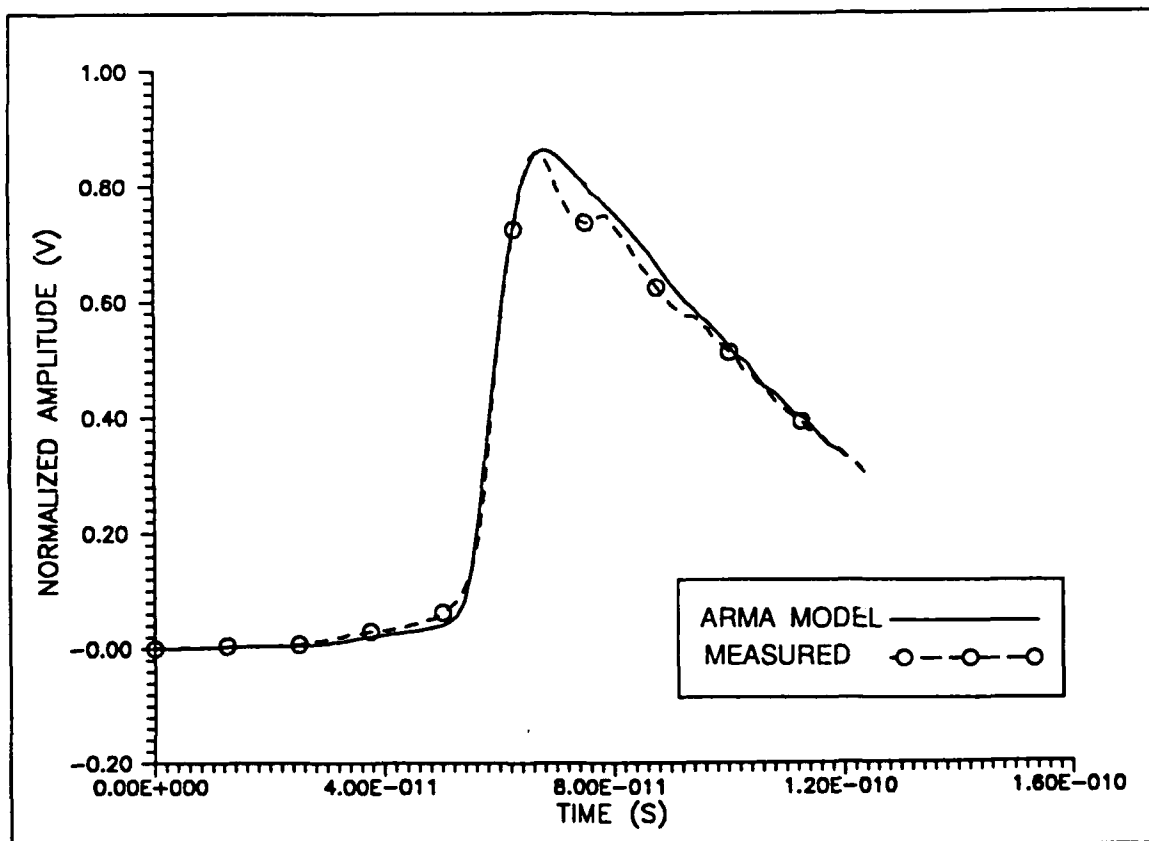
Figure 6.9(a) 1st-order ARMA parametric model simulation

83

Simulated pulses are shown by solid lines while the measurements are indicated with dash lines. Both simulated waveforms have properly accounted for the loss mechanisms on the 500μm microstrip section; however, the 2nd-order ARMA model result shows an outstanding waveform agreement as compared with the 1st-order AR model. In the next section we will focus on the model parameter estimation algorithms using both simulated and measured data.
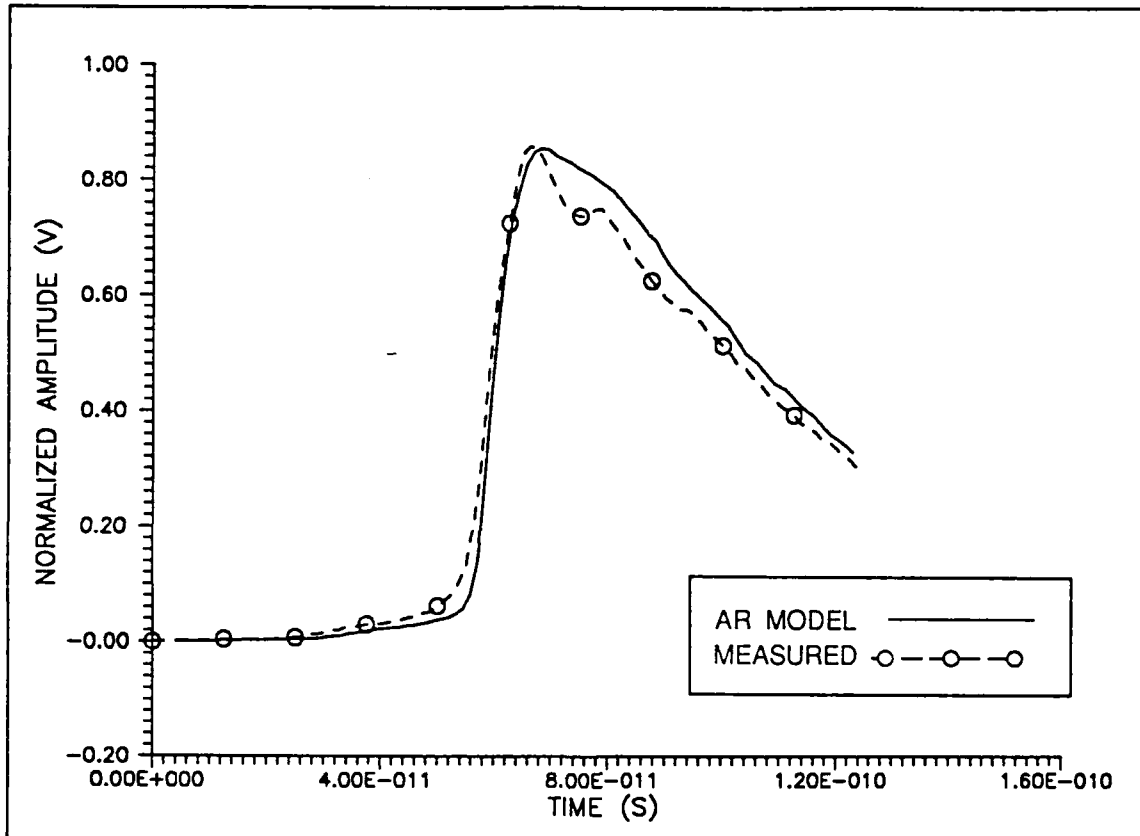
Figure 6.9(b) 1st-order AR parametric model simulation

5. Model Parameter Estimation Results

a. WLS Algorithm

The weighted least squares (WLS) algorithm of Chapter V can be used to estimate model parameters from a given sample impulse response. First, we must obtain an accurate impulse response from the available input/output measurements. The impulse response was obtained by deconvolving the output data, measured at

84

the second PCE sampler, with the measured normalized input data. The original measured data, sampled at 1.25 ps, was decimated to a sampling interval of 5 ps to improve the frequency resolution of the FFT during deconvolution. Next, the resulting sample impulse response was applied to the WLS algorithm. The estimated ARMA model parameters are listed in Table 9. Figure 6.10 compares the

Table 9. ARMA PARAMETERS USING WLS ALGORITHM

Parameter	Theoretical	Estimated
b_1	0.657	0.688
a_1	0.285	0.187
a_2	-0.106	-0.107

estimated impulse response to the measured and theoretical impulse responses at a 5 ps sampling interval.
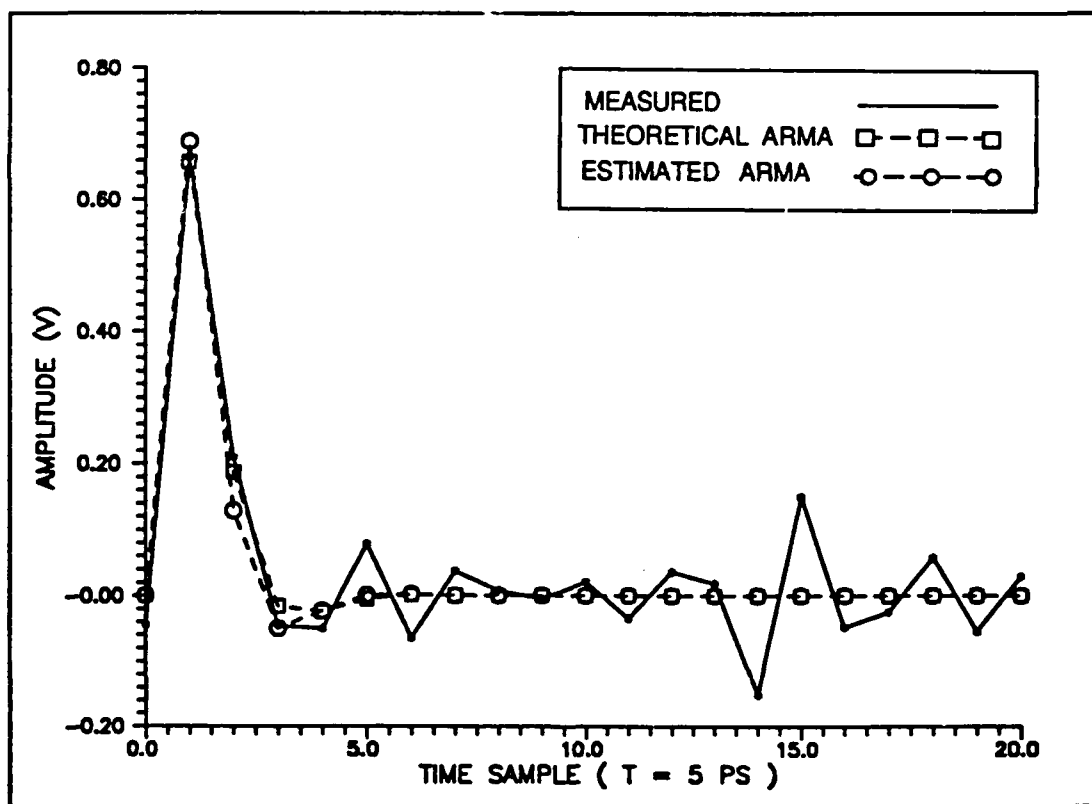
Figure 6.10 Comparison of ARMA model sample impulse responses

85

b. Stochastic Methods

ARMA and AR sample impulse responses were simulated using a PSPICE transient analysis of the equivalent circuit models at a sampling interval of 1.25 ps. Stochastic output processes are generated using the convolution summation

$$y[n] = \sum_{k=0}^{N} v[k]h[n-k] \tag{6.4}$$

where $v[n]$ is an input Gaussian white noise sequence and $h[n]$ is the simulated sample impulse response. The white noise sequence was obtained using a pseudo-random number generator program. The output process $y[n]$, having a record length of 1800 samples, and the original white noise sequence were applied to the M-R algorithm. The ARMA digital filter coefficients were estimated for a (2,1) order model. Table 10 compares these estimates to the theoretical parameter values at a 1.25 ps sampling interval.

Table 10. ARMA PARAMETERS USING M-R ALGORITHM

Parameter	Theoretical	Estimated
b_1	0.1172	0.1137
a_1	1.4513	1.4796
a_2	-0.5705	-0.5905

The estimated results compare favorably with the theoretical model parameter values. There is, however, a limitation in using the stochastic approach. First, the M-R algorithm requires input/output data to be simultaneously sampled to provide accurate ARMA parameter estimates. Second, microwave measurement techniques are usually based on frequency-domain scattering parameters, and high-speed picosecond sampling techniques are not commercially available.

The Schur algorithm is used to estimate a 1st-order AR model. Initially, a 1st-order AR sample impulse response was simulated using PSPICE at a sampling interval of 1.25 ps. Using equation (5.45), a sample autocorrelation sequence is

computed from the impulse response data. Then the Schur algorithm is used to solve the AR reflection coefficients, and the normalized AR transfer function yields

$$H_{AR}(z) = \frac{1}{1 - 0.57z^{-1}} \cdot \qquad (6.5)$$

Since the impulse response was simulated using a 1st-order AR model a single Schur reflection coefficient should be expected.

c. Elmore Method

Network functions are now estimated from rise and delay time measurements. Figure 6.11 describes two consecutive PCE sampler voltage measurements denoted as $v_2(t)$ and $v_3(t)$. A two-port network describes the 500μm length of microstrip.
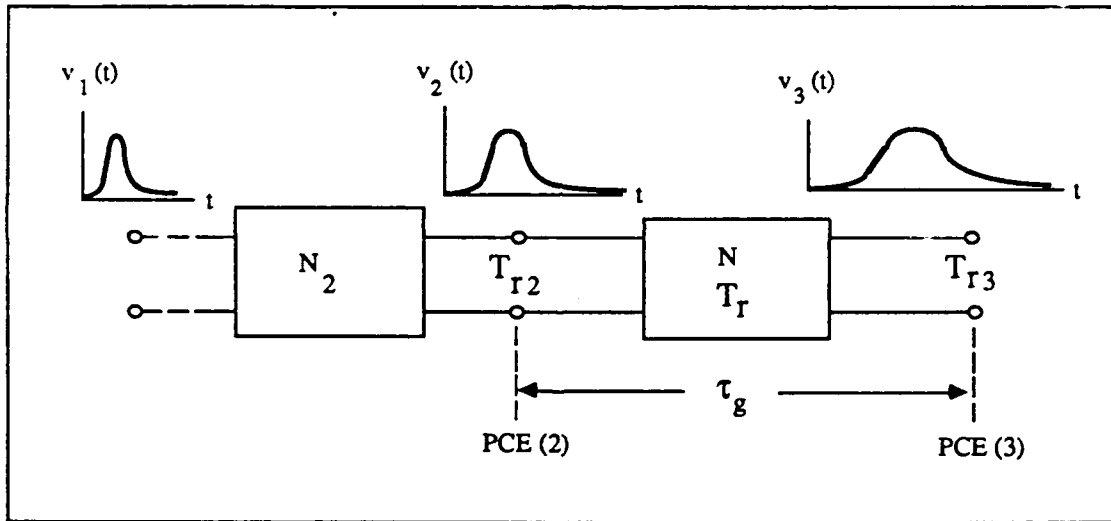
Figure 6.11 Cascaded network functions

The Elmore rise time (T_r) is defined as the reciprocal of the slope of the tangent drawn to the response curve at its half-magnitude point [Ref. 46]. The delay times are estimated at consecutive peak or half-magnitude points. Referring to Figure 6.12, a delay time of 4.41 ps is obtained by averaging the peak magnitude delay (4.48 ps) and the half-magnitude (4.33 ps) delay times. A rise time of 2.06 ps is computed using (5.34) for $T_{r2} = 7.73$ ps and $T_{r3} = 8.00$ ps.

A 2nd-order network function is evaluated as

$$H(s) = \frac{99.3836 \times 10^{21}}{s^2 + 438.282 \times 10^9 s + 99.3836 \times 10^{21}}.$$

(6.6)

The characteristic impedance of the microstrip must be determined prior to solving for ω_0 and ζ in (3.5). The estimation of the characteristic impedance will be addressed in the next section. Finally, the ARMA model parameters are calculated at the sampling interval of 5 ps using equations (3.10) and (3.11).
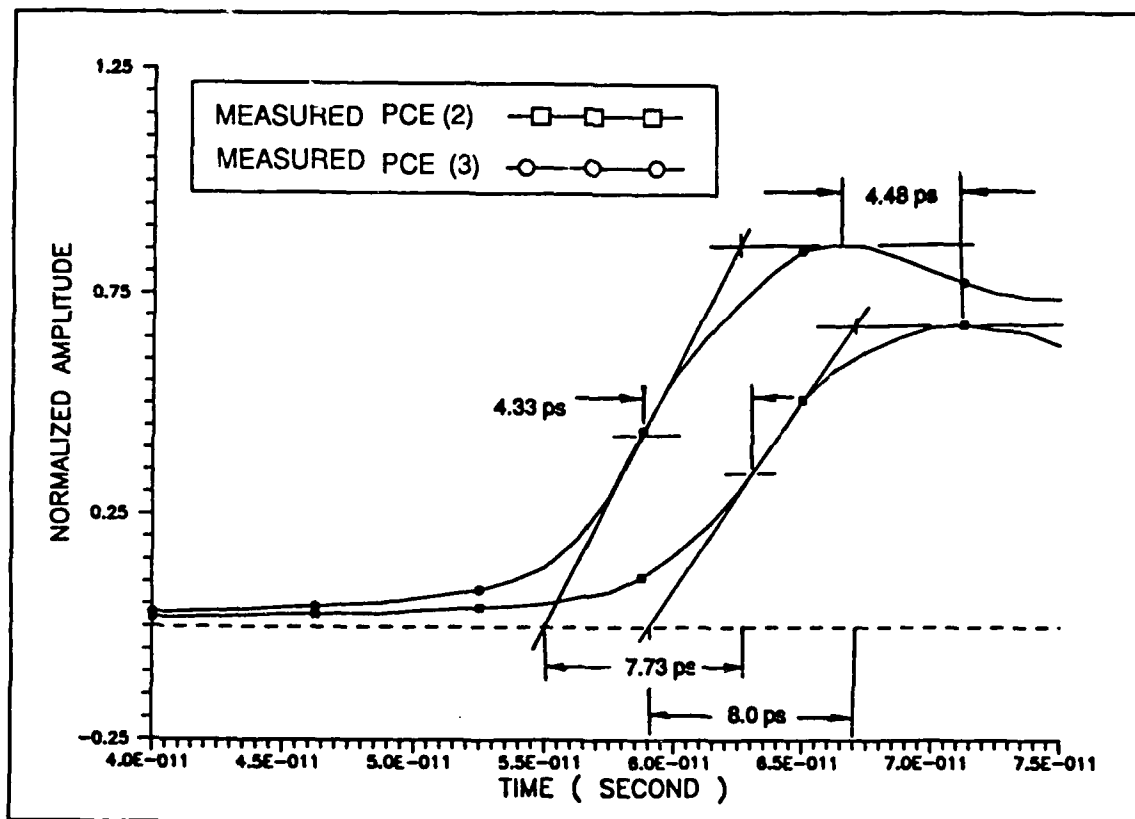
Figure 6.12 Elmore delay and rise time graphical estimates

Equation (5.35) solves the 1st-order AR filter coefficient in terms of the delay and rise times. Both the estimated and theoretical ARMA/AR model parameters are compared in Table 11 at a 1.25 ps sampling interval.

88

The Elmore estimates for the AR model parameters, including the denominator AR filter coefficients of the ARMA model, all show a slight increase over their theoretical

Table 11. MODEL PARAMETERS USING ELMORE

ARMA Parameter	Theoretical	Estimated
b_1	0.1172	0.1165
a_1	1.4513	1.4602
a_2	-0.5705	-0.5782
AR Parameter		
a	0.5705	0.5782

values. This result will explain the increase in effective microstrip permittivity estimates presented in the next section.

d. Estimation of Physical Microstrip Properties

The characteristic impedance at each PCE sampler is computed using (2.29) and (2.30). Table 12 lists the calculated characteristic impedance estimated at each PCE sampler. The average impedance of 74.32 Ω compares very favorably to the actual microstrip characteristic impedance of 74.23 Ω.

Table 12. CHARACTERSITIC IMPEDANCE ESTIMATES

PCE Sampler No.	Z_0
(1)	72.92 Ω
(2)	73.03 Ω
(3)	77.06 Ω
Average Value	74.34 Ω

The effective microstrip permittivity (ϵ_{eff}) is directly calculated from the model parameter estimates using (3.22) and (3.25). Several theoretical expressions have been cited in the literature for the effective microstrip permittivity. Here, we have computed a value of 7.082 using equation (2.2). However, other closed-form expressions will produce different results. For example, another expression for the

89

effective microstrip permittivity, given the characteristic impedance, is [Ref. 18: p.44]

$$\epsilon_{eff} = \frac{\epsilon_r + 1}{2}\left[1 + \frac{29.98}{Z_0}\left(\frac{2}{\epsilon_r + 1}\right)^{\frac{1}{2}}\left(\frac{\epsilon_r - 1}{\epsilon_r + 1}\right)\left(\ln\frac{\pi}{2} + \frac{1}{\epsilon_r}\ln\frac{4}{\pi}\right)\right]^2 \quad (6.7)$$

$$\epsilon_{eff} = 7.186$$

where $Z_0 = 74.23\ \Omega$ and $\epsilon_r = 11.7$ for silicon substrate. Table 13 lists the effective microstrip permittivity values that were computed using the ARMA/AR model parameters obtained from the different estimation algorithms.

Table 13. EFFECTIVE PERMITTIVITY ESTIMATES

Estimator	ARMA	AR
WLS	7.210	
Schur		7.087
Elmore	7.511	7.496

These results indicate that the best model parameter estimators are the WLS and Schur algorithms. These algorithms provide optimal estimates in a least squares sense, while the Elmore method was extremely dependent upon obtaining accurate rise and delay time measurements. Precautions should be made whenever we compare the estimated results to the theoretical values. For example, the accuracy of the theoretical expressions is dependent upon the shape ratio w/h range. In all cases the shape ratio will be accurate to ± 1 percent. For narrow lines ($w/h < 1.3$), the effective microstrip permittivity has an error range $+0.5$-0.0 percent. When calculated using (6.7), ϵ_{eff} is accurate to ± 1 percent [Ref. 18: pp. 45-46]. Additionally, the effective microstrip permittivity is in fact frequency dependent, and the values tend to be slightly higher than those given by (2.2) and (6.7).

B. CASCADED MICROSTRIP STEP DISCONTINUITY RESULTS

The equivalent circuit and parametric models of Chapter IV are validated by comparing model simulations with experimental measurements. Figure 6.13 describes a cascaded microstrip step discontinuity structure that was fabricated on G-10 epoxy dielectric material. The physical dimensions of the cascaded step discontinuity were restricted by the available photolithographic equipment and the dielectric substrate. A half power bandwidth of 400 MHz for the measured reference pulse was selected as the maximum design frequency. This frequency is used in the theoretical calculations. Table 14 summarizes the theoretical microstrip results obtained from the closed-form expressions.
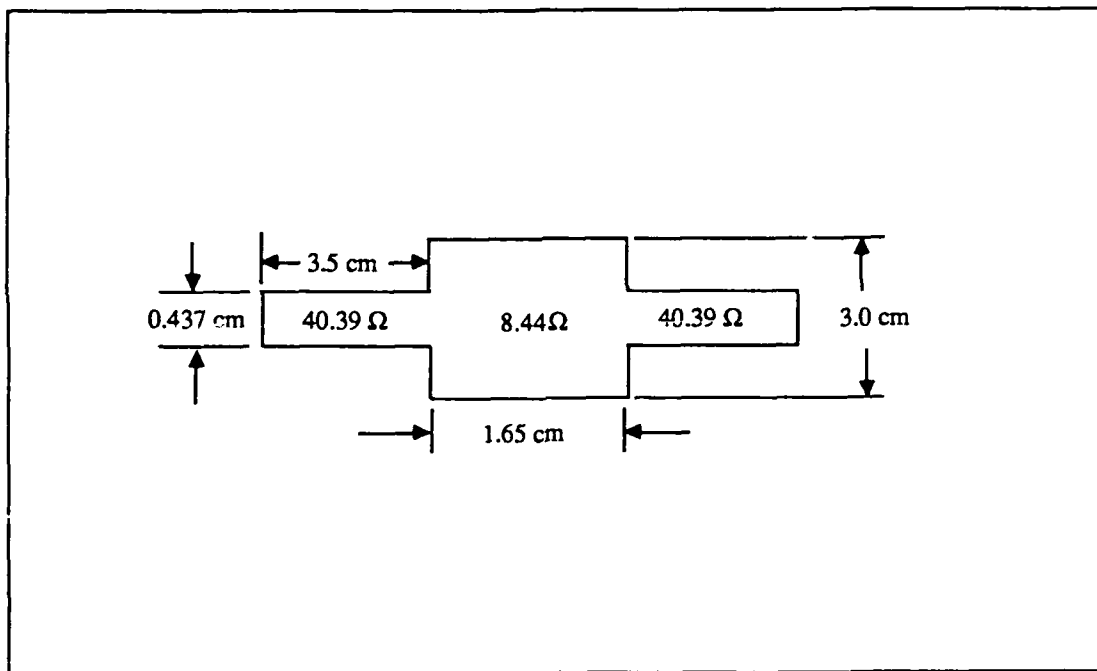
Figure 6.13 Cascaded microstrip step discontinuity

1. Validation of Equivalent Circuit Models

The lumped-element values in Table 14 are associated with the equivalent circuit models of Figures 4.3(c) and 4.4(b). A transient analysis simulation, using PSPICE, is performed for each equivalent circuit. A piecewise-linear approximation

of the measured input pulse was used in the transient analysis simulations. A half-symmetric attenuation factor of 0.0348 nepers is computed from the measured incident, reflected, and transmitted cumulative energy. Separate resistive attenuator π-networks are designed to model each half-symmetric loss. The shunt resistors (2.316 kΩ) are given by [Ref. 37: pp.186-192]:

$$R_1 = Z_0 \left(\frac{N+1}{N-1} \right) \qquad (6.8a)$$

and the series resistor (1.41 Ω) by

$$R_2 = Z_0 \left(\frac{N^2 - 1}{2N} \right) \qquad (6.8b)$$

where the loss in decibels is $20 \log_{10} N$. Transmission and reflection output responses are simulated. These simulations are compared to the measured responses in Figures 6.14(a) and 6.14(b), respectively. The measured transmission
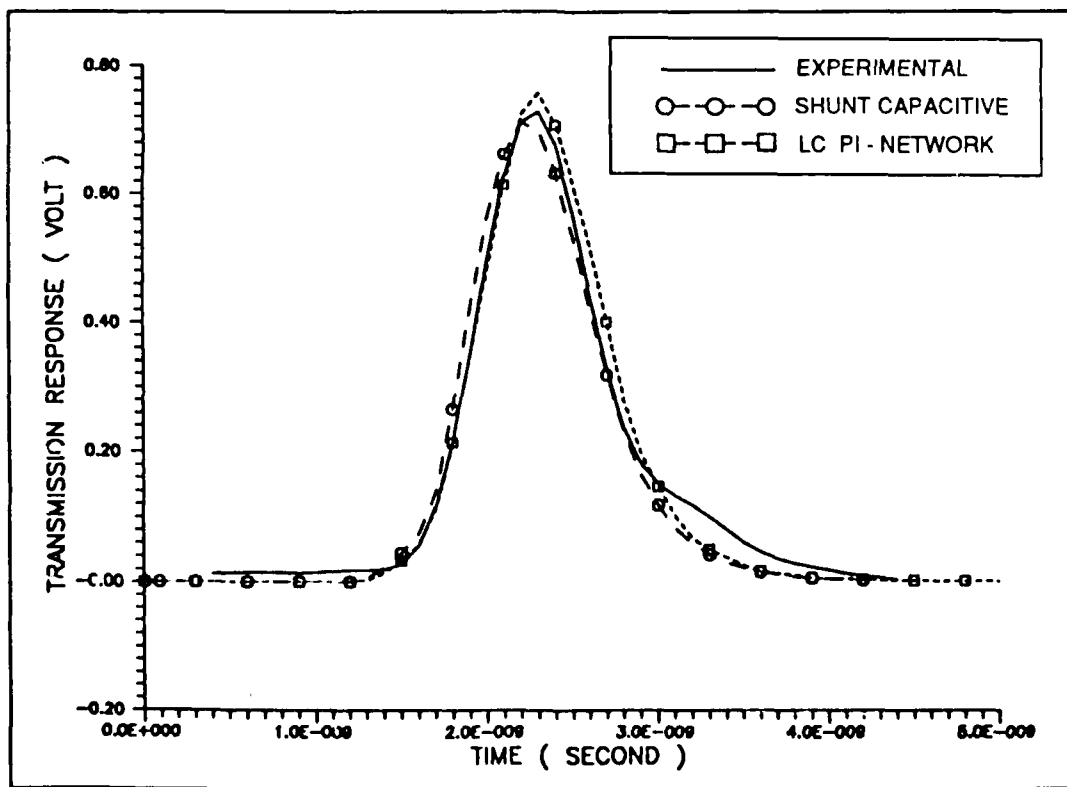
Figure 6.14(a)   PSPICE simulated transmission response

and reflection responses were obtained using the inverse FFT of the measured scattering parameters.

2. Parametric Model Simulations

Using equations (4.14), and (4.16) − (4.18), yields a 3rd-order ARMA transfer function

$$T_3(z) = \frac{6.776 \times 10^9 - 7.295 \times 10^9 z^{-1} + 4.323 \times 10^9 z^{-2}}{1 - 1.702 z^{-1} + 1.5964 z^{-2} - 0.762 z^{-3}} \qquad (6.9)$$

at a sampling interval of 40 ps. A sample impulse response is generated using the difference equation of (6.9). The sampled incident pulse is then convolved with the sample impulse response data to produce an output transmission response.

Table 14. CASCADED STEP THEORETICAL RESULTS

Microstrip Parameter		Equation	Value
Wide Width (3 cm) Segment			
Static Effective Permittivity	(ϵ_{eff})	(2.2)	3.953
Effective Permittivity	$(\epsilon_{eff}(f))$	(2.6a)	4.024
Characteristic Impedance	(Z_{01})	(2.3a)	8.44 Ω
Guide Wavelength	(λ_{g01})	(2.19)	373.90 mm
Shunt Capacitance	(C_S)	(4.7)	13.10 pF
End Inductance	(L_e)	(4.8)	0.931 nH
Narrow Width (0.437 cm) Segment			
Static Effective Permittivity	(ϵ_{eff})	(2.2)	3.354
Effective Permittivity	$(\epsilon_{eff}(f))$	(2.6a)	3.360
Characteristic Impedance	(Z_{02})	(2.3b)	40.39 Ω
Guide Wavelength	(λ_{g02})	(2.19)	409.16 mm
Series Inductance	(L_s)	(4.5)	8.640 nH
Step Discontinuity Circuit Parameters			
Shunt Capacitance	(C_d)	(4.3a)	0.559 pF
Series Inductance	(L_1)	(4.1a)	0.054 nH
Series Inductance	(L_2)	(4.1b)	0.235 nH

93

The normalized transmission response is compared to the measured output in Figure 6.15. Next, the 1st-order ARMA reflection and transmission transfer functions are
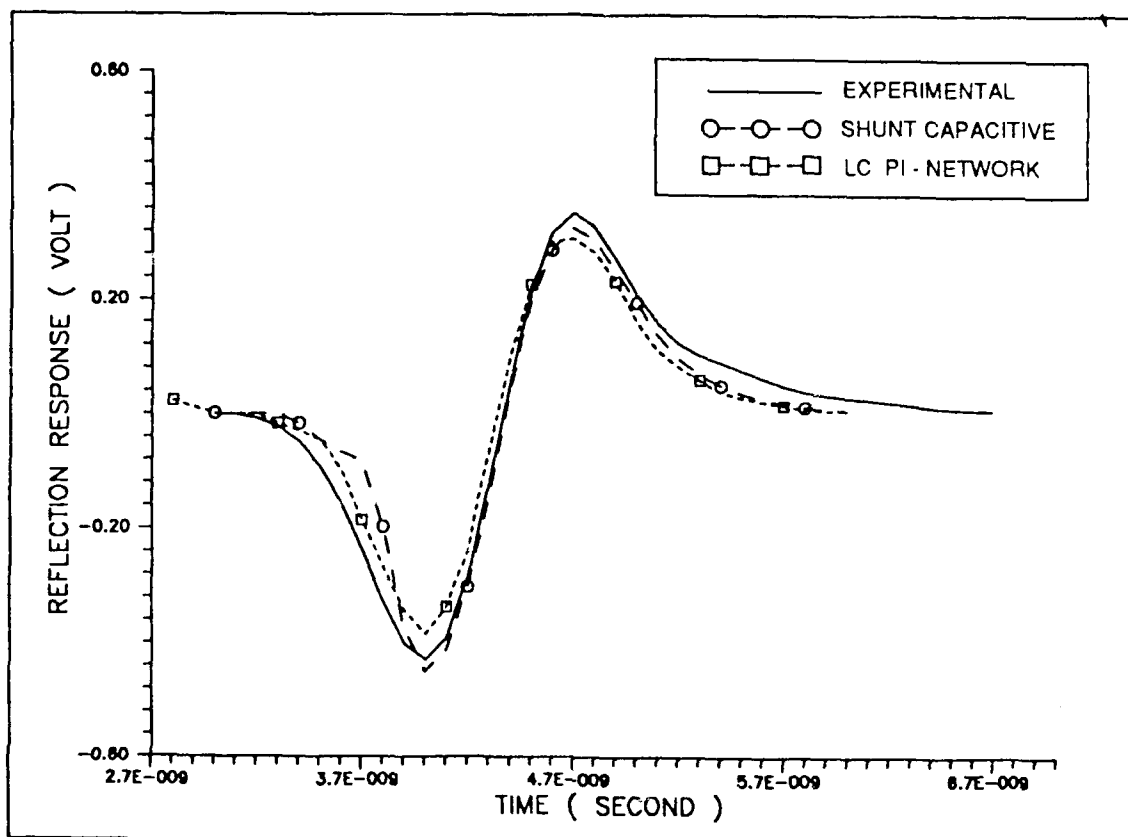
Figure 6.14(b)   PSPICE simulated reflection response

obtained using (4.20b) and (4.20c), respectively, as

$$\Gamma_1(z) = \frac{0.746\left(z^{-1} - 1\right)}{1 - 0.492z^{-1}} \tag{6.10a}$$

and

$$T_1(z) = \frac{0.254\left(1 + z^{-1}\right)}{1 - 0.492z^{-1}} \tag{6.10b}$$

at a sampling interval of 200 ps.

Figures 6.16(a) and 6.16(b) compare the ARMA reflection and transmission response simulations with the measured responses. The results show both the lossless
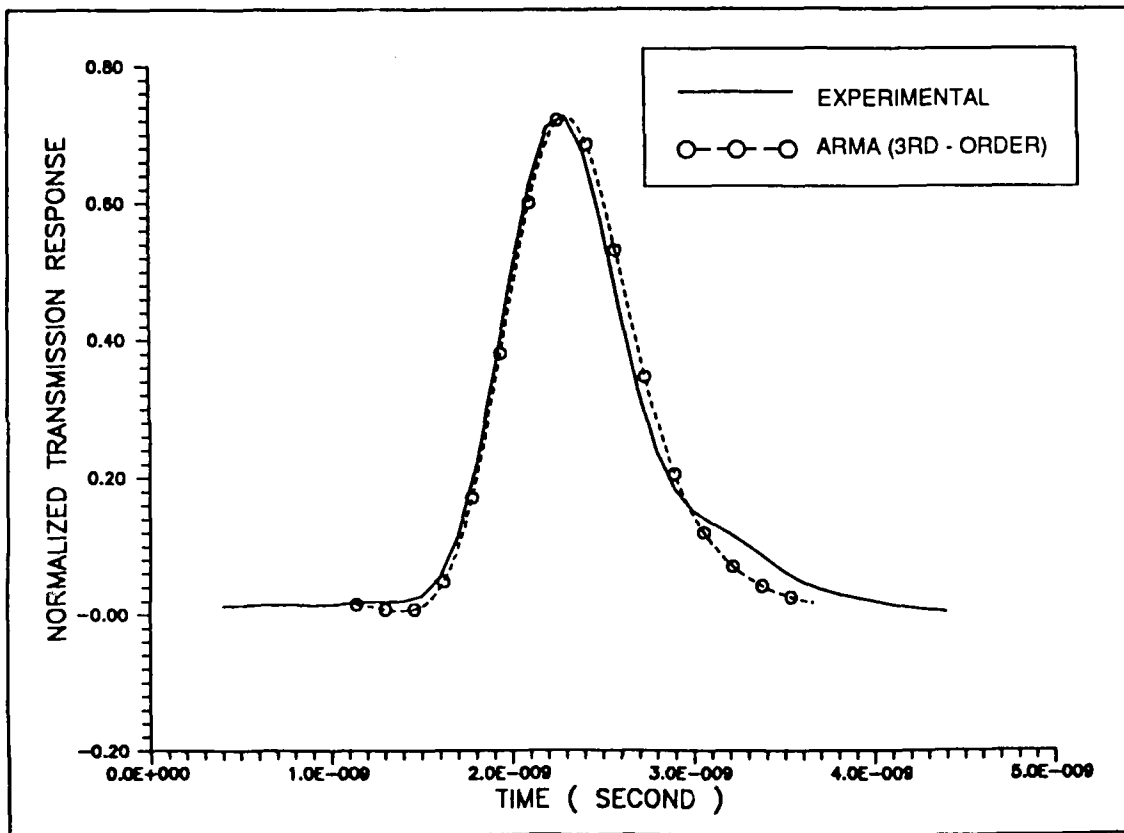
Figure 6.15   3rd-order ARMA model transmission response

and lossy (0.0348 nepers) simulated output waveforms. When the attenuation loss is included, the waveform agreement improves, especially with respect to the peak amplitudes.

Finally, a 1st-order AR model is given by (4.21) as

$$T_{AR}(z) = \frac{0.68}{1 - 0.507z^{-1}} \qquad (6.11)$$

at a sampling interval of 200 ps. The normalized AR transmission response is compared to the measured response in Figure 6.17.

95
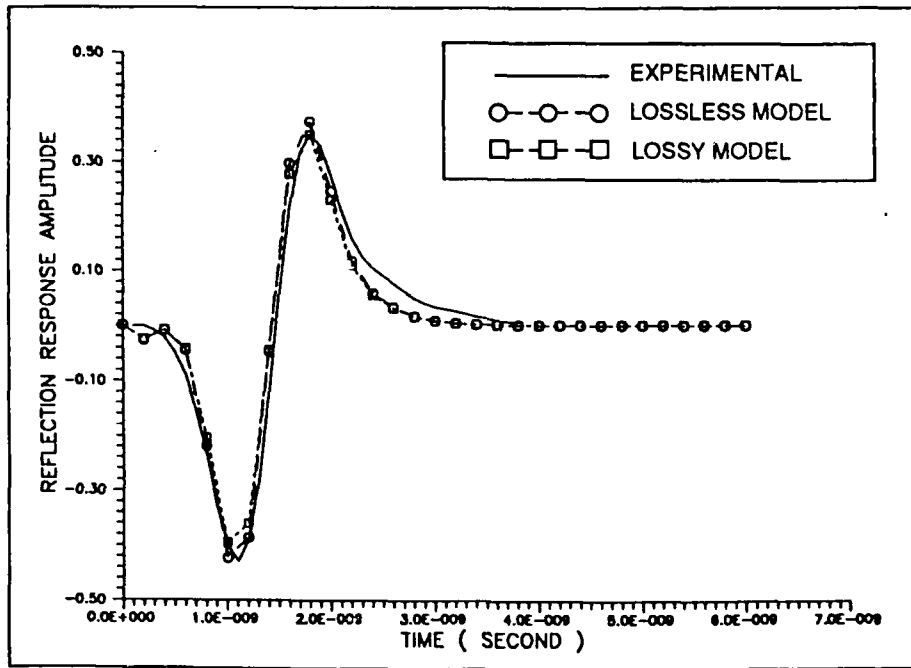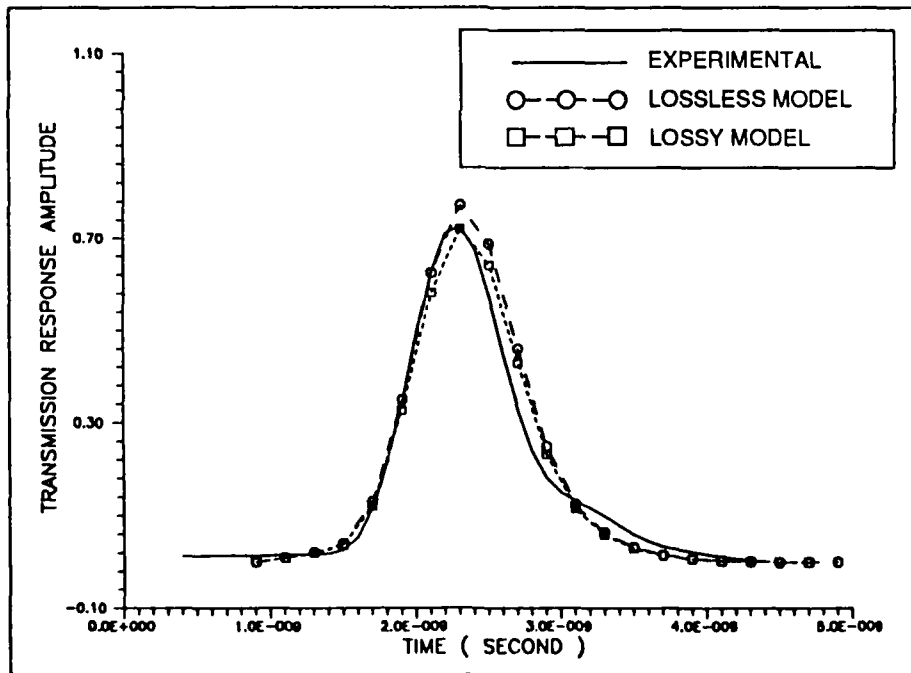
Figure 6.16 1st-order ARMA (a) reflection response and (b) transmission response

3. Estimation Results

a. Estimation of Reflection Impulse Response

An appropriate parametric model for the cascaded microstrip step discontinuity is estimated from only the measured incident and reflected responses. An estimate of the reflection sample impulse response is obtained by deconvolving the measured reflection response with the incident pulse. Figure 6.18 shows the estimated reflection sample impulse response at a sampling interval of 200 ps.
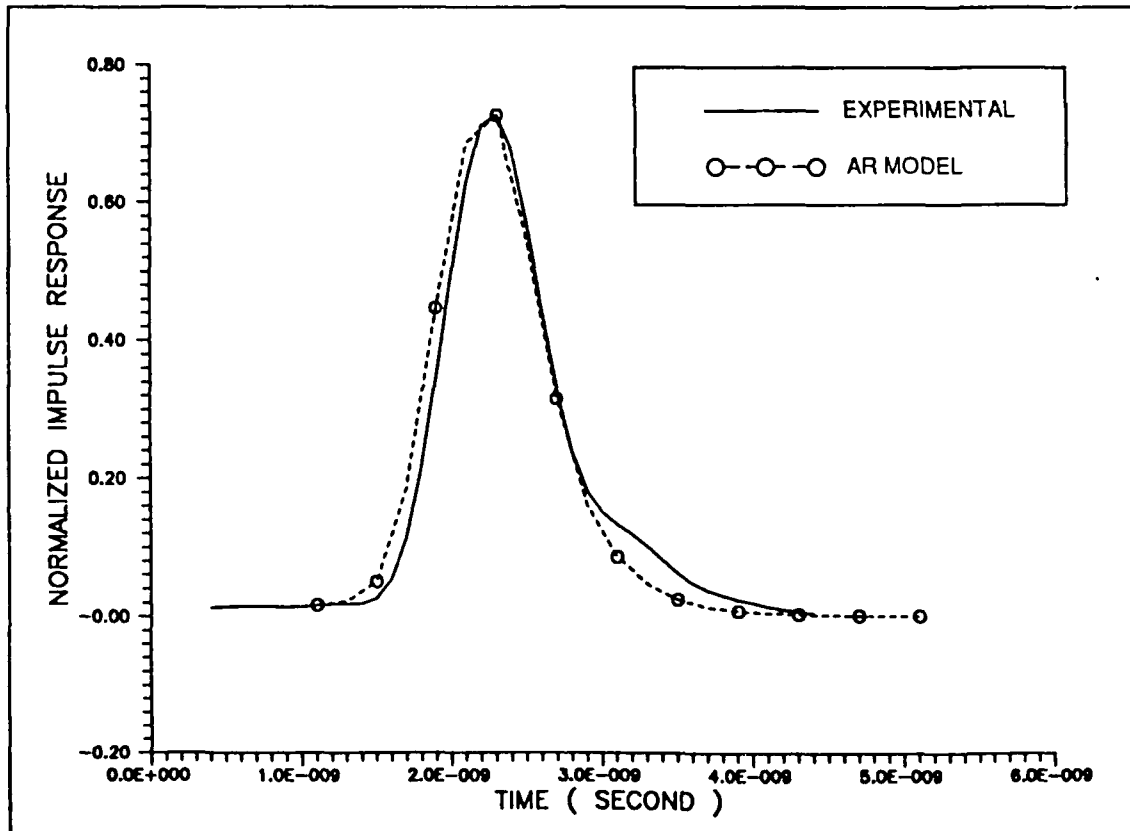
Figure 6.17   1st-order AR transmission response

b. Estimation of Model Parameters

The WLS algorithm estimates the 1st-order AR model parameter of equation (4.21) using the previously estimated reflection impulse response. The time constant ($C_\pi Z_{02}$) is solved as 291.51 ps using an estimated 1st-order AR filter coefficient of 0.5035.

97

Next the 1st-order ARMA model parameters are calculated by substituting this time constant value into equation (4.20c). Therefore, the unknown transmission response can also be approximated from observing only the incident and reflected data. Finally, the ARMA and AR model parameter estimates are given in
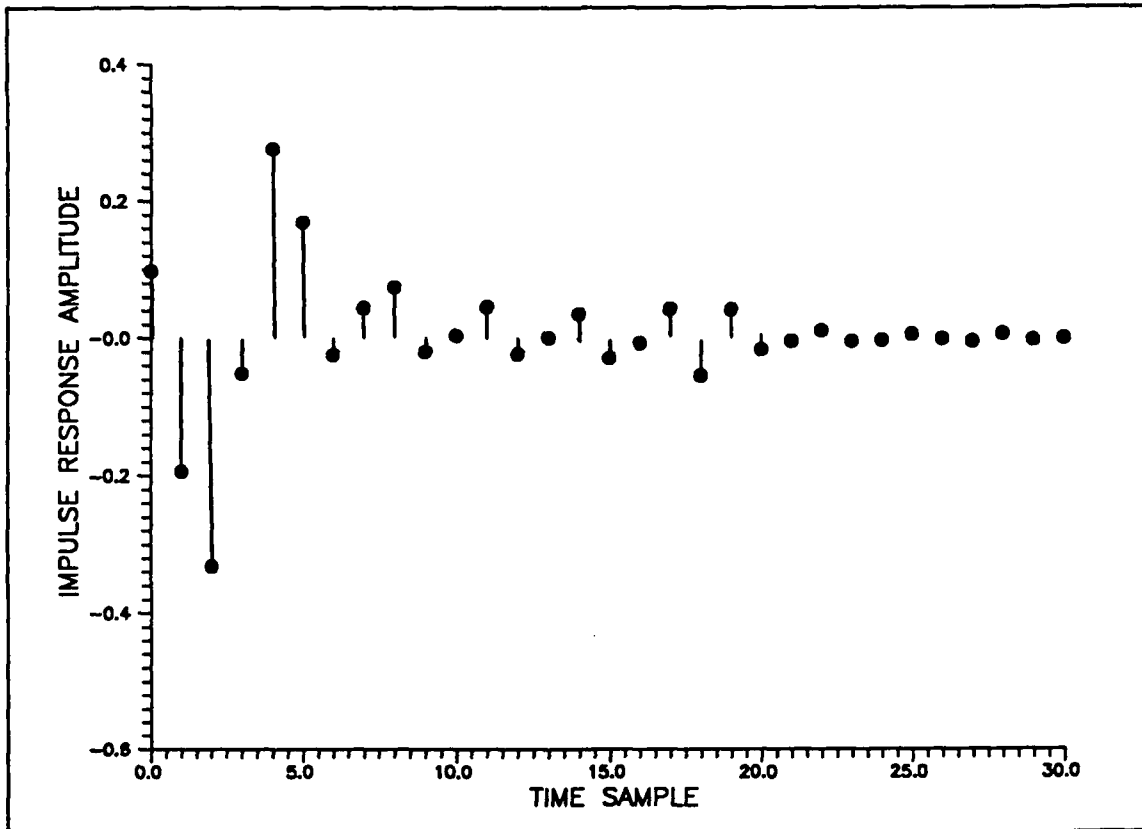
Figure 6.18 Estimated reflection sample impulse response

Table 15. This approach will be exploited by the *layer-probing* algorithm in the next section for the system identification of a multi-section microstrip structure [Ref. 54].

98

Table 15. MODEL PARAMETER ESTIMATES

ARMA Parameter	Theoretical	Estimated
b_0	0.2538	0.2554
a_1	0.4924	0.4892
AR Parameter		
a	0.5065	0.5035

C. MULTI-SECTION STEP DISCONTINUITY RESULTS

As we saw earlier, a cascaded step microstrip discontinuity can be modeled by an equivalent circuit or by an AR parametric model. We will now extend these models for a multi-section microstrip step discontinuity.

1. Equivalent Lumped-Distributed Circuit Model

a. Theoretical Results

The capacitive shunt equivalent circuit model, as shown in Figure 4.4, will be used to characterize each cascaded step discontinuity. The high impedance (narrow microstrip width) lines which connect each discontinuity are modeled as lossless distributed transmission-line sections using (2.24). The propagation delay time associated with each transmission line is determined from the physical length and the frequency-dependent effective microstrip permittivity. Figure 6.19 describes the multi-section microstrip structure which will be modeled and simulated using PSPICE. Three different line width dimensions are referred to by numbered line segments. Specific equivalent circuit numerical results are listed in Table 16 for each line segment. The theoretical calculations use a maximum design frequency of 4 GHz and a substrate relative dielectric constant ϵ_r of 4.3. Frequency dispersion is incorporated into the circuit model by using frequency dependent effective microstrip permittivity $\epsilon_{eff}(f)$ and characteristic impedance $Z_0(f)$ values.

The characteristic impedance is calculated using [Ref. 18: pp. 81-82]

$$Z_0(f) = \frac{376.6\,h}{w_{eff}(f)\sqrt{\epsilon_{eff}(f)}} \tag{6.12}$$

where

$$w_{eff}(f) = w + \frac{w_{eff} - w}{1 + \left(\dfrac{f}{f_p}\right)^2} \, ,$$

$$f_p = \frac{c}{2\,w_{eff}\sqrt{\epsilon_{eff}}}$$

and the effective width is

$$w_{eff} = \frac{376.7\,h}{Z_0\sqrt{\epsilon_{eff}}}$$
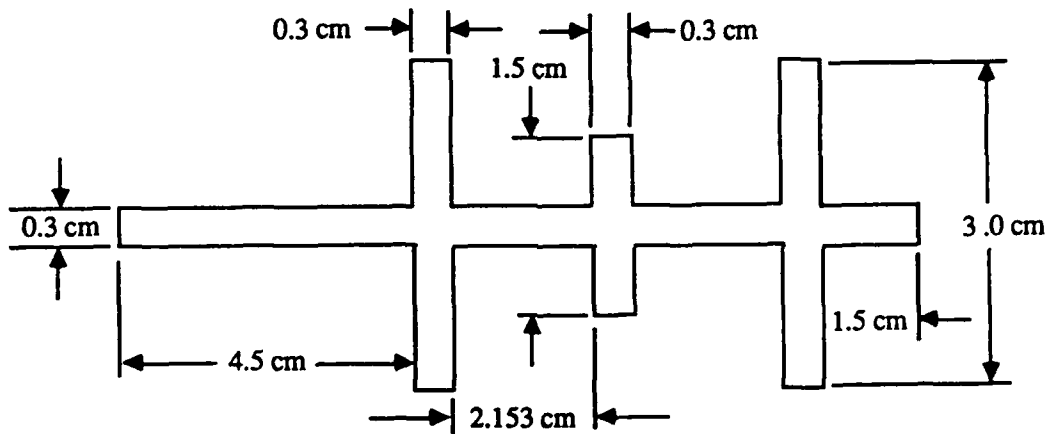
Figure 6.19 Multi-section microstrip discontinuity test structure

The theoretical propagation losses are given in Table 17 for each line segment. The total segment loss in dB/λ_g is the sum of each segment dielectric α_d and conductor α_c loss, given by

$$\alpha_d = \frac{27.3\,\epsilon_r\left(\epsilon_{eff} - 1\right)\tan\delta}{\epsilon_{eff}\left(\epsilon_r - 1\right)} \, , \tag{2.10}$$

$$\alpha_c = \frac{0.072\sqrt{f}\lambda_g}{w\,Z_0(f)} \tag{2.8b}$$

where $\tan\delta$ is the dielectric loss tangent and f is in GHz.

100

Table 16. MULTI-SECTION MICROSTRIP THEORETICAL RESULTS

Microstrip Parameter		Equation	Value
Narrow (0.3 cm) Segment No. (1)			
Static Effective Permittivity	$\epsilon_{eff}^{(1)}$	(2.2)	3.244
Frequency-Dependent Eff. Permittivity $\epsilon_{eff}^{(1)}(f)$		(2.6)	3.358
Static Characteristic Impedance	$Z_0^{(1)}$	(2.3a)	51.3 Ω
Frequency-Dependent Impedance	$Z_0^{(1)}(f)$	(6.12)	53.0 Ω
Guide Wavelength	$\lambda_g^{(1)}$	(2.19)	41.00 mm
Wide (3 cm) Segment No. (2)			
Static Effective Permittivity	$\epsilon_{eff}^{(2)}$	(2.2)	3.953
Frequency-Dependent Eff. Permittivity $\epsilon_{eff}^{(2)}(f)$		(2.6)	4.100
Static Characteristic Impedance	$Z_0^{(2)}$	(2.3a)	8.5 Ω
Frequency-Dependent Impedance	$Z_0^{(2)}(f)$	(6.12)	9.5 Ω
Guide Wavelength	$\lambda_g^{(2)}$	(2.19)	37.04 mm
Shunt Capacitance	$C_S^{(2)}$	(4.7)	2.14 pF
Wide (1.5 cm) Segment No. (3)			
Static Effective Permittivity	$\epsilon_{eff}^{(3)}$	(2.2)	3.755
Frequency-Dependent Eff. Permittivity $\epsilon_{eff}^{(3)}(f)$		(2.6)	3.922
Static Characteristic Impedance	$Z_0^{(3)}$	(2.3a)	15.7 Ω
Frequency-Dependent Impedance	$Z_0^{(3)}(f)$	(6.12)	17.5 Ω
Guide Wavelength	$\lambda_g^{(3)}$	(2.19)	37.87 mm
Shunt Capacitance	$C_S^{(3)}$	(4.7)	1.13 pF
Step Discontinuity Circuit Parameters			
Shunt Capacitance	$C_d^{(2)}$	(4.3a)	0.723 pF
Shunt Capacitance	$C_d^{(3)}$	(4.3a)	0.213 pF

101

The total propagation loss (in dB) for each microstrip line is modeled in the circuit model by a resistive attenuator π-networks. Figure 6.20 shows the equivalent circuit

Table 17. MULTI-SECTION MICROSTRIP THEORETICAL LOSSES

Microstrip Attenuation		Equation	Value
Narrow (0.3 cm) Segment No. (1)			
Dielectric Loss	$\alpha_d^{(1)}$	(2.10)	0.450 dB/λ_g
Conductor Loss	$\alpha_c^{(1)}$	(2.8b)	0.037 dB/λ_g
Total Segment Loss	$\alpha_t^{(1)}$		0.487 dB/λ_g
Wide (3 cm) Segment No. (2)			
Dielectric Loss	$\alpha_d^{(2)}$	(2.10)	0.484 dB/λ_g
Conductor Loss	$\alpha_c^{(2)}$	(2.8b)	0.019 dB/λ_g
Total Segment Loss	$\alpha_t^{(2)}$		0.503 dB/λ_g
Wide (1.5 cm) Segment No. (3)			
Dielectric Loss	$\alpha_d^{(3)}$	(2.10)	0.477 dB/λ_g
Conductor Loss	$\alpha_c^{(3)}$	(2.8b)	0.021 dB/λ_g
Total Segment Loss	$\alpha_t^{(3)}$		0.498 dB/λ_g

model for the microstrip filter of Figure 6.19.

b. Simulation Results

The microstrip filter was fabricated on G-10 epoxy dielectric material. Scattering parameter measurements were taken using the network analyzer. A piecewise-linear approximation of the measured excitation signal is used in the PSPICE circuit simulation. The transient analysis of the equivalent circuit model provides both reflection and transmission responses. Shown in Figure 6.21 is a comparison between the measured and simulated reflection responses. The amplitude of the simulated response indicates that the theoretical losses are slightly greater than

than the measured losses. The magnitude spectrum of the reflection responses is shown in Figure 6.22.
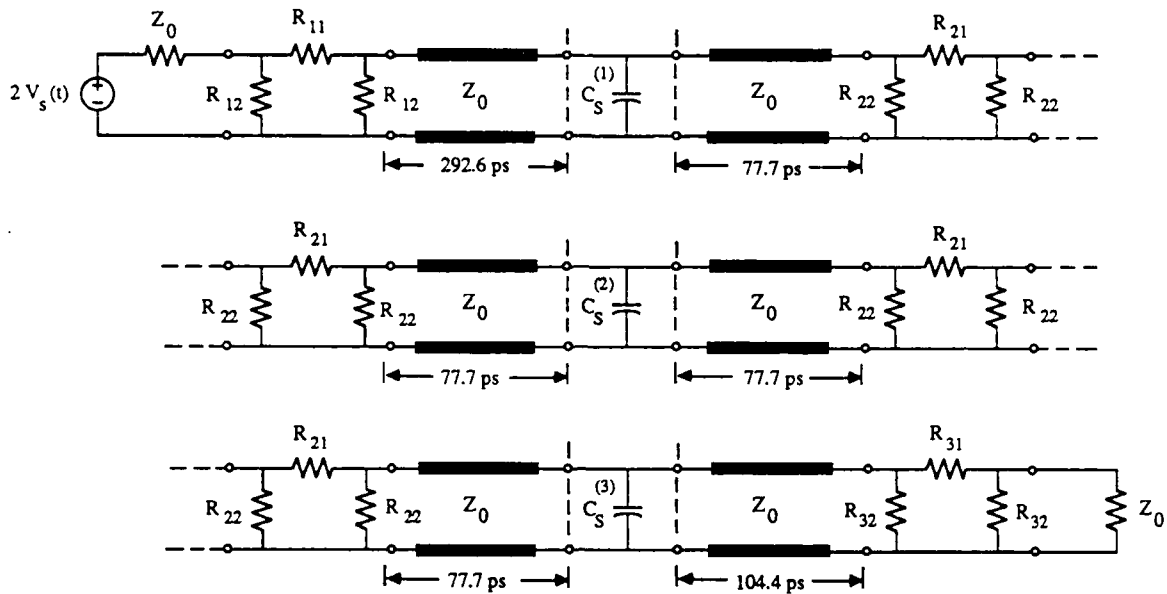
Figure 6.20 Multi-section equivalent circuit model

The multi-section microstrip filter is also simulated by *PUFF*, a computer-aided design (CAD) program for microwave integrated circuits [Ref. 55]. The *PUFF* simulation solves the scattering parameters for the microstrip filter described in Figure 6.19. The inverse FFT is performed on the scattering parameters to obtain the reflected and transmitted impulse responses. The *PUFF* program input excitation is a gaussian-shaped unit amplitude pulse. In order to accurately compare both the simulation results, a piecewise-linear approximation of the *PUFF* excitation was used in the PSPICE transient analysis. Figures 6.23 and 6.24 compare the reflection and transmission responses, respectively. The *PUFF* simulation model does not account for propagation losses.

Figure 6.24 illustrates the effect of losses in the equivalent circuit model. The influe ..e of loss and dispersion on the multiple reflected signals can be observed in the Figure 6.23 by the apparent phase shift in the PSPICE simulation.
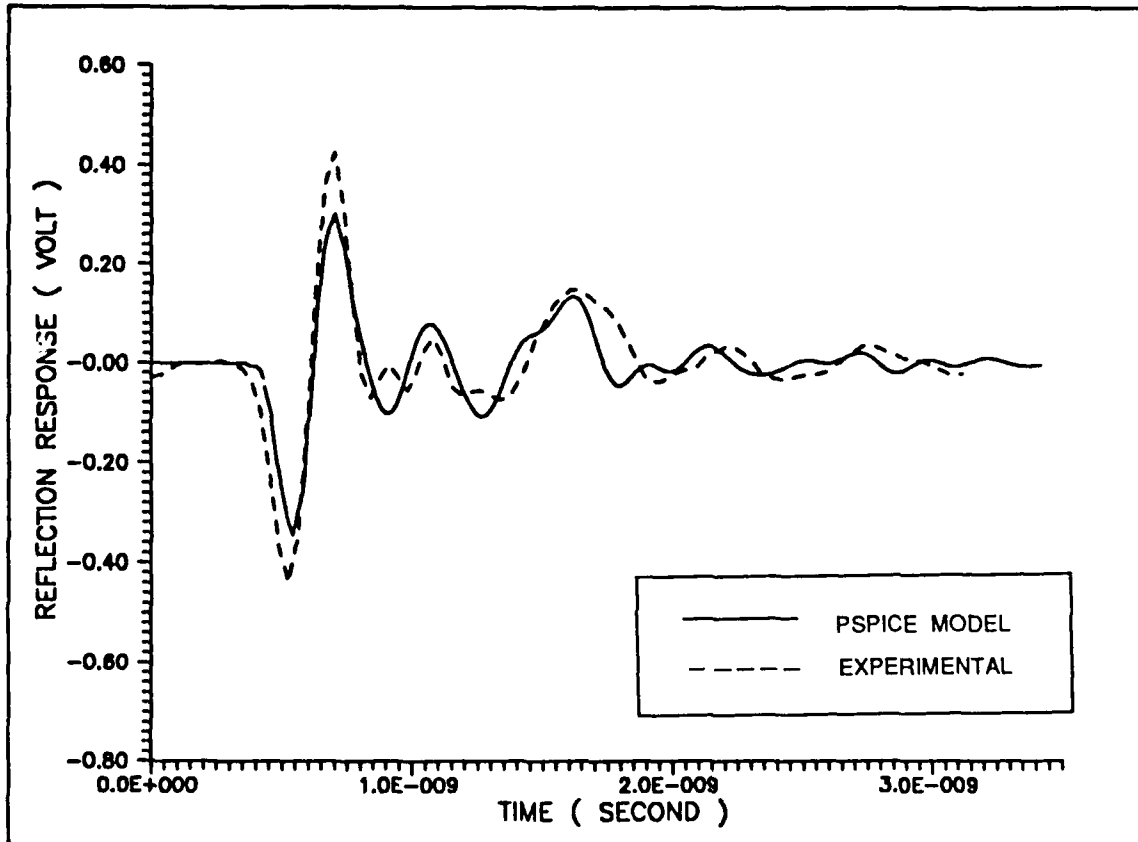
Figure 6.21   Comparison of PSPICE reflection response waveforms

104
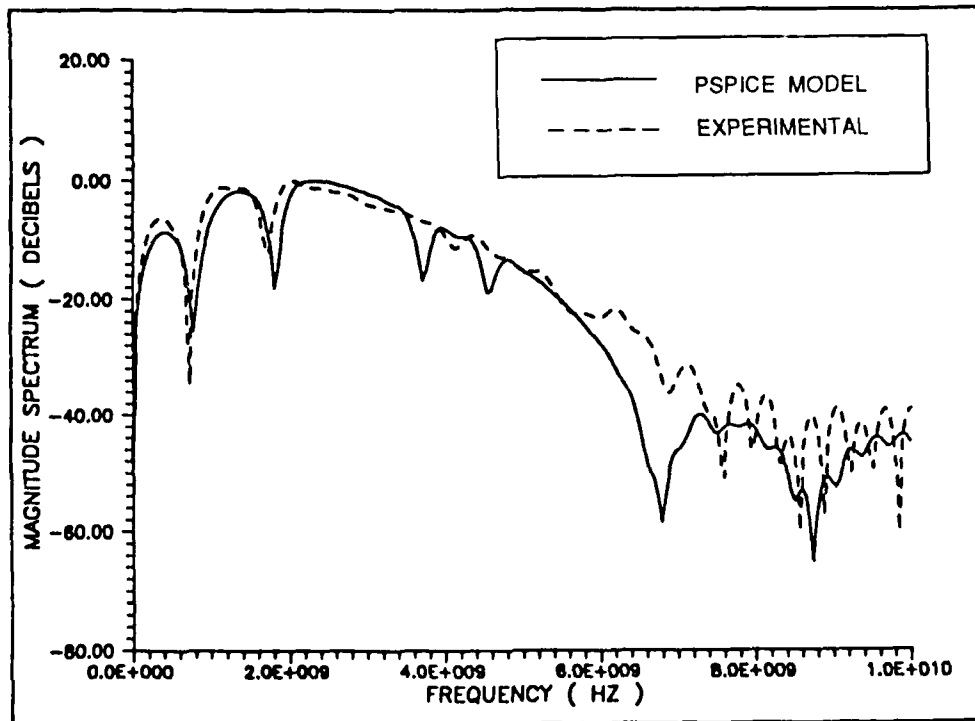
Figure 6.22   PSPICE reflection response magnitude spectrum
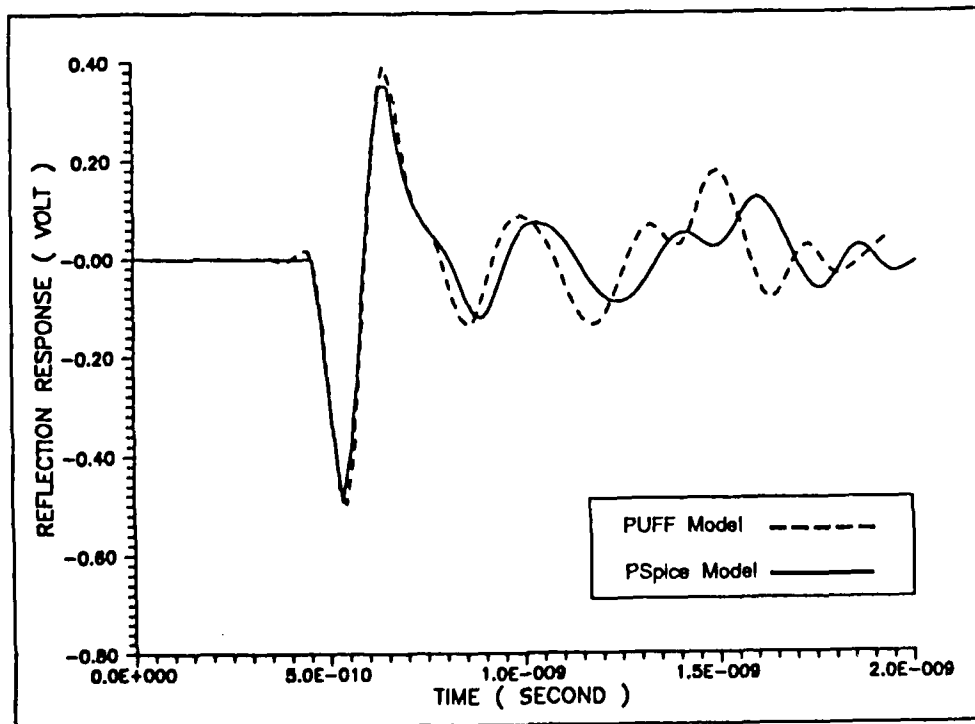
Figure 6.23   Comparison of simulated reflection responses

105

2. Layer-Probing Simulation Results

A lumped-distributed equivalent circuit is developed for a three-sectioned microstrip step discontinuity structure. A PSPICE transient analysis is performed
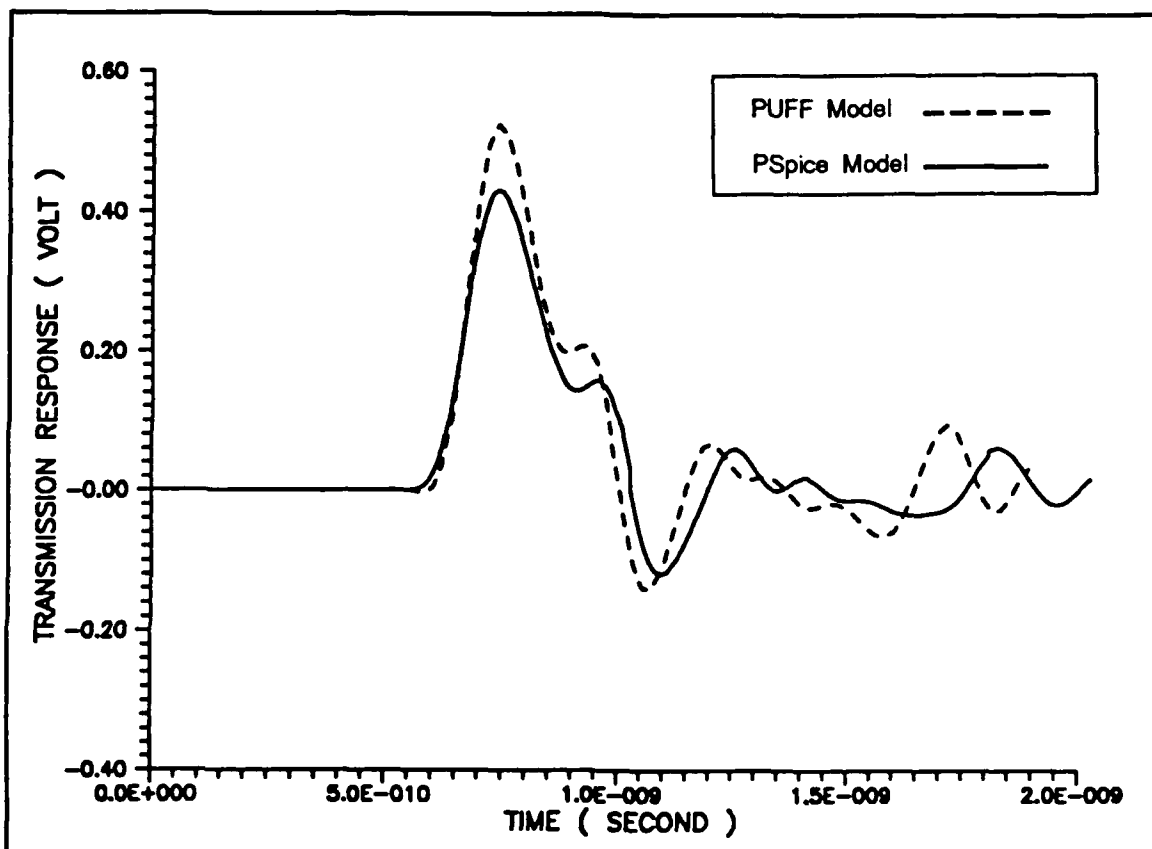
Figure 6.24   Simulated transmission responses

using the equivalent circuit model. Reflection and transmission response data will be applied to the layer reflection coefficient estimation and *layer-probing* algorithms. The initial reflection impulse response data is applied to a Fortran program implementation of the layer reflection coefficient estimation algorithm. As shown in Figure 6.25, a sign change in the layer reflection coefficient sequence corresponds to an abrupt width change on the microstrip line. An estimated group velocity of

2.53 mm/sample is computed from a measured propagation time delay of 707.9 ps and a structure length of 112 mm. Figure 6.26 shows the impedance profile
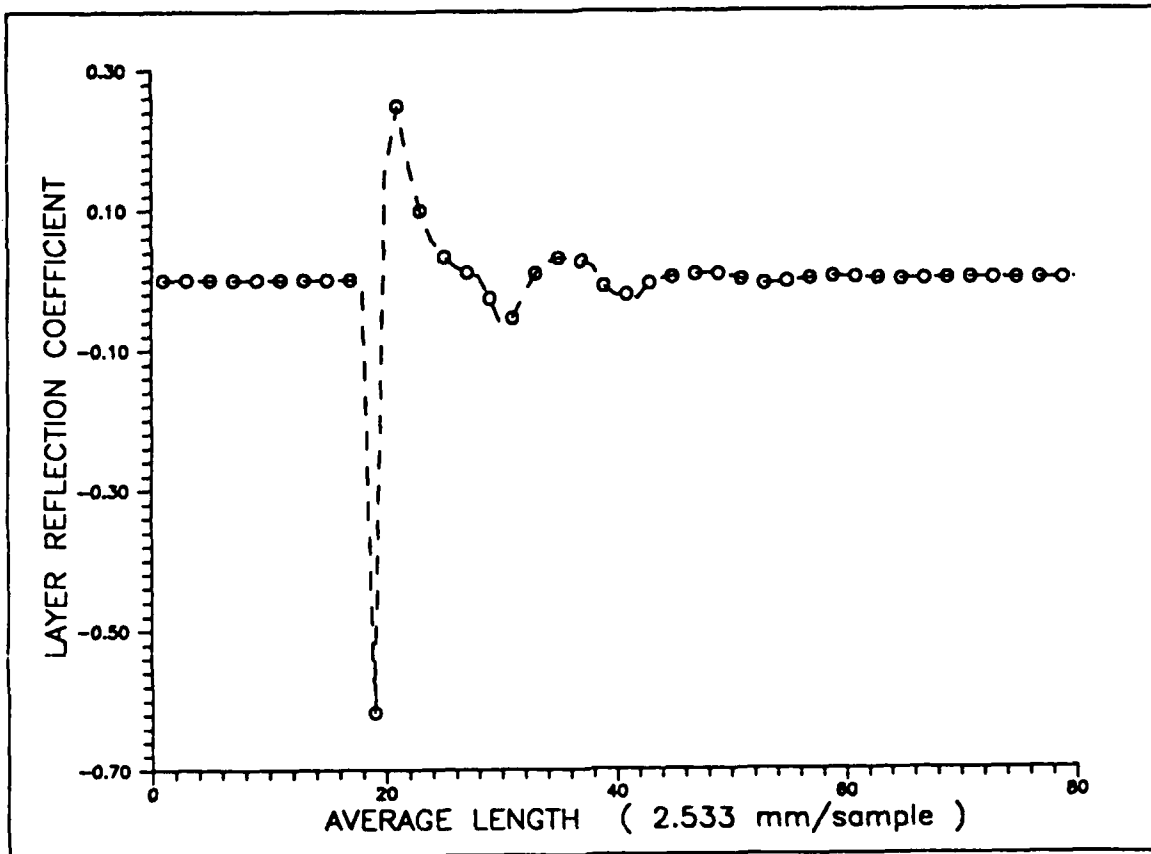
Figure 6.25   Multi-section layer reflection coefficient sequence

computed from the estimated layer reflection coefficients. The accuracy of the impedance profile degrades rapidly beyond the first discontinuty because of loss and dispersion. Nevertheless, we are able to detect the relative changes in the impedance profile and then estimate the number of discontinuities within the structure. This result is more qualitative than quantitative. The detection resolution performance

of the algorithm is dependent upon the sampling interval used. Accurate layer reflection coefficients are obtained only when the sampling interval is sufficiently small.
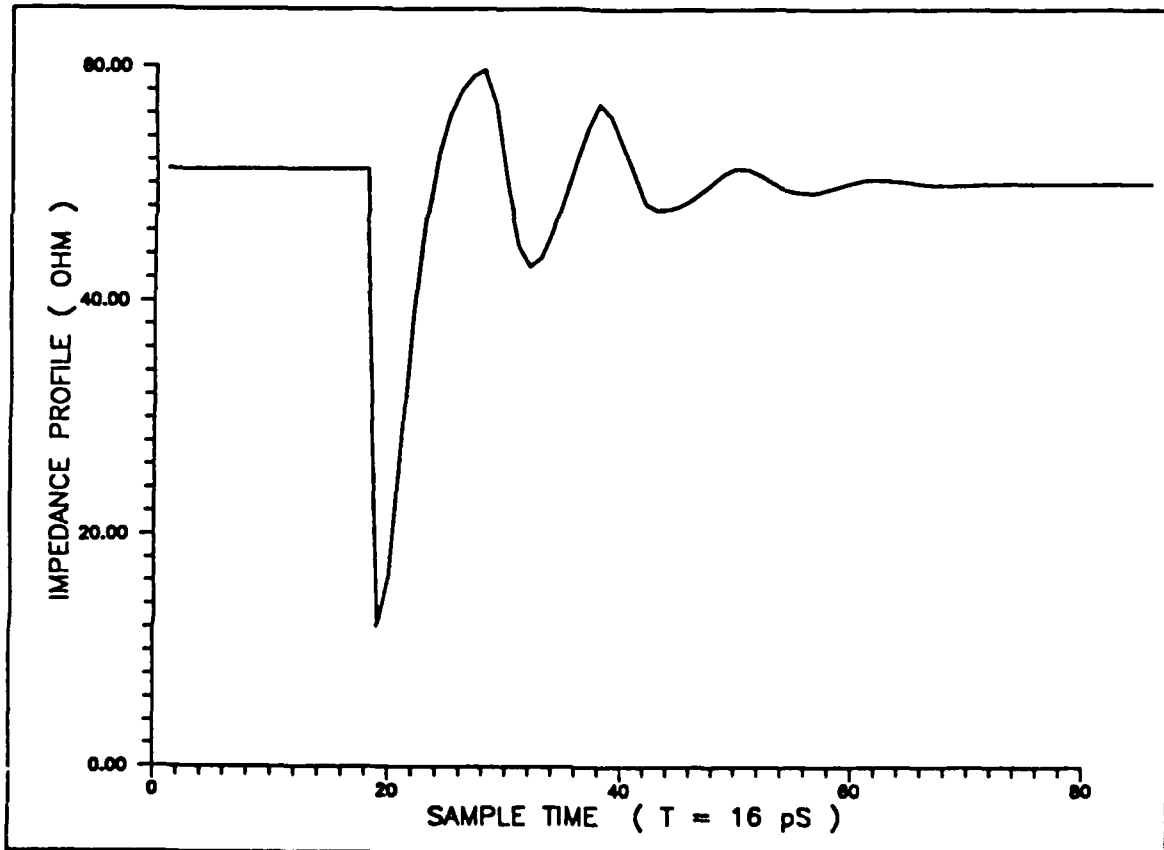
Figure 6.26   Multi-section impedance profile

The WLS algorithm was used to efficiently compute a 1st-order AR model from the reflected impulse response shown in Figure 6.27. The *layer-probing* algorithm next formulates an appropriate inverse filter using the estimated AR model parameter. A new excitation signal is simulated from the difference equation description of the first inverse filter transfer function. We create a piecewise-linear approximation of the customized input and initiate a second transient analysis in

108

PSPICE to simulate the pulse propagating in the microstrip. The resulting second reflection response is windowed to eliminate the reflected energy caused by the first
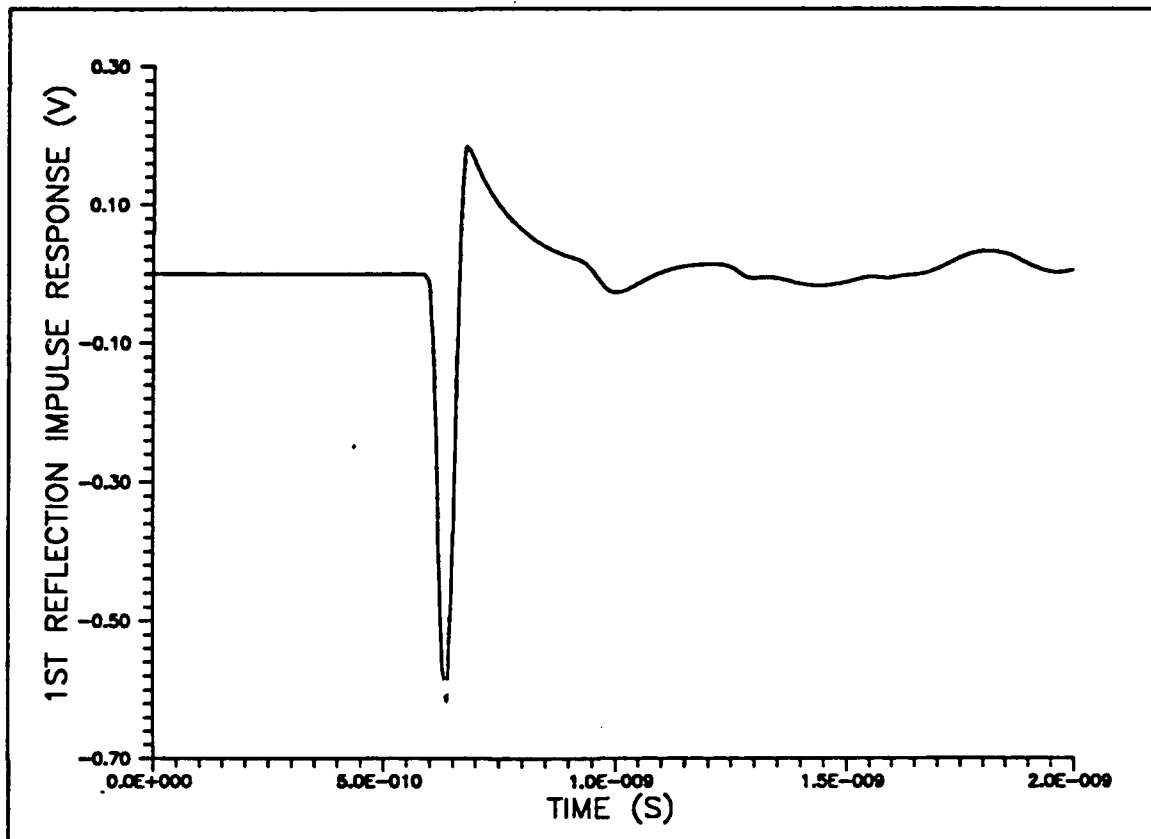
Figure 6.27   Initial reflection response waveform

discontinuity. The windowed reflection response is shown in Figure 6.28. The reflection response is now deconvolved with the estimated transmission impulse response of the first discontinuity. Figure 6.29 shows the result of the deconvolution. The WLS algorithm is used to estimate another 1st-order AR model that will describe the second discontinuity. The previous AR model parameter estimates are used to design a 2nd-order inverse filter. Next, we excite the difference equation description

of the inverse filter using the original input pulse. A third excitation sequence is generated to probe the microstrip. Once again a piecewise-linear approximation of the third customized input is entered in PSPICE. Figure 6.30 shows the transmission
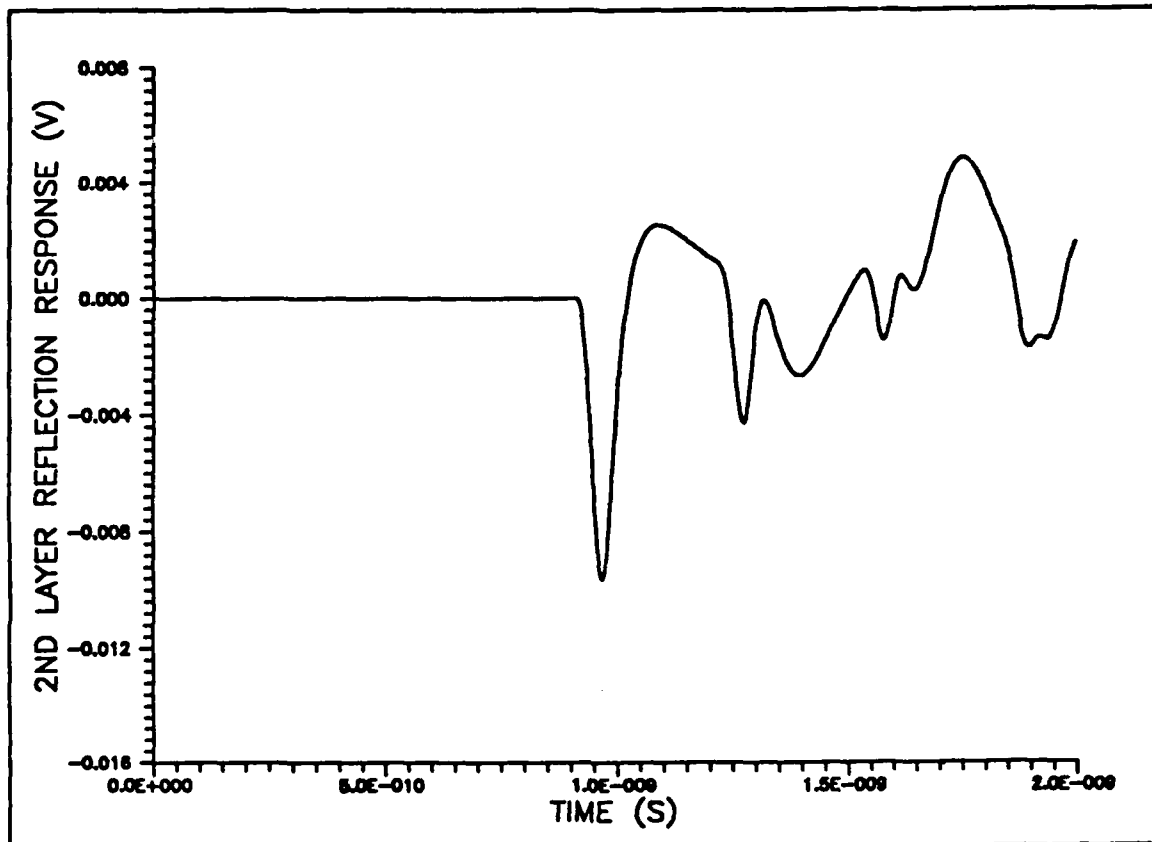
Figure 6.28   2nd windowed reflection response

response simulated by the multi-section equivalent circuit model. The simulated transmission response immediately reveals the transmitted impulse response of the third discontinuity. The transmitted impulse response is identified as the exponentially decaying transient shown in Figure 6.30. Finally, a third AR model is

110

obtained from the transmitted impulse response using the WLS algorithm. The purpose of the *layer-probing* algorithm was to resolve the reflected and transmitted impulse response for each cascaded step discontinuity. This was accomplished
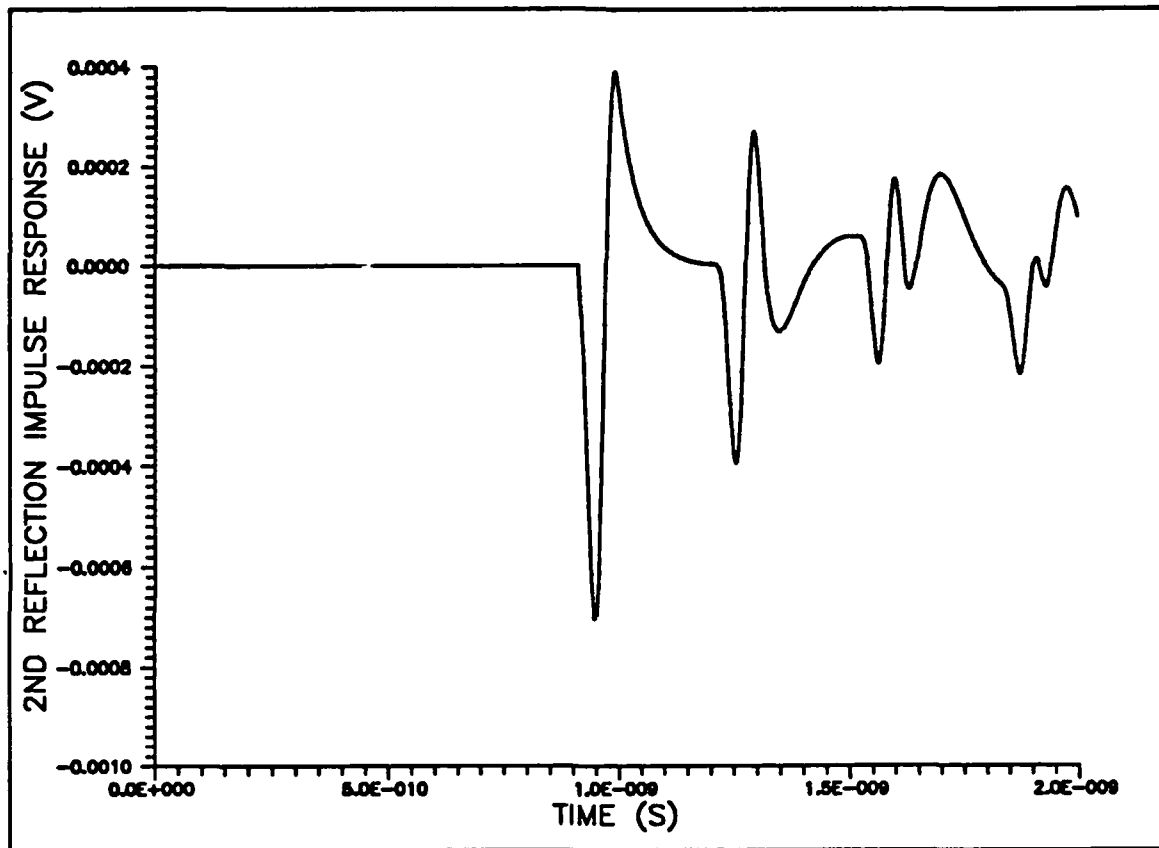
Figure 6.29   2nd reflected impulse response after deconvolution

by iterately "probing" the multi-section structure with customized signals synthetically produced by inverse filtering. Table 18 compares the estimated AR model parameters with the theoretical values used in the simulation.

111

The multi-section microstrip structure of Figure 6.19 was excited by a 18.5 GHz incident pulse. The performance of the layer reflection coefficient

Table 18. MULTI-SECTION MODEL PARAMETER ESTIMATES

Discontinuity Parameter		Theoretical	Estimated
a_1	(T = 2.0 ps)	0.9829	0.9816
a_2	(T = 2.0 ps)	0.9560	0.9567
a_3	(T = 2.5 ps)	0.9766	0.9769
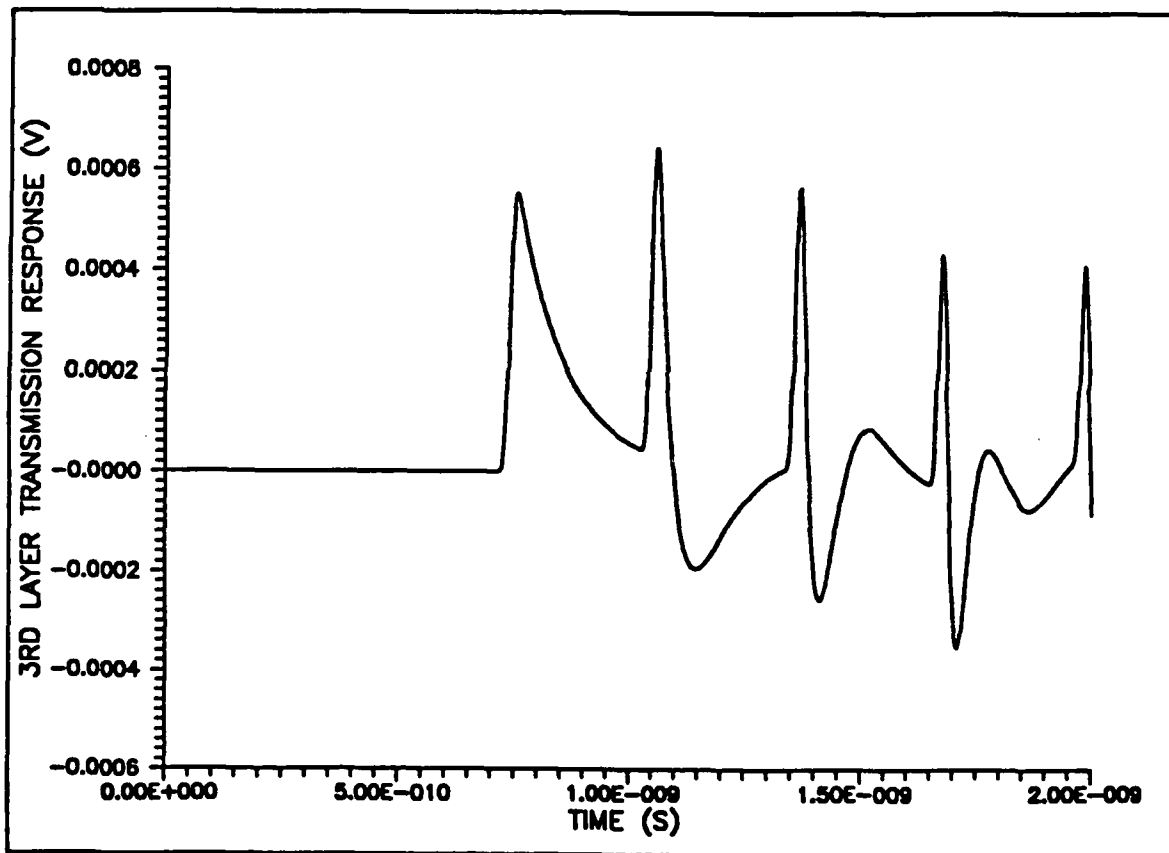
Figure 6.30   Third discontinuity transmitted impulse response

112

estimation algorithm is studied using the measured reflection response shown in Figure 6.31. The layer reflection coefficients are shown in Figure 6.32.
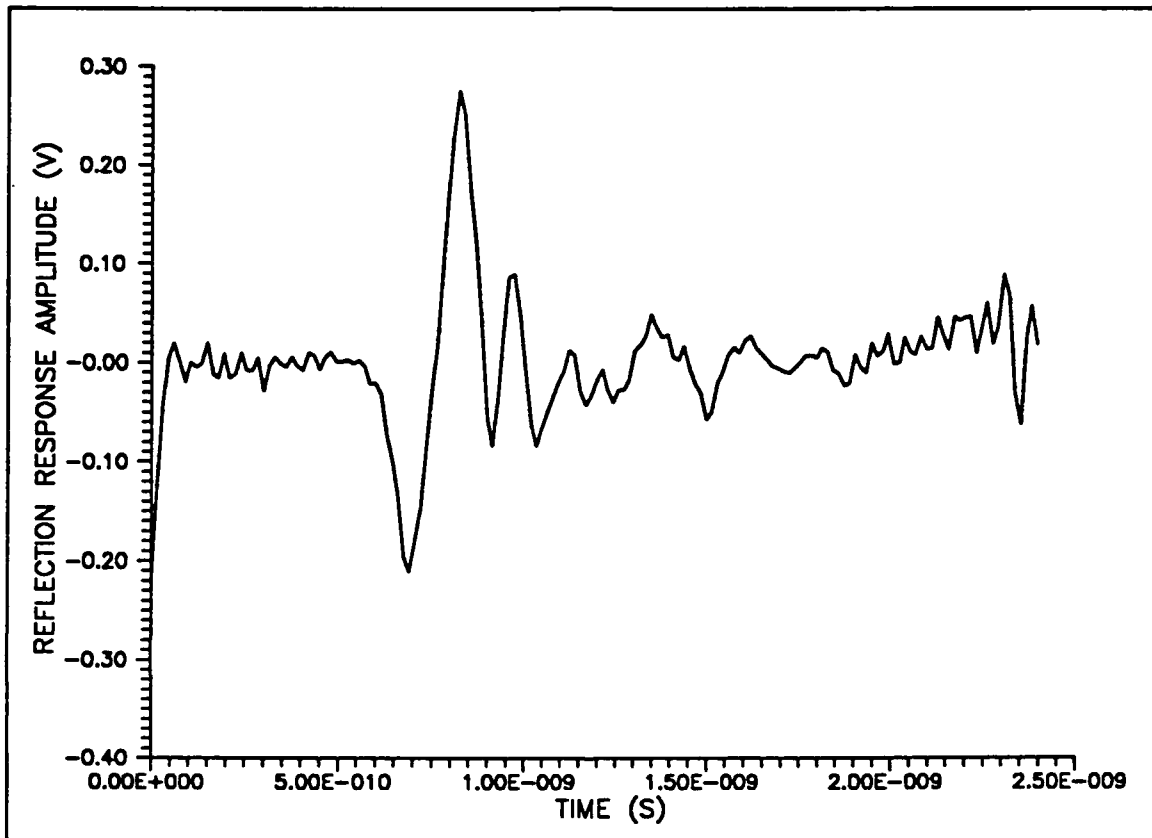
Figure 6.31 Measured reflection response due to the 18.5 GHz pulse

However, the estimated reflection coefficient values rapidly decreased in amplitude after the 30th sample value. In Figure 6.31, we can observe a significant initial reflection which is followed by several lower amplitude transients. The primary reflection is due to the first discontinuity, while the subsequent transients are distorted by the multiple reflections. Next, the impedance profile is computed from the estimated reflection coefficients using an initial impedance value of 50Ω.

113

Referring to Figure 6.33, a characteristic impedance of 12Ω is estimated for the first step discontinuity as compared with a theoretical value of 9.5Ω at 4 GHz.
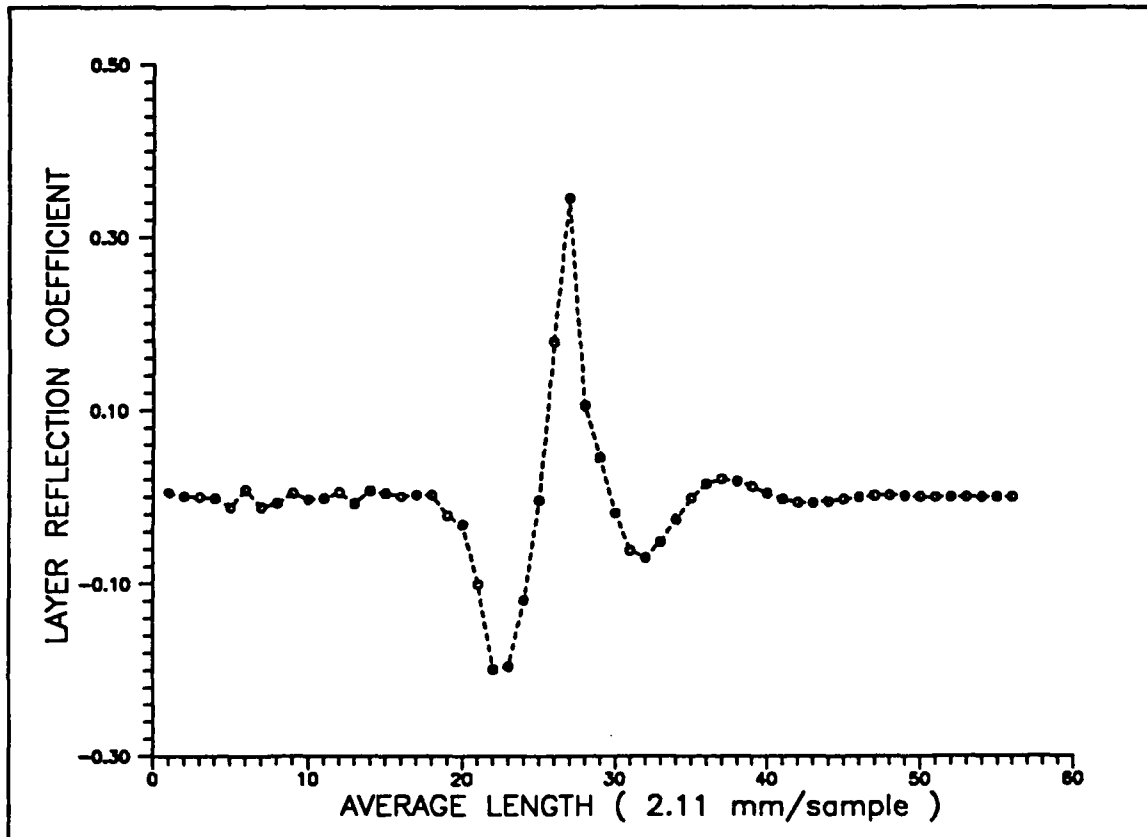
Figure 6.32   Layer reflection coefficient estimate using measured data

The impedance profile estimates a 50Ω microstrip line following the initial discontinuity. This narrow impedance estimate compares favorably to the theoretical value of 53Ω.

     The simulation and measured results presented in this section have demonstrated the performance of the *layer-probing* algorithm. However, the algorithm assumes that the multiple discontinuities can be accurately modeled by cascading minimum-phase transfer functions. A practical realization of the algorithm could

be achieved by using optoelectronic picosecond sampling techniques and real-time digital signal processing. Finally, the layer impedance profile, using measured re-
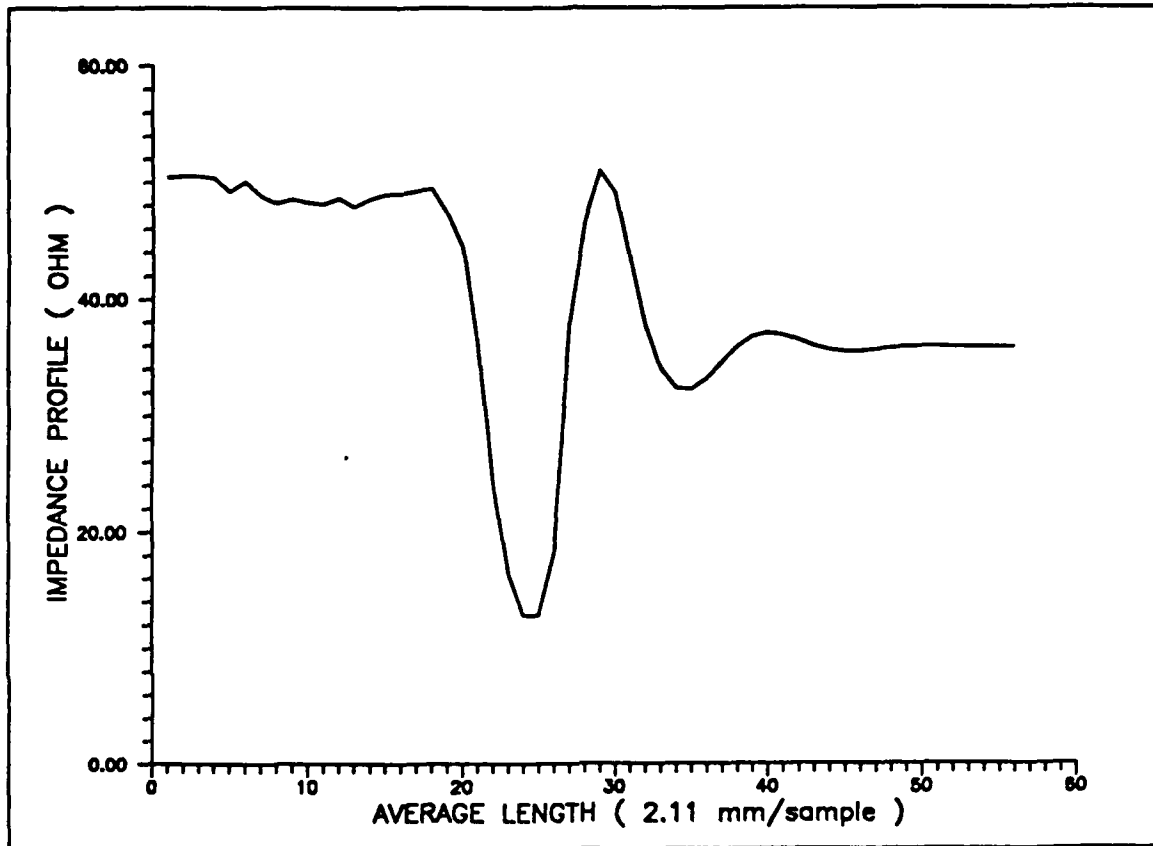
Figure 6.33 Characteristic impedance profile for multiple discontinuities

flection data, produced excellent impedance estimates for both the initial cascaded microstrip step discontinuity and the narrow 0.3 cm microstrip line.

Summarizing, we have presented both experimental and simulation results for three microstrip test structures. First, pulse propagation simulations were performed using both the equivalent circuit and ARMA/AR parametric models of an IC microstrip interconnection. Time-domain measurements were compared with the simulation results. Second, a cascaded microstrip step discontinuity was investigated. Using the equivalent circuit and parametric models derived in Chapter IV, reflection and transmission response simulations were compared with experimental results. Third, an equivalent circuit model was developed for a lossy multi-section microstrip structure consisting of several cascaded step discontinuities. The circuit model was validated by comparing PSPICE and *PUFF* simulations with microwave measurements. Finally, the parameter estimation algorithms, presented in Chapter V, were applied to simulated and measured response data in order evaluate their performance.

VII. SUMMARY AND CONCLUSION

With the development of automated optoelectronic measurement systems suitable for the manufacturing environment comes the problem of how to characterize microwave integrated circuit (MIC) devices and interconnections in MMIC's. This thesis has presented new computer-aided design models and parameter estimation techniques to model these MIC interconnections using picosecond time-domain measurements.

A. SUMMARY OF SIGNIFICANT RESULTS

Equivalent lumped-distributed circuit models were derived for lossy dispersive microstrip transmission line structures. The circuit models consisted of resistive and reactive lumped-elements, and distributed lossless transmission-line sections. The models were compatible with general computer-aided design techniques and simulation programs, such as PSPICE. In addition, the circuit models for the cascaded microstrip step discontinuity accurately characterized the reflected and transmitted wave propagation in the structure. These models mark a significant improvement over empirical modeling for which accurate generalized closed-form solutions are not available for CAD programs.

The picosecond sampling performance of current optoelectronic measurement systems motivates a digital signal processing framework for the modeling and analysis of high-speed transient signals. Parametric models of lossy dispersive microstrip transmission-lines provide an innovative modeling approach not previously presented by microwave engineers. The parametric model approach is emphasized for several reasons. First, the fitting of an autoregressive model to an observable time series is a linear process which can be handled using well tried and highly efficient computing algorithms. Secondly, an autoregressive moving-average model provides the smallest number of parameters for an optimal and most parsimonious

117

representation of the propagation process. Finally, the identification problem in parametric modeling, in other words choosing an AR or ARMA representation for a microstrip line, was shown to be intimately related to the critical physical properties. We have demonstrated how the effective microstrip permittivity of a MIC interconnection can be evaluated from ARMA or AR model parameters. Furthermore, parametric model simulations accurately characterized the picosecond pulse propagation on lossy dispersive microstrip structures. A first-order AR model of the cascaded microstrip step discontinuity formed the basis for the development of the multi-section microstrip structure model.

Several parameter estimation techniques were presented. Both deterministic and stochastic algorithms were developed to estimate the ARMA and AR model parameters. The weighted least squares (WLS) algorithm estimated the ARMA digital filter coefficients or model parameters from a prescribed unit impulse response. The algorithm rapidly converged when applied to several finite-length deterministic examples.

A discrete transformation of the network function approximation method, introduced by Elmore [Ref. 46], was presented. This method approximated either a first-order "all pole" or a second-order "pole-zero" network function from measured transient pulse delay and rise times. A first-order AR model and a second-order ARMA model were derived using the impulse invariant transformation of the respective network functions.

A layer reflection coefficient estimation algorithm was derived. This algorithm estimated the reflection coefficients from the sampled reflection response of a lossy multi-section microstrip structure. The algorithm assumed a constant attenuation factor and group velocity throughout the structure. The algorithm detected major discontinuities within the structure.

Finally, the *layer-probing* algorithm was developed to characterize multiple discontinuities within a multi-section microstrip transmission-line, consisting of several

step discontinuities. A minimum-phase parametric model described each discontinuity. Inverse filtering and deconvolution techniques were employed by the algorithm to iteratively probe successive sections of the structure.

B. CONCLUSIONS

The research conducted for this thesis has shown that the parametric modeling approach provides an alternative framework to characterize and analyze dispersive pulse propagation on microwave integrated circuit interconnections. The modeling of dispersive propagation on silicon and gallium arsenide microstrip structures is important because it points to a limitation in IC speeds even when transistor switching speed continue to improve. The measurements conducted and reported in this work have verified that the proposed equivalent circuit models are compatible with available computer-aided design (CAD) programs. The circuit models were developed using a combination of frequency-dependent expressions available in the literature and original analysis by the author.

The development of optoelectronic measurement systems will provide the capability to directly sample high-speed transients on the semiconductor substrates without introducing significant parasitics. With the availability of time-domain measurements, we developed new signal processing algorithms to estimate both the ARMA and AR model parameters.

The *layer-probing* algorithm presented a technique to iteratively identify individual step discontinuities in a multi-section transmission-line. Simulation results showed how destructive interference problems caused by dispersion and multiple reflections degraded the algorithm for some structures investigated. This problem was overcome by measuring and modeling the transmitted impulse response.

C. FUTURE DIRECTIONS FOR RESEARCH

The objectives of the research were successfully accomplished. Several suggestions for future research are now presented.

Researchers are currently studying optical techniques to measure nonlinear and multiport characteristics of MMIC components and circuits. Based on these experiments, nonlinear parametric models should also be investigated. The high frequency sampling capability of photoconductor devices can be integrated with pulsed laser technology to develop a picosecond time-domain measurement system using a white noise excitation. Here, several stochastic-based parameter estimation algorithms can be applied to the modeling problem.

Equivalent circuit and parametric models need to be developed for coupled microstrip, coplanar waveguide and other microstrip discontinuities, such as bends, crossings and the asymmetrical step discontinuities.

Improvements to the *layer-probing* algorithm should include: 1) the development of a method to estimate the attenuation factor of each lossy section. 2) the implementation of a minimum-phase ARMA parametric model for each section, and 3) the integration of cross-correlation techniques.

Another important aspect of this research is its extensions to other engineering problems. Future efforts envision the application of the proposed system identification algorithms to ultra-wideband (UWB) radar target identification. Emphasis is required on *time-domain* electromagnetics in measuring and computing the impulse response of targets, radar-absorbing materials, transmitting and receiving antennas. and various other media. New signal processing algorithms must be developed for impulsive radar.

Appendix A   Derivation of the Schur Recursion Algorithm

A recursive in order solution for the AR lattice filter reflection coefficients is presented. This derivation of the so-called Schur algorithm will show the computational efficiency of this algorithm over the Levinson-Durbin algorithm [Ref. 12: pp. 6-22]. The algorithm derivation will assume that the signal data is stationary.

1. List of Symbols and Definitions.

The following symbols are used in the derivation:

$y(n)$	The autoregressive (AR) signal sequence.
$\underline{b}$	The prediction error filter coefficient vector.
$\epsilon(n)$	The forward prediction error.
$\grave{e}(n)$	The backward prediction error.
$\mathcal{E}\{\bullet\}$	Expectation operator.
$[R_{yy}]$	The autocorrelation matrix of the signal $y(n)$.
$B(z)$	The z-transform of the forward model parameter.
$\grave{B}(z)$	The z-transform of the backward model parameter.
$k^{(p+1)}$	The $(p+1)$-th order model reflection coefficient, or lattice filter reflection coefficient.
$E(z)$	The z-transform of the forward prediction error.
$\grave{E}(z)$	The z-transform of the backward prediction error.
$\bar{\epsilon}^{(p)}(n)$	The (p)-th order normalized forward prediction error.
$\bar{r}^{(p)}(n)$	The (p)-th order normalized backward prediction error.
$\underline{\alpha}^{(p)}(n)$	The (p)-th order Schur forward recursion parameter.
$\underline{\beta}^{(p)}(n)$	The (p)-th order Schur backward recursion parameter.

2. Algorithm Derivation.

The present output data $y(n)$ can be estimated from the weighted summation of the past values of the output for the (p)-th order autoregressive (AR) model. This estimate is expressed as [Ref. 46: p. 150]

$$\widehat{y(n)} = \sum_{i=1}^{p} b_i \, y(n - i) \qquad (A.1a)$$

or in matrix form

$$\widehat{y(n)} = \underline{b}^T \underline{y}(n) \qquad (A.1b)$$

where

$$\underline{b}^T = [b_1 \; b_2 \; \ldots b_p]$$
$$\underline{y}^T(n) = [y(n - 1) \; y(n - 2) \; \ldots y(n - p)]$$

The prediction error is defined as the difference in the signal and its estimate or

$$e(n) = y(n) - \widehat{y(n)}$$
$$= y(n) - \underline{b}^T \, \underline{y}(n) \qquad (A.2)$$

The mean squared prediction error, expressed as a function of the prediction error filter weights $\underline{b}$, is formulated as [Ref. 56: p. 20]

$$\mathcal{E}\left\{e^2(n)\right\} = \underline{b}^T \, [R_{yy}] \; \underline{b} - 2\underline{b}^T \underline{R}_{yy} + R_{yy}(0) \qquad (A.3)$$

where

$$[R_{yy}] = \begin{bmatrix} R_{yy}(0) & R_{yy}(-1) & \ldots\ldots & R_{yy}(-p+1) \\ R_{yy}(1) & R_{yy}(0) & \ldots\ldots & R_{yy}(p) \\ \vdots & \vdots & \ddots & \vdots \\ R_{yy}(p-1) & \ldots & R_{yy}(1) & R_{yy}(0) \end{bmatrix}$$

and

$$\underline{R}_{yy}^T = [R_{yy}(1) \; R_{yy}(2) \; \ldots \; R_{yy}(p)]$$

The solution of (A.3) for the optimum filter weights is given by

$$\underline{b}_{opt} = [R_{yy}]^{-1} \, \underline{R}_{yy} \qquad (A.4)$$

which is commonly called the normal equations [Ref. 56: p. 22]. The normal equations can be written in matrix form as

$$
\begin{bmatrix}
R_{yy}(0) & R_{yy}(-1) & \ldots\ldots & R_{yy}(-p+1) \\
R_{yy}(1) & R_{yy}(0) & \ldots\ldots & R_{yy}(p) \\
\vdots & \vdots & \ddots & \vdots \\
R_{yy}(p-1) & \ldots & R_{yy}(1) & R_{yy}(0)
\end{bmatrix}
\begin{bmatrix}
b_1 \\
b_2 \\
\vdots \\
b_p
\end{bmatrix}
=
\begin{bmatrix}
R_{yy}(1) \\
R_{yy}(2) \\
\vdots \\
R_{yy}(p)
\end{bmatrix}
\qquad (A.5)
$$

The autocorrelation matrix $[R_{yy}]$ is Toeplitz if the signals are stationary which is assumed in this derivation. The Levinson algorithm provides the solution of the $(p+1)$-th order model parameters by using the previously determined p-th order model parameters. [Ref. 46: pp. 81-85]. The $(p+1)$-th order model parameters are obtained recursively by

$$
B^{(p+1)}(z) = B^{(p)}(z) - z^{-1}k^{(p+1)}\tilde{B}^{(p)}(z) \qquad (A.6a)
$$

$$
\tilde{B}^{(p+1)}(z) = z^{-1}\tilde{B}^{(p)}(z) - k^{(p+1)}B^{(p)}(z) \qquad (A.6b)
$$

where $B^{(p)}(z)$ is the p-th order forward model parameter transfer function, $\tilde{B}^{(p)}(z)$ is the p-th order backward model parameter transfer function, and $k^{(p+1)}$ is called the reflection coefficient. The z-transform of the forward and backward prediction error is obtained by multiplying (A.6) by Y(z).

$$
E^{(p+1)}(z) = E^{(p)}(z) - z^{-1}k^{(p+1)}\tilde{E}^{(p)}(z) \qquad (A.7a)
$$

$$
\tilde{E}^{(p+1)}(z) = z^{-1}\tilde{E}^{(p)}(z) - k^{(p+1)}E^{(p)}(z) \qquad (A.7b)
$$

In the time domain the prediction error equations become

$$
e^{(p+1)}(n) = e^{(p)}(n) - k^{(p+1)}\tilde{e}^{(p)}(n-1) \qquad (A.8a)
$$

$$
\tilde{e}^{(p+1)}(n) = \tilde{e}^{(p)}(n-1) - k^{(p+1)}e^{(p)}(n) \qquad (A.8b)
$$

To find $e^{(p+1)}(n)$ and $\tilde{e}^{(p+1)}(n)$ from $e^{(p)}(n)$ and $\tilde{e}^{(p)}(n)$, respectively, it is only necessary to determine $k^{(p+1)}$. Since the zero order prediction of a signal is $\hat{y}(n) = 0$, the zero order error is

$$
e^0(n) = \tilde{e}^0(n) = y(n) \qquad (A.9)
$$

123

and equations (A.8a) and (A.8b) can be realized as a lattice structure as shown in Figure A.1.
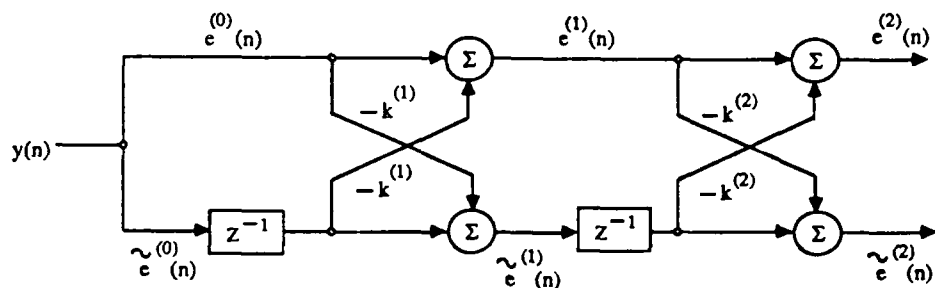
Figure A.1 Second Order AR Lattice Filter Model

The reflection coefficient $k^{(p+1)}$ can be determined by minimizing the square of the expected value of equation (A.8a) and (A.8b) with respect to the forward (k_f) and backward (k_b) reflection coefficients, respectively. The forward reflection coefficient is

$$k_f^{(p+1)} = \frac{\mathcal{E}\left\{e^{(p)}(n)\tilde{e}^{(p)}(n-1)\right\}}{\mathcal{E}\left\{\tilde{e}^{(p)}(n-1)\tilde{e}^{(p)}(n-1)\right\}} \qquad (A.10)$$

and the backward reflection coefficient is

$$k_b^{(p+1)} = \frac{\mathcal{E}\left\{e^{(p)}(n)\tilde{e}^{(p)}(n-1)\right\}}{\mathcal{E}\left\{\tilde{e}^{(p)}(n)\tilde{e}^{(p)}(n)\right\}}. \qquad (A.11)$$

The forward and backward reflection coefficients can be related to the geometric mean form as [Ref. 57: pp. 434-437]

$$k^{(p+1)} = \frac{\mathcal{E}\{e^{(p)}(n)\tilde{e}^{(p)}(n-1)\}}{\sqrt{\mathcal{E}\{\left[e^{(p)}(n)\right]^2\}\mathcal{E}\{\left[\tilde{e}^{(p)}(n-1)\right]^2\}}}. \qquad (A.12)$$

124

By substituting (A.12) into (A.10), the forward reflection coefficient becomes

$$k_f{}^{(p+1)} = k^{(p+1)} \frac{\sqrt{\mathcal{E}\{\,[e^{(p)}(n)]^2\,\}\,\mathcal{E}\{\,[\tilde{e}^{(p)}(n-1)]^2\,\}}}{\mathcal{E}\{\,[\tilde{e}^{(p)}(n-1)]^2\,\}} \qquad (A.13a)$$

$$k_f{}^{(p+1)} = k^{(p+1)} \frac{\|e^{(p)}(n)\|}{\|\,[\tilde{e}^{(p)}(n-1)]^2\,\|} \qquad (A.13b)$$

where

$$\|e^{(p)}(n)\| = \sqrt{\mathcal{E}\{\,[e^{(p)}(n)]^2\,\}}$$

and

$$\|\tilde{e}^{(p)}(n-1)\| = \sqrt{\mathcal{E}\{\,[\tilde{e}^{(p)}(n-1)]^2\,\}}$$

Similarly, the backward reflection coefficient (A.11) yields

$$k_b{}^{(p+1)} = k^{(p+1)} \frac{\sqrt{\mathcal{E}\{e^{(p)2}(n)\}\,\mathcal{E}\{\,[\tilde{e}^{(p)}(n-1)]^2\,\}}}{\mathcal{E}\{\,[e^{(p)}(n)]^2\,\}} \qquad (A.14a)$$

$$k_b{}^{(p+1)} = k^{(p+1)} \frac{\|\tilde{e}^{(p)}(n-1)\|}{\|\,[e^{(p)}(n)]^2\,\|} \qquad (A.14b)$$

Substituting (A.13b) and (A.14b) into (A.9a) and (A.9b), respectively yields

$$e^{(p+1)}(n) = e^{(p)}(n) - k^{(p+1)}\tilde{e}^{(p)}(n-1)\frac{\|e^{(p)}(n)\|}{\|\,[\tilde{e}^{(p)}(n-1)]^2\,\|} \qquad (A.15a)$$

$$\tilde{e}^{(p+1)}(k) = \tilde{e}^{(p)}(n-1) - k^{(p+1)}e^{(p)}(n)\frac{\|\tilde{e}^{(p)}(n-1)\|}{\|\,[e^{(p)}(n)]^2\,\|} \qquad (A.15b)$$

The normalized $(p+1)$-th order forward and backward prediction errors are defined as

$$\bar{e}^{(p+1)}(n) = \frac{e^{(p+1)}(n)}{\|e^{(p+1)}(n)\|} \qquad (A.16a)$$

$$\bar{r}^{(p+1)}(n-1) = \frac{\tilde{e}^{(p+1)}(n-1)}{\|\tilde{e}^{(p+1)}(n-1)\|} \qquad (A.16b)$$

Factoring $\|e^{(p)}(n)\|$ from the right side of (A.15a) and normalizing yields

$$\bar{e}^{(p+1)}(n) = \frac{\|e^{(p)}(n)\|}{\|e^{(p+1)}(n)\|}\left\{\bar{e}^{(p)}(n) - k^{(p+1)}\bar{r}^{(p)}(n-1)\right\} \qquad (A.17a)$$

Factoring $\|\tilde{e}^{(p)}(n-1)\|$ from the right side of (A.15b) and normalizing yields

$$\bar{r}^{(p+1)}(n) = \frac{\|\tilde{e}^{(p)}(n-1)\|}{\|\tilde{e}^{(p+1)}(n)\|}\left\{\bar{r}^{(p)}(n-1) - k^{(p+1)}\bar{e}^{(p)}(n)\right\} \qquad (A.17b)$$

We will next show that

$$\frac{\|e^{(p)}(n)\|}{\|e^{(p+1)}(n)\|} = \frac{1}{\sqrt{1 - \left[k^{(p+1)}\right]^2}} \qquad (A.18a)$$

and

$$\frac{\|\tilde{e}^{(p)}(n-1)\|}{\|\tilde{e}^{(p+1)}(n-1)\|} = \frac{1}{\sqrt{1 - \left[k^{(p+1)}\right]^2}} \qquad (A.18b)$$

Proof: Equation (A.18) is defined as

$$\frac{\|e^{(p)}(n)\|}{\|e^{(p+1)}(n)\|} = \frac{\left[\mathcal{E}\left\{\left[e^{(p)}(n)\right]^2\right\}\right]^{\frac{1}{2}}}{\left[\mathcal{E}\left\{\left[e^{(p+1)}(n-1)\right]^2\right\}\right]^{\frac{1}{2}}} \qquad (A.19a)$$

Squaring (A.9a) and taking the expectation yields

$$\mathcal{E}\left\{\left[e^{(p+1)}(n)\right]^2\right\} = \mathcal{E}\left\{\left[e^{(p)}(n)\right]^2\right\} - 2k_f^{(p+1)}\mathcal{E}\left\{e^{(p)}(n)\tilde{e}^{(p)}(n-1)\right\}$$
$$+ [k^{(p+1)}]^2\mathcal{E}\left\{\left[\tilde{e}^{(p)}(n-1)\right]^2\right\} \qquad (A.19b)$$

Substituting (A.10) for $k_f^{(p+1)}$, and simplifing

$$\mathcal{E}\left\{\left[e^{(p+1)}(n)\right]^2\right\} = \mathcal{E}\left\{\left[e^{(p)}(n)\right]^2\right\} - k_f^{(p+1)}\mathcal{E}\left\{e^{(p)}(n)\tilde{e}^{(p)}(n-1)\right\} \qquad (A.19c)$$

Returning to equation (A.19a), we substitute (A.19c) to yield

$$\frac{\|e^{(p)}(n)\|}{\|e^{(p+1)}(n)\|} = \frac{1}{\left[\dfrac{\mathcal{E}\left\{\left[e^{(p)}(n)\right]^2\right\} - k_f^{(p+1)}\mathcal{E}\left\{e^{(p)}(n)\tilde{e}^{(p)}(n-1)\right\}}{\mathcal{E}\left\{\left[e^{(p)}(n)\right]^2\right\}}\right]^{\frac{1}{2}}}$$

$$= \frac{1}{\left[1 - \dfrac{k_f^{(p+1)}\mathcal{E}\left\{e^{(p)}(n)\tilde{e}^{(p)}(n-1)\right\}}{\mathcal{E}\left\{\left[e^{(p)}(n)\right]^2\right\}}\right]^{\frac{1}{2}}} \qquad (A.19d)$$

126

Finally, we substitute (A.13a) for $k_f^{(p+1)}$ into (A.19d), and multiply the denominator term $\mathcal{E}\left\{ \left[e^{(p)}(n)\right]^2 \right\}$ by the ratio

$$\frac{\sqrt{\mathcal{E}\left\{ \left[e^{(p)}(n)\right]^2 \left[\tilde{e}^{(p)}(n-1)\right]^2 \right\}}}{\sqrt{\mathcal{E}\left\{ \left[e^{(p)}(n)\right]^2 \left[\tilde{e}^{(p)}(n-1)\right]^2 \right\}}}$$

simplifying yields

$$\frac{\|e^{(p)}(n)\|}{\|e^{(p+1)}(n)\|} = \frac{1}{\left[1 - \dfrac{k_f^{(p+1)}\mathcal{E}\left\{ e^{(p)}(n)\tilde{e}^{(p)}(n-1) \right\}}{\sqrt{\mathcal{E}\left\{ \left[e^{(p)}(n)\right]^2 \left[\tilde{e}^{(p)}(n-1)\right]^2 \right\}}} \right]^{\frac{1}{2}}} \qquad (A.19e)$$

$$\frac{\|e^{(p)}(n)\|}{\|e^{(p+1)}(n)\|} = \frac{1}{\sqrt{1 - \left[k^{(p+1)}\right]^2}} \qquad (A.19f)$$

Following the same approach using equations (A.9b) and (A.11), it can be shown that

$$\frac{\|\tilde{e}^{(p)}(n-1)\|}{\|\tilde{e}^{(p+1)}(n-1)\|} = \frac{1}{\sqrt{1 - \left[k^{(p+1)}\right]^2}} \qquad (A.20)$$

The normalized lattice recursion equations are from (A.17a) and (A.17b)

$$\begin{bmatrix} \bar{e}^{(p+1)}(n) \\ \bar{r}^{(p+1)}(n) \end{bmatrix} = \frac{1}{\sqrt{1 - [k^{(p+1)}]^2}} \begin{bmatrix} 1 & -k^{(p+1)} \\ -k^{(p+1)} & 1 \end{bmatrix} \begin{bmatrix} \bar{e}^{(p)}(n) \\ \bar{r}^{(p)}(n-1) \end{bmatrix} \qquad (A.21a)$$

or

$$\begin{bmatrix} \bar{e}^{(p+1)}(n) \\ \bar{r}^{(p+1)}(n) \end{bmatrix} = \theta[k^{(p+1)}] \begin{bmatrix} \bar{e}^{(p)}(n) \\ \bar{r}^{(p)}(n-1) \end{bmatrix} \qquad (A.21b)$$

where

$$\theta[k^{(p+1)}] = \frac{1}{\sqrt{1 - [k^{(p+1)}]^2}} \begin{bmatrix} 1 & -k^{(p+1)} \\ -k^{(p+1)} & 1 \end{bmatrix}$$

In order to obtain the Schur recursion equations we will introduce two new parameters, $\underline{\alpha}^{(p)}(n)$ and $\underline{\beta}^{(p)}(n-1)$ as

$$\underline{\alpha}^{(p)}(n) = \mathcal{E}\left\{\bar{e}^{(p)}(k)\, y(n)\right\} \qquad (A.22a)$$

$$= \mathcal{E}\left\{\frac{e^{(p)}(n)\, y(n)}{\|e^{(p)}(n)\|}\right\} \qquad (A.22b)$$

$$\underline{\alpha}^{(p)}(n) = \frac{\underline{R}_{yy}(n)}{\|y(n)\|} \qquad (A.22c)$$

where $\underline{R}_{yy}(n)$ is a $(p \times 1)$ correlation vector, and the norm $\|y(n)\| = \sqrt{R_{yy}(0)}$.

Similarly,

$$\underline{\beta}(k)^{(p)}(n-1) = \mathcal{E}\left\{\bar{r}^{(p)}(n-1)\, y(n)\right\} \qquad (A.23a)$$

$$= \mathcal{E}\left\{\frac{r^{(p)}(n-1)\, y(n)}{\|r^{(p)}(n-1)\|}\right\} \qquad (A.23b)$$

$$\underline{\beta}^{(p)}(n-1) = \frac{\underline{R}_{yy}(n-1)}{\|y(n-1)\|}. \qquad (A.23c)$$

Using the normalized lattice recursion equation (A.21) and the previously defined Schur recursion parameters $(\underline{\alpha}^{(p)}(n))$ and $(\underline{\beta}^{(p)}(n-1))$, the Schur recursion equation is

$$\begin{bmatrix} \underline{\alpha}^{(p+1)}(n) \\ \underline{\beta}^{(p+1)}(n-1) \end{bmatrix} = \theta(k^{(p+1)}) \begin{bmatrix} \underline{\alpha}^{(p)}(n) \\ \underline{\beta}^{(p)}(n-1) \end{bmatrix}. \qquad (A.24)$$

We will next show the $((p+1))$-th order reflection coefficient in terms of the ratio of Schur recursion parameters. From equation (A.22a) and (A.23a) we form

$$\frac{\underline{\alpha}^{(p)}(n)}{\underline{\beta}^{(p)}(n-1)} = \frac{\mathcal{E}\left\{\bar{e}^{(p)}(n)\, y(n)\right\}}{\mathcal{E}\left\{\bar{r}^{(p)}(n-1)\, y(n)\right\}} \qquad (A.25a)$$

$$= \frac{\mathcal{E}\left\{\bar{e}^{(p)}(n)\right\}}{\mathcal{E}\left\{\bar{r}^{(p)}(n-1)\right\}} \qquad (A.25b)$$

128

$$= \frac{\mathcal{E}\left\{e^{(p)}(n)\right\} \|\tilde{e}^{(p)}(n-1)\|}{\mathcal{E}\left\{\tilde{e}^{(p)}(n-1)\right\} \|e^{(p)}(n)\|} \tag{A.25c}$$

$$\frac{\underline{\alpha}^{(p)}(n)}{\underline{\beta}^{(p)}(n-1)} = \frac{\mathcal{E}\left\{e^{(p)}(n)\,\tilde{e}^{(p)}(n-1)\right\}}{\sqrt{\mathcal{E}\left\{\left[e^{(p)}(n)\right]^2\right\}}\sqrt{\mathcal{E}\left\{\left[\tilde{e}^{(p)}(n-1)\right]^2\right\}}}. \tag{A.25d}$$

Using stationarity and $\mathcal{E}\left\{\left[\tilde{e}^{(p)}(n-1)\right]^2\right\} = \mathcal{E}\left\{\left[e^{(p)}(n)\right]^2\right\}$, we have [Ref. 46: p. 168]

$$\frac{\underline{\alpha}^{(p)}(n)}{\underline{\beta}^{(p)}(n-1)} = \frac{\mathcal{E}\left\{e^{(p)}(n)\,\tilde{e}^{(p)}(n-1)\right\}}{\mathcal{E}\left\{\left[\tilde{e}^{(p)}(n-1)\right]^2\right\}} \tag{A.25f}$$

$$= k^{(p+1)}. \tag{A.25g}$$

3. Normalized Lattice Filter Realization.

This section describes the normalized lattice filter as a direct method of solving $k^{(p+1)}$ given the autocorrelation sequence $(\underline{R}_{yy})$. Assume the zero order Schur parameters are

$$\alpha^{(0)}(1) = R(1)$$
$$\beta^{(0)}(0) = R(0)$$

Inserting these initial values in (A.25) we have

$$k^{(1)} = \frac{\alpha^{(0)}(1)}{\beta^{(0)}(0)}$$
$$= \frac{R(1)}{R(0)}.$$

The first order Schur parameters for $(n = 1, 2)$ are solved using the recursion equation (A.24) as

$$\alpha^{(1)}(1) = \frac{1}{\sqrt{1 - \left[k^{(1)}\right]^2}}\left[\alpha^{(0)}(1) - k^{(1)}\beta^{(0)}(0)\right]$$

and

$$\alpha^{(1)}(2) = \frac{1}{\sqrt{1 - \left[k^{(1)}\right]^2}} \left[\alpha^{(0)}(2) - k^{(1)}\beta^{(0)}(1)\right]$$

where $\alpha^{(0)}(2) = R(2)$ and $\beta^{(0)}(1) = R(1)$. The $\beta^{(1)}(n)$ parameters are

$$\beta^{(1)}(0) = \frac{1}{\sqrt{1 - \left[k^{(1)}\right]^2}} \left[\beta^{(0)}(0) - k^{(1)}\alpha^{(0)}(1)\right]$$

and

$$\beta^{(1)}(1) = \frac{1}{\sqrt{1 - \left[k^{(1)}\right]^2}} \left[\beta^{(0)}(1) - k^{(1)}\alpha^{(0)}(2)\right]$$

where $\alpha^{(0)}(2) = R(2)$ and $\beta(0)(1) = R(1)$. Substituting the previous results into (A.25g) yields

$$k^{(2)} = \frac{\alpha^{(1)}(2)}{\beta^{(1)}(0)}$$

$$= \frac{R(2) - k^{(1)}R(1)}{R(0) - k^{(1)}R(1)}.$$

The Schur recursion equation can be realized as a p-th order normalized lattice structure as shown in Figure A.2.
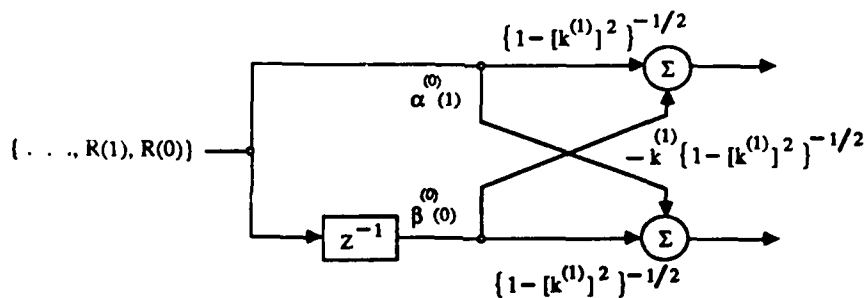
Figure A.2(a)   Zero Order ($n = 1$) Normalized Lattice Filter

130

$\{1-[k^{(1)}]^2\}^{-1/2}$

$\{1-[k^{(2)}]^2\}^{-1/2}$

$\{\ldots, R(1), R(0)\}$

$\alpha^{(0)}(1)$

$\alpha^{(1)}(2)$

$-k^{(1)}\{1-[k^{(1)}]^2\}^{-1/2}$

$-k^{(2)}\{1-[k^{(2)}]^2\}^{-1/2}$

z^{-1}

$\beta^{(0)}(0)$

z^{-1}

$\beta^{(1)}(0)$

Σ

$\{1-[k^{(1)}]^2\}^{-1/2}$

$\{1-[k^{(2)}]^2\}^{-1/2}$
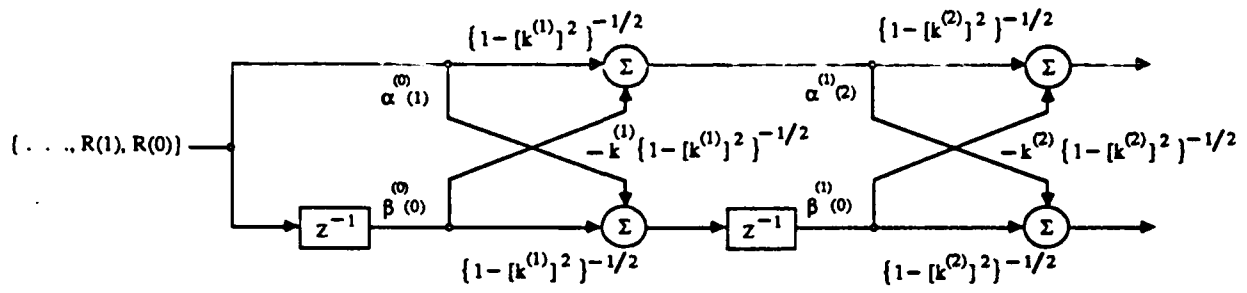
Figure A.2(b)   First Order ($n = 2$) Normalized Lattice Filter

APPENDIX B PSPICE EQUIVALENT CIRCUIT LISTINGS

IC INTERCONNECTION (PI-NETWORK AND MATCHED IMPED TERMINATION)
*

* MICROSTRIP TRANSMISSION LINE SIMULATION (LCL) PI - MODEL
* TEST STRUCTURE (LENGTH = 500E-06 m)
* SILICON SUBSTRATE (ER = 11.7)
*
.OPT ACCT LIST NODE OPTS NOPAGE RELTOL=.001
.WIDTH IN=133 OUT=80
.OPTIONS LIMPTS = 20000
.OPTIONS ITL5 = 50000
.OPTIONS TRTOL=5
.OPTIONS ITL4=5
V 1 0 PWL(0 0 3.75p .11 7.5p .25 11.25p 1.45 15p 1.9 18.75p 2 22.5p 1.9 26.25p 1.85 37.5p 1.6 52.5p 1.2
75p .72 78.75p 0)
RS 1 2 74.23
T1 2 0 3 0 Z0=74.23 TD=1.25ps
R1 2 0 1.065K
R2 2 3 10.4
R3 3 0 1.065K
C1 3 0 0.03pF
L1 3 4 0.332nH
C2 4 0 0.03pF
RL 4 0 74.23
.TRAN 1.25pS 80ps 0 1.25pS
.PROBE
.END
*

IC INTERCONNECTION (T-NETWORK AND MATCHED IMPED TERMINATION)
*
*
.OPT ACCT LIST NODE OPTS NOPAGE RELTOL=.001
.WIDTH IN=133 OUT=80
.OPTIONS LIMPTS = 20000
.OPTIONS ITL5 = 20000
.OPTIONS TRTOL=5
.OPTIONS ITL4=5
* PIECEWISE-LINEAR APPROXIMATION OF NORMALIZED PCE SAMPLER 1
V 1 0 PWL(0 0 3.75p .11 7.5p .25 11.25p 1.45 15p 1.9 18.75p 2 22.5p 1.9 26.25p 1.85 37.5p 1.6 52.5p 1.2
75p .72 78.75p 0)
RS 1 2 74.23
R1 2 0 1.065K
R2 2 3 10.4
R3 3 0 1.065K
T1 2 0 3 0 Z0=74.23 TD=2.23ps
C1 3 0 0.06pF
T2 3 0 4 0 Z0=74.23 TD=2.23ps
RL 4 0 74.23
.TRAN 1.25pS 100pS 0 0.05ps
.PROBE
.PRINT TRAN V(4)
.END

CASCADED-STEP DISCONTINUITY PSPICE PI-MODEL SIMULATION
*
* DIELECTRIC: (G-10 ER = 4.2)
* INPUT SIGNAL: (PIECEWISE-LINEAR APPROXIMATION OF THE MEASURED
* GAUSSIAN PULSE OF THE HP8510 NETWORK ANALYZER)
*
.OPT ACCT LIST NODE OPTS NOPAGE RELTOL=.001
.WIDTH IN=133 OUT=80
.OPTIONS LIMPTS = 20000
.OPTIONS ITL5 = 50000
.OPTIONS TRTOL=5
.OPTIONS ITL4=5
V 1 0 PWL(0 0 100P .06 300P .17 400P .37 800P 1.88 900P 2.02 1NS 1.93 1.4NS .41 1.5NS .17 1.6NS
.044 1.7NS 0)
RS 1 2 41.24
T1 2 0 3 0 Z0=41.24 TD=750PS
R1 3 0 3.118K
R2 3 4 1.091
R3 4 0 3.118K
T2 4 0 5 0 Z0=41.24 TD=214PS
C1 5 0 7.13PF
L4 5 6 0.362NH
C2 6 0 7.13PF
T3 6 0 7 0 Z0=41.24 TD=214PS
R4 7 0 3.118K
R5 7 8 1.091
R6 8 0 3.118K
RL 8 0 41.24
.TRAN 100PS 5NS 0 30PS
.PROBE
.PRINT TRAN V(2)
.PRINT TRAN V(8)
.END

CASCADED-STEP DISCONTINUITY PSPICE SHUNT CAPACITOR MODEL SIMULATION
*
* DIELECTRIC: (EPOXY G-10 ER = 4.2)
* INPUT SIGNAL: (PIECEWISE-LINEAR APPROXIMATION OF THE MEASURED
* GAUSSIAN HP8510 NETWORK ANALYZER SOURCE)
*
.OPT ACCT LIST NODE OPTS NOPAGE RELTOL=.001
.WIDTH IN=133 OUT=80
.OPTIONS LIMPTS = 20000
.OPTIONS ITL5 = 50000
.OPTIONS TRTOL=5
.OPTIONS ITL4=5
V 1 0 PWL(0 0 100P .06 300P .17 400P .37 800P 1.88 900P 2.02 1NS 1.93 1.4NS .41 1.5NS .17 1.6NS
.044 1.7NS 0)
RS 1 2 41.24
T1 2 0 3 0 Z0=41.24 TD=750PS
R1 3 0 2.316K
R2 3 4 1.409
R3 4 0 2.316K
T2 4 0 5 0 Z0=41.24 TD=214PS
C1 5 0 10.91PF
T4 5 0 6 0 Z0=7.424 TD=24.38PS
T5 6 0 7 0 Z0=7.424 TD=24.38PS
C2 7 0 10.91PF
T3 7 0 8 0 Z0=41.24 TD=214PS
R4 8 0 2.316K
R5 8 9 1.409
R6 9 0 2.316K
RL 9 0 41.24
.TRAN 100PS 5NS 0 30PS
.PROBE
.PRINT TRAN V(2)
.PRINT TRAN V(9)
.END

MULTI-SECTION MICROSTRIP FILTER LAYER-PROBING PSPICE SIMULATION
*

* DIELECTRIC:EPOXY (ER = 4.3), H=1.59mm, DESIGN FREQ = 8.79GHz
* CHARACTERISTIC IMPEDANCE = 59.2 Ohms (THEORETICAL)
*

.OPT ACCT LIST NODE OPTS NOPAGE RELTOL=.001
.WIDTH IN=133 OUT=80
.OPTIONS LIMPTS = 100000
.OPTIONS ITL5 = 100000
.OPTIONS TRTOL=5
.OPTIONS ITL4=5
*

* THE FOLLOWING PIECEWISE-LINEAR APPROXIMATION DESCRIBES AN INITIAL 100PS
* GAUSSIAN PULSE HAVING A 3DB BANDWIDTH OF 8.79 GHZ
*V3 1 0 PWL(0 0 10P .03 20P .33 30P .968 40P 1.68 50P 2 60P 1.68 70P .968 80P .33 90P .03 100P 0)
*

* THE FOLLOWING PIECEWISE-LINEAR APPROXIMATION DESCRIBES THE SIMULATED
* INVERSE FILTER OUTPUT USING THE 1ST DISCONTINUITY AR COEFFICIENT.
*V3 1 0 PWL(0 0 10P .03 20P .302 30P .668 40P .8 50P .47 60P -.1426 70P -.562 80P -.552 90P -.274
100P 0)
* THE FOLLOWING PIECEWISE-LINEAR APPROXIMATION DESCRIBES THE SIMULATED
* 2ND-ORDER INVERSE FILTER OUTPUT USING 1&2 DISCONTINUITY AR COEFFICIENTS.
*V3 1 0 PWL(0 0 10P .03 20P .276 30P .398 40P .206 50P -.238 60P -.558 70P -.436 80P -.053 90P .22
100P .212 110P .024 120P 0)
RS 1 2 59.22
T0 2 0 3 0 Z0=59.2 TD=1P
R1 3 0 831.7
R2 3 4 8.48
R3 4 0 831.7
T2 4 0 5 0 Z0=59.22 TD=292.6PS
C1 5 0 3.57PF
T4 5 0 6 0 Z0=59.22 TD=77.7PS
R4 6 0 1.55K
R5 6 7 4.52
R6 7 0 1.55K
T5 7 0 8 0 Z0=59.22 TD=77.7PS
C2 8 0 1.5PF
T6 8 0 9 0 Z0=59.22 TD=77.7PS
R7 9 0 1.55K
R8 9 10 4.24
R9 10 0 1.55K
T7 10 0 11 0 Z0=59.22 TD=77.7PS
C3 11 0 3.57PF
T8 11 0 12 0 Z0=59.22 TD=104.4PS
R13 12 0 2.323K
R14 12 13 3.02
R15 13 0 2.323K
RL 13 0 59.22
.TRAN 5PS 2.5NS 0 5PS
.PROBE
.PRINT TRAN V(2)
.PRINT TRAN V(13)
.END

LIST OF REFERENCES

[1] A.K Sinha, J.A. Cooper, and H.J. Levinstein, "Speed limitations due to interconnect time constants in VLSI integrated circuits," *Electron Devices Letters*, EDL-3, No. 4, pp. 90-92, April 1982.

[2] V.K. Tripathi and A. Hill, "Equivalent circuit modeling of losses and dispersion in single and coupled lines for microwave and millimeter-wave integrated circuits," *IEEE Trans. on Microwave Theory and Tech.*, MTT-36, No. 2, February 1988.

[3] N.S. Naham, "Picosecond-domain waveform measurements: Status and future directions," *IEEE Trans. on Inst. and Meas.*, 32, No. 1, March 1983.

[4] R.A. Pucel, *Monolithic Microwave Integrated Circuits*, IEEE Press, 1985.

[5] L.A. Zadeh, "From circuit theory to system theory," *Proc. IRE*, vol. 50, 1962.

[6] H.A. Atwater, "Tests of microstrip dispersion formulas," *IEEE Trans. on Microwave Theory and Tech*, MTT-36, No.3, March 1988.

[7] E. Yamashita, K. Atsuki and T Veda, "An approximate dispersion forumla of microstripline for computer-aided design of microwave integrated circuits," *IEEE Trans. on Microwave Theory and Tech.*, MTT-27, pp. 1036-1038, Dec. 1979.

[8] K.C. Gupta, R. Garg and T. Bahl, *Microstrip Lines and Slotlines*, Norwood, MA: Artech House, 1979.

[9] H.A. Hung, P. Polak-Dingels, K.J. Webb, T. Smith, H.C. Huang, and C.H. Lee, "Millimeter-wave monolithic integrated circuit characterization by a picosecond optoelectonic technique," *IEEE Trans. on Microwave Theory and Tech.*, MTT-37, No. 8 , pp. 1223-1231, August 1989.

[10] D. A. Auston, "Impulse response of photoconductor in transmission lines," *IEEE J. Quantum Electron.*, Vol. QE-19, pp. 639-648, April 1983.

[11] L.R. Rabiner and R.W. Schafer, *Digital Processing of Speech Signals*, Prentice-Hall, Englewood Cliffs, New Jersey, 1978.

[12] A. Bruckstein and T. Kailath, "An inverse scattering framework for several problems in signal processing," *IEEE ASSP Magazine*, Vol. 4, No.1, January 1987.

[13] A. Bruckstein, B. Levy, and T. Kailath, "Differential methods in inverse scattering," *SIAM J. Applied Math.*, Vol. 45, No. 2, April 1985.

[14] S. R. Parker, Notes for EC4900 (Lattice Parameter Modeling of Stochastic Signals: Some Fundamental Concepts), Naval Postgraduate School, 1986 (unpublished).

[15] D. W., Mennecke, "Adaptive ARMA lattice filter based on a generalized Mullis-Roberts Criterion," Master's thesis, Naval Postgraguate School, 1988.

[16] V.K. Tripathi and A. Hill, "Equivalent circuit modeling of losses and dispersion in single and coupled lines for microwave and millimeter-wave integrated circuits," *IEEE Trans. on Microwave Theory and Tech.*, MTT-36(2), February 1988.

[17] PSpice Electrical Circuit Simulator, Version 2.0, MicroSim Corporation, 1986.

[18] T.C. Edwards, *Foundations for Microstrip Circuit Design*, Wiley, 1981.

[19] R.Γ Owens, "Accurate analytical determination of quasi-static microstrip line parameters," *The Radio and Electronic Engineer*, Vol. 46, No. 7, pp. 360-364, July 1976.

[20] M.V. Schneider, "Microstrip lines for microwave integrated circuits," *Bell System Technical Journal*, 48(5), pp. 1421-1444, May-June 1969.

[21] I.J Bahl and R. Garg, "Simple and accurate formulas for microstrip with finite strip thickness," *Proceedings of the IEEE*, 65, pp. 1611-1612, 1977.

[22] J. B. Knorr and Ahmet Tufekcioglu, "Spectral-domain calculation of microstrip characteristic impedance," *IEEE Trans. on Microwave Theory and Tech.*, MTT-23(9), pp. 725-728, September 1975

[23] R. Mittra and T. Itoh, "A new technique for the analysis of dispersion characteristics of of microstrip lines," *IEEE Trans. on Microwave Theory and Tech.*, MTT-19(1), pp. 47-56, January 1971.

[24] W. J. Getsinger, "Microstrip dispersion model," *IEEE Trans. on Microwave Theory and Tech.*, MTT-21(1), pp. 34-39, January 1973.

[25] R.A. Pucel, D.J. Masse and C.P Hartwig, "Losses in microstrip," *IEEE Trans. on Microwave Theory and Tech.*, MTT-16, p. 342, 1968.

[26] E.O. Hammerstadt and F. Bekkadal, "A microstrip handbook," *ELAB Report*, STF 44 A74169, University of Trondheim, Norway, 1975, pp. 98-110.

[27] K.W. Goosen and R.B. Hammond, "Modeling of picosecond pulse propagation in microstrip interconnections of integrated circuits," *IEEE Trans. on Microwave Theory and Tech.*, MTT-37, pp. 469-478, March 1989.

[28] J.F. Whitaker, T.B. Norris, G. Mourow and T.Y. Hsiang, "Pulse dispersion and shaping in microstrip lines," *IEEE Trans. on Microwave Theory and Tech.*, MTT-35(1), pp. 41-47, January 1987.

[29] K.W. Goosen and R.B. Hammond, *Modeling of Picosecond Pulse Propagation on Silicon-Integrated Circuits*, pp. 70-73, Springer-Verlang, New York NY, March 1985.

[30] R.N. Ghose, *Microwave Circuit Theory and Analysis*, McGraw-Hill Book Co., Inc., 1960.

[31] E.A. Robinson and T.S. Durrani, *Geophysical Signal Processing*, Prentice Hall International, Englewood Cliffs, N.J., 1986.

[32] N.N. Rao, *Elements of Engineering Electromagnetics - 2nd Edition*, Prentice Hall International, Englewood Cliffs, N.J., 1987.

[33] S.M. Kay, *Modern Spectral Estimation: Theory and Application*, Prentice Hall, 1988.

[34] E.A. Oppenhiem and R.W. Schafer, *Digital Signal Processing*, Prentice Hall International, Englewood Cliffs, N.J., 1975.

[35] S. Ramo, J.R. Whinnery and T. Van Duzer, *Fields and Waves In Communications Electronics - 2nd Edition*, J. Wiley and Sons, New York, N.Y., 1984.

[36] M. T. Jong, *Methods of Discrete Signal and System Analysis*, McGraw-Hill Book Co., New York, 1982.

[37] V.F. Fusco, *Microwave Circuits Analysis and Computer-Aided Design*, Prentice Hall, Englewood Cliffs, N.J., 1987.

[38] J.R. Whinnery and H.W. Jamieson, "Equivalent circuits for discontinuities in transmission lines," *Proceedings of the I.R.E.*, pp. 98-107, February 1944.

[39] A.A. Oliner, "Equivalent circuits for discontinuities in balanced strip transmission line," *IEEE Trans. Microwave Theory Tech.*, Vol. MTT-3, pp. 134-143, November 1955.

[40] W. Menzel and I. Wolff, "A Method for calculating the frequency-dependent properties of microstrip discontinuities," *IEEE Trans. Microwave Theory Tech.*, Vol. MTT-25, pp. 107-112, February 1977.

[41] C. Gupta and A. Gopinath, "Equivalent circuit capacitance of microstrip step change in width," *IEEE Trans. Microwave Theory Tech.*, v. MTT-25, pp. 819-822, February 1977.

[42] R.D. Strum and D. E. Kirk, *First Principles of Discrete Systems and Digital Signal Processing*, Addison-Wesley, Inc, New York, 1988.

[43] A.G. Evans and R. Fischel, "Optimal Least Squares Time-Domain Synthesis of Recursive Digital Filters," *IEEE Trans. on Audio and Electroacoustics*, vol. AU-21, no.1, pp. 61-65, February 1973.

[44] C.S. Burrus and T.W. Parks, "Time Domain Design of Recursive Digital Filters," *IEEE Trans. on Audio and Electroacoustics*, Vol. AU-18, No.2, pp. 137-141, June 1970.

[45] W.C. Elmore, "The Transient Response of Damped Linear Networks with Particular Regard to Wideband Amplifiers," *J. Appl. Phys.*, Vol. 19, pp 55-83, 1948.

[46] S.J. Orfanidis, *Optimum Signal Processing - An Introduction*, Macmillan Publishing Co., New York, 1985.

[47] Y. Miyanaga, N. Nagai, and N. Miki, "ARMA digital lattice filter based on new criterion," *IEEE Trans. Circuits Syst.*, vol. CAS-34, No.6, June 1987.

[48] J. Durbin, "Fitting of time-series models," *Revue Inst. Int. Statist.*, Vol 28, pp. 233-243, 1960.

[49] D.H. Auston, "Picosecond optoelectronic switching and gating in silicon," *Applied Physics Letters*, 26(3), pp. 101-103, 1975.

[50] A.M. Johnson and D.H. Auston, "Microwave switching by picosecond photoconductivity," *IEEE Journal of Quantum Electronics*, QE-11(6), pp. 283-287, 1975

[51] W.R Eisenstadt, R.B. Hammond, and R.W. Dutton, "Integrated silicon photoconductors for picosecond pulsing and gating," *Electron Device Letters*, EDL-5(8), pp. 296-298, 1984.

[52] W.R Eisenstadt, "High frequency measurements of integrated circuit devices and interconnects," PhD thesis, Stanford University, p. 96, 1985.

[53] D.R. Bowman, "High speed polycrystalline silicon photoconductors for on-chip pulsing and gating," PhD thesis, Stanford University, 1985.

[54] E.M. Siomacco and S. R. Parker, "Modeling of dispersive multi-layered media using layer-peeling and layer-probing", *Proc. of 21st Asilomar Conf. on Circuits, Systems and Computers*, Pacific Grove, California, pp. 31-34, Maple Press, Inc., 1987.

[55] R. Compton and D. Rutledge, *PUFF - Computer Aided Design for Microwave Integrated Circuits*, Department of Electrical Engineering, California Institute of Technology, Pasadena, CA 91125, 1987.

[56] D.J. Klich, "Efficient multichannel autoregressive modeling in time and frequency domain," Ph.D. thesis, Naval Postgraduate School, 1982.

[57] F. Itakura and S. Saito, "On the optimum quantization of feature parameters in Parcor speech synthesizer," *Proc. of 1972 Conf. on Speech Com. Processing*, 1972.

INITIAL DISTRIBUTION LIST

No. Copies

1. Library, Code 0142   2
   Naval Postgraduate School
   Monterey, California, 93943

2. Defense Technical Information Center   2
   Cameron Station
   Alexandria, Virginia 22304-6145

3. Chairman, Code EC   1
   Department of Electrical and
   Computer Engineering
   Naval Postgraduate School
   Monterey, California, 93943-5000

4. Dr. Murali Tummala, Code EC/Tu   5
   Department of Electrical and
   Computer Engineering
   Naval Postgraduate School
   Monterey, California, 93943

5. Dr. Glen A. Myers, Code EC/Mv   1
   Department of Electrical and
   Computer Engineering
   Naval Postgraduate School
   Monterey, California, 93943

6. Dr. Charles W. Therrien, Code EC/Ti   1
   Department of Electrical and
   Computer Engineering
   Naval Postgraduate School
   Monterey, California, 93943

7. Dr. Jeffery B. Knorr, Code EC/Ko   2
   Department of Electrical and
   Computer Engineering
   Naval Postgraduate School
   Monterey, California, 93943

8. Dr. Harold Fredricksen, Code MA/Fs   1
   Chairman, Department of Mathematics
   Naval Postgraduate School
   Monterey, California, 93943

9. Dr. Michael J. Zyda, Code CS/Zk   1
   Department of Computer Science
   Naval Postgraduate School
   Monterey, California, 93943

10. Major Edward M. Siomacco   4
    4913 Ashton Road
    Fayetteville, North Carolina, 28304

11. Dr. R. Madan, Code 1114   1
    Office of Naval Research
    800 N. Quincy Street
    Arlington, Virginia 22217-5000

12. Dave Rubin, Code 753,   1
    Microwave and Millimeter-wave Branch
    Naval Ocean Systems Center
    San Diego, California 92152

13. Joe Mosko, Code 35203,   1
    RF Development Section
    Naval Weapons Center
    China Lake, California 93555

14. Chairman   1
    Department of Electrical Engineering and
    Computer Science
    United State Military Academy
    West Point, New York 10996-5000

15. Science Research Laboratory   1
    United State Military Academy
    West Point, New York 10996-5000

16. Dr. Sydney R. Parker   1
    P.O. Box AQ
    Carmel, California 93921